Rendering dark energy void

by

Sean February

A thesis submitted in partial fulfillment for the

degree of Master of Science in Cosmology

in the

Faculty of Science

Department of Mathematics and Applied Mathematics

University of Cape Town

July 2009

Thesis directed by

Supervisor: Dr. Christopher Clarkson
University of Cape Town
South Africa

and approved by

Internal Examiner:

External Examiner:

Declaration of Authorship

I declare that this thesis is my own work, and hereby certify that unless stated, all work contained within this thesis is my own to the best of my knowledge.

This thesis is being submitted for the degree of Masters of Science in Cosmology in the department of Mathematics at the University of Cape Town.

Sean February
July 2009

Abstract

The current model of cosmology, the Friedman-Lemaître-Robertson-Walker model, assumes that the universe is approximately homogeneous and isotropic on very large scales. Further assuming flatness and dark energy in the form of Einstein's cosmological constant Λ then implies that the latter contributes roughly 73% of the total energy of the universe, cold dark matter (CDM) 23%, and baryons, the matter we are made, only 4%. Although this so-called ΛCDM model can explain the bulk of present cosmological observations with great accuracy, we have no theoretical understanding of what Λ actually is, and where it comes from. Recently, however, it was shown that another particular exact solution to Einstein's field equations, the Lemaître-Tolman-Bondi (LTB) solution, can be used as an alternative to dark energy if we are placed at the centre of a large (few gigaparsecs in size) nonlinearly underdense region of the universe, or void. Various void parameterizations, including one capable of reproducing the ΛCDM distance modulus to arbitrary accuracy, are tested here against the recent Constitution sample of 397 type Ia supernova (SN) as well as the Hubble rate data. We find better fits to these datasets than that of the ΛCDM model, and, in contrast to that seen in literature, show that current SN data alone cannot distinguish between void models and that of ΛCDM. While the Hubble rate data will help in the future to distinguish these two models, perturbation theory may also be developed to allow for further constraints from Baryon Acoustic Oscillations and the Cosmic Microwave Background. In fact, in a recent paper, we have explored linear perturbation theory about LTB models, and include this work as an appendix.

Acknowledgements

I owe a number of people in the Cosmology and Gravity Group, situated in the Department of Mathematics and Applied Mathematics at the University of Cape Town, my sincere gratitude and thanks for their priceless contribution towards this thesis, which began roughly a year ago.

I would firstly like to express my deep appreciation to Dr. Christopher Clarkson for his supervision, advice, guidance, encouragement and above all, for the incredible excitement, energy and interest he displayed in my work throughout. My gratitde also extends to Dr. Timothy Clifton from the University of Oxford for useful discussions and for his generous contribution towards the paper he, myself and Dr. Chris Clarkson published in the Journal of Cosmology and Astroparticle Physics in June 2009.

A large part of this thesis involved data analysis and reduction, something I had very basic knowledge of, until I met Dr.'s Julien Larena and Matthew Smith. I would therefore like to acknowledge the huge part they played during my research, which came about through the many insightful discussions and meetings I had with them. Thank you both so much.

I would also like to thank my family too for their continued support, encouragement, and hospitality, without which none of this work would be possible.

Finally, I want to thank the National Astrophysics and Space Science Program (NASSP), the National Research Foundation (NRF) as well as the Department of Science and Technology (DST) for financial assistance for my studies and travels.

Contents

List of Abbreviations

AIC	**A**kaike **I**nformation **C**riterion
BAO	**B**aryon **A**coustic **O**scillation
BBN	**B**ig **B**ang **N**ucleosynthesis
BIC	**B**ayesian **I**nformation **C**riterion
CDM	**C**old **D**ark **M**atter
CMB	**C**osmic **M**icrowave **B**ackground
CP	**C**opernican **P**rinciple
DE	**D**ark **E**nergy
EFE	**E**instein **F**ield **E**quation
EOS	**e**quation **o**f **s**tate
FE	**F**riedmann **E**quation
FLRW	**F**riedmann-**L**emaître-**R**obertson-**W**alker
FWHM	**F**ull **W**idth at **H**alf **M**aximum
LRG	**L**uminous **R**ed **G**alaxy
LTB	**L**emaître-**T**olman-**B**ondi
SDSS	**S**loan **D**igital **S**ky **S**urvey
SNIa	**S**upernova type **Ia**
WMAP	**W**ilkinson **M**icrowave **A**nisotropy **P**robe

Cosmological Parameters/Observables

Λ	cosmological constant
ρ_M, ρ_Λ	physical matter and cosmological constant energy densities
Ω_M, Ω_K, Ω_Λ	dimensionless matter, curvature and cosmological constant densities
w	equation of state parameter
μ	distance modulus
H_0, H	Hubble constant and Hubble parameter
q	deceleration parameter

List of Figures

List of Tables

Chapter 1

Introduction and Review

The idea that we are living in a universe whose expansion is accelerating is baffling to anyone familiar with the concept of basic Newtonian gravity: if the contents of the universe is supposedly dominated by matter (or similarly any pressureless fluid) at present, then why is the expansion rate currently speeding up, instead of slowing down? Well, the current generally accepted answer to that question is that our universe is not dominated by known matter at present, but by some unknown fluid with a negative pressure – coined *dark energy* – which behaves as 'anti-gravity' would, pushing the fabric of space on which (clusters of) galaxies live faster apart than gravity can pull them together, and may just be the culprit in this whole dilemma.

This idea has led to the development of the ΛCDM cosmological concordance model, built on the Friedman-Lemaître-Robertson-Walker (FLRW) metric which combines two assumptions: that the universe around us is without a preferred direction (isotropic), and the Copernican Principle (CP), which states that our position in the universe is not specially favoured [1], holds. The universe is then forced to be homogeneous (all points in space look the same) and we end up with the Cosmological Principle – a universe which is isotropic around every point. A simple model indeed, yet it can explain the bulk of what we observe today with great accuracy. However, it comes at a price: the visible baryonic matter we seem to know and understand from measurements in the laboratory makes up approximately only 4% of the total energy of the universe, leaving us to explain exactly what makes up the rest. In fact, we now know that this remaining 96% actually contains two 'dark' contributions: approximately one quarter in the form of cold dark matter (CDM), and the rest as dark energy in the form of Einstein's cosmological constant Λ.

Although there has been much progress in understanding the nature of CDM, we still have no clue what Λ is, and where it comes from. Indeed, we know, at least mathematically, that the cosmological constant is equivalent to the vacuum energy. However, calculations of the magnitude of the latter exceed that of Λ by some 120 orders of magnitude – this is known as the cosmological constant problem [2]. Another problem concerning Λ is the conincidence problem: if the energy density of the cosmological constant remains the same throughout the history of the universe (i.e. $\rho_\Lambda(t) = \rho_{\Lambda_0}$), and the energy density due to matter $\rho_{_M}$ was larger than ρ_Λ in the past and decreases (as $\rho_{_M}(t) \propto t^{-2}$) over time, then why are the magnitudes of these quantities so comparible today, exactly at the time we are measuring them? These issues may be due to (some of) the assumptions (i.e. homogeneity and isotropy) of the standard model not being valid, or it may just be the case that our univese is is stranger than we thought, or both. Either way, it is worth exploring all the possibilities, in the hope that we can pin down the true nature of our universe.

Perhaps, the first logical step is to find which models can explain the current cosmological data without invoking Λ, and perhaps dark energy in general. Recently there have been many investigations into possible alternatives to dark energy, from modified gravity, brane-world models and backreaction (see [3, 4, 5, 6] and references therein), to even using some of the already existing exact solutions to Einstein's field equations, namely the isotropic but inhomogeneous Lemaître-Tolman-Bondi (LTB) spacetime and the anisotropic, inhomogeneous Szekeres solution, respectively. In particular, the idea that we shall focus on in this thesis is that which assumes we (the observer) occupy the centre of a large ($\sim$ few Gpc in size) underdense region of our Universe, or *void*. The latter is usually modelled using the inhomogeneous LTB metric which exhibits spherical symmetry about the centre [7, 8, 9], and contains only a pressureless matter fluid (or dust). Moreover, in such a model, our Local Group would have to be within roughly tens of megaparsecs (Mpc) of the centre of the void [10] in order to be consistent with the observed isotropy of the Cosmic Microwave Background (CMB) [11]. In any case, this model violates the CP – the principle upon which our current concordance model is based. But of course, the CP has, to this day, not yet been proven. In fact, observations of the spatial distribution of local galaxy clusters reveals large overdensities (e.g. the Shapley Supercluster [13], see also [14] and references therein), walls (e.g. the Sloan Great Wall, with length $\sim$ 400 Mpc, see [15] and references therein]), filaments and voids, implying that, at least on small scales ($\sim$ hundreds of Mpc), the universe is not

homogeneous. Although the assumption for homogeneity is meant to hold on larger scales, what exactly the size of that scale is, is not clear. Is violating the unproven CP then such a terrible thing if we were able to explain all of the observations without dark energy?

At the moment, of course, void models have not yet been properly scrutinized with all of the available cosmological data (see section 1.3 for a review). For instance, they are yet to be shown to agree with the full CMB angular power spectrum since this requires linear perturbation theory to be carried out in these models – which has, in fact, been attempted by Zibin [16] and, more recently, explored by the author [17] as shown in Appendix C.

In particular, we shall make use of the largest SN sample to date, the Constitution dataset [18], as well as the Hubble rate data [23] to constrain our void model parameters, and leave the testing of our models against such observations of structure formation for future work.

In the next section we highlight some of the key events in history that led to the current concordance model of cosmology. We will then briefly discuss some of the important observational data used in cosmology today, starting off with the particular observations we have used in our study, and ending with observations that can, at present, only be completely analyzed in FLRW models. Thereafter we provide a brief review of LTB void models, and quickly touch on other alternatives to dark energy. In the first section of Chapter 2 we introduce the basic theory governing homogeneous and isotropic cosmologies, and in the second section we tackle the theory involved in the inhomogeneous and isotropic LTB models. In Chapter 3 we introduce and discuss the void models we consider, and Chapter 4 concerns the testing of these models against present cosmological data. We then finally conclude in Chapter 5.

1.1 The Standard Model

Soon after Albert Einstein proposed his general theory of relativity (GR) in 1916, he introduced a 'cosmological constant' Λ into his field equations – which assumed a simple homogeneous and isotropic Friedman-Lemaître-Robertson-Walker (FLRW) spacetime – in order to exactly balance the attrative gravity of matter as he believed that the universe was static [24]. However, when Edwin Hubble discovered in 1929 [25] that the universe was actually expanding, standard big bang cosmology was

born: the basic conjecture being that the universe (and spacetime itself) began from an extremely hot, dense and microscopically small point some time in the past, created all the light elements in the process of (Big Bang) Nucleosynthesis (BBN), cooled throughout as it expanded, and any irregularities in the matter distribution that existed condensed via gravitational collapse into the galaxies we see today. Although the motivation for Λ was consequently lost, it was nevertheless resurrected (see e.g. [26, 27]) and subsequently discarded many times after that.

The discovery in 1965 by Penzias and Wilson [28] of the nearly uniform (to about 1 part in 10^5) microwave background radiation temperature ($T \approx 3K$) left by the CMB (i.e. the 'surface of last scattering' where photons decoupled from matter some three hundred thousand years after the big bang) served as an important piece of evidence for the 'hot' big bang hypothesis: if the universe indeed started off from such an extremely high temperature, then all of the matter present could only exist in an ionized state (i.e. electrons and protons, in addition to photons). As the universe expanded and cooled, Thomson scattering would continue to take place between the baryons and photons, until temperatures were cool enough (at $T \approx 3000K$) for electrons to combine with protons to form atoms, at which point (roughly) the photons any baryons decouple from each other, allowing the photons to free-stream throughout the cosmos [29]. We then measure that residual background radiation today (after the universe has cooled significantly) as the CMB surface if it were a perfect blackbody (see [30] for a review on the CMB). Penzias and Wilson's discovery also backed-up the validity of the assumption that the universe is (almost) isotropic on large scales, which when combined with the CP, immediately implies that the universe should be (almost) homogeneous too on large scales – this is a consequence of the EGS theorem [31] (or, more appropriately, the almost EGS theorem [32]), which states that if every observer in an expanding dust-filled universe views an (almost) isotropic radiation field around them, then that universe is (almost) FLRW.

However, the standard big bang model was not without problems: for instance, how can two patches on the sky (being causally disconnected in the past) have such similiar temperatures (i.e. the horizon problem)? And why is the universe so geometrically flat (as deduced from the CMB) on large scales (i.e. the flatness problem)? Well, in the early 1980's Guth's [33] inflationary scenario provided a resolution to these and other problems. Inflation, now generally accepted, refers to the process taking place in the very early universe causing it to expand by several

billions of factors in size, in only a fraction of a second. This rapid early expansion allows all parts of the sky we see today to be in thermal equalibrium at some earlier time (thus solves the horizon problem) and predicts a value for the total density the universe to be that of the critical density (thus solving the flatness problem). In addition, and perhaps more remarkable, are the quantum fluctuations that inflation predicts – these set the initial conditions of the distribution of matter in the very early universe, thus providing the 'seeds' for structure formation to take place later on [33].

Indeed, around the same time inflation was introduced to rescue the standard model of cosmology, another discovery came along which puzzled the scientific community. Although discovered already in 1933 by Swiss astronomer Fritz Zwicky [34], who noticed, via the virial theorem, that the Coma cluster had to contain several hundred times more mass than was visibly present in order to account for the larger-than-expected perculiar velocities [35], his claim of 'dark matter' being the likely explanation was only taken more seriously after Vera Rubin's galaxy rotation curve measurements [36]: she found that as one went away from the galactic center, orbital velocities of stars did not decrease as expected from Keplerian motion, but remained constant and even increased a little in some cases. The only way this can happen is if the mass of the galaxy increases linearly with distance, which is precisely consistent with the idea of dark matter (DM) being present. More recently, the claim that DM exists has been strengthened through its indirect detection via weak lensing (see e.g. [37, 38] and the references therein for a proper review on DM and observational evidence for it). From a theoretical view-point, however, a lot has been done to try and pin down the very nature of DM. In particular, models of structure formation require the DM to be of the 'cold' non-relativistic type, namely cold dark matter (CDM). Moreover, CDM plays such a crucial role in the process of structure formation [39, 37, 40], mainly in the radiation dominated era, as it allows gravitational instability to occur soon after decoupling, that if it did not exist at all, the universe today would have looked very much different – in particular, the largest structure in such a universe would be far smaller than what we observe today – not to mention, the chances of life developing in such a universe would probably be much lower. In particle physics, on the other hand, CDM is usually treated as some type of neutral but massive weakly interacting particle (WIMP), and there are now several candidates which appear in the literature: neutrinos, axions, Kaluza-Klein gravitons, gravitinos, neutralinos, sneutrinos, primordial black holes, particles from

little Higgs models etc. [37]. The search for these particles certainly continues, both in the laboratory [41] as well as through astrophysical observations (see [38, 39] for a review).

It was not until the late 90's with the discovery of accelerated expansion via type Ia supernovae (SN) [42, 43] that Λ was finally back in business, and the universe we seemed to understand took a surprising turn – their results showed that the rate at which the universe is expanding is actually increasing! Since then, Λ has remained in the lime-light, with follow-up observations taking place all the time [44, 45, 19], albeit with no theoretical understanding of its origin or magnitude. All we know is that, when modelled as a perfect (barotropic) fluid with linear equation of state $p = w\rho$, its pressure equals minus its density (i.e. where the equation of state parameter $w = -1$), such that its energy density remains constant over time – thus mimicking the nature of the vacuum energy. Of course, other more exotic dark energy models (i.e. $w < -1/3$) exist which considers w to be redshift dependent in some way, which can usually be modelled by some scalar field ϕ. However, these models fail to provide any physical insight into what this gravitationally repulsive force actually is, and, in addition, there is rarely any physical motivation involved (from a particle physics view-point) for such models, and nearly always do fine-tuning issues arise (See e.g. [5, 46, 4] for a review, as well as references therein). Nevertheless, the ΛCDM model has been able to agree with the numerous cosmological observations we have to date with remarkable accuracy, as we shall briefly review in the next section.

1.2 Cosmological Observations

In this section, we outline the cosmological data we shall be using to constrain our void model parameters, and briefly touch on additional observations the ΛCDM model has been tested against which are yet to be properly done in the context of LTB models since they require the use of linear perturbation theory (as shall be later discussed).

1.2.1 Type Ia Supernova

A type Ia supernova (SNIa) is a highly luminous astronomical event arising from the thermonuclear explosion of a carbon-oxygen white dwarf due to its mass exceeding that of the Chadrasekhar mass ($\sim$ 1.4 solar masses) after accreting sufficient

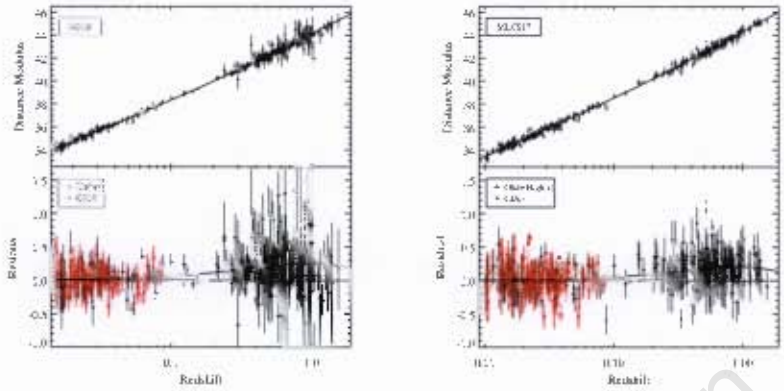

Figure 1.1: Left panel: Distance moduli (Hubble diagram) (top) and normalized (to a universe with $\Omega_M = 0.27$ and $\Omega_\Lambda = 0$) distance moduli (residuals) (bottom) for the Constitution sample as determined by the SALT light-curve fitter. The new low redshift sample CfA3 SN (red) [18] and the Union sample [15] (black) are shown in the bottom panel, along with the best-fit cosmology. Right panel: Hubble diagram (top) and residuals (bottom) as determined by the MLCS17 light-curve fitter. The black points in the bottom panel are the high redshift SN compiled from [20, 21, 22]. Notice the smaller dispersion at higher redshift for MLCS17 than for SALT. Taken from [19].

material from its companion star. However, SNIa are classified spectroscopically (which is also used to derive their redshift) according to the absence of hydrogen absorption lines, as opposed to type II supernovae which are abundant in hydrogen, and also to the presence of strong silicon lines in their early and maximum spectra. Moreover, because their peak brightness has such a small dispersion over their entire population — due to the relationship between their light curve shape and luminosity i.e. broader means brighter, narrower means fainter — the standard error in intrinsic (or absolute) SN luminosity is reduced by a factor of three, making them into standardizable candles. SNIa are thus used extensively in cosmology as distance indicators because, if we know how bright they are, we can determine how far they are away via the standard formula for the distance modulus,

$$\mu = m - M = 5 \log_{10} \left[\frac{d_L}{\text{Mpc}} \right] + 25 , \tag{1.1}$$

where m and M are their apparent and absolute magnitudes, respectively, and d_L their luminosity distance (defined in the next chapter), and moreover, can use

them to constrain cosmological paramters. In fact, just over a decade ago, two independent groups studying distant SN, the 'Supernova Cosmology Project' [48, 42] and the 'High-Z Supernova Search Team' [47, 43], discovered that distant SN were fainter than that expected in a matter dominated universe, from which it was immediately inferred that the expansion rate of our universe is actually speeding up. This apparent dimming of distant SN certainly caused a stir in the cosmology community when astrophysical explanations such as the presence of extragalactic gray dust [49, 50, 51, 52] and pure luminosity evolution [53] were ruled out, because this meant, in the context of a homogeneous and isotropic universe, that some unknown fluid with a negative pressure was not only necessary, but was required to make up approximately 73% of the energy budget of the universe.

In our study, we make use of the largest sample of SN to date, the Constitution set consisting of 397 SNIa [19]. The Consititution set combines the Union data set [45] with the rececntly acquired low redshift CfA3 sample [18] (see left panel Fig. 1.1). We specifically used the MLCS light-curve fitter applied to the sample, as it makes the extraction of best-fit parameters easier (resulting magnitudes are cosmology independent, so is absent of the additional 'nuisance' parameters present in SALT [19]) and contains significantly less scatter (see right panel Fig. 1.1). In addition, we modify the errors by adding in the uncertainty due to the intrinsic dispersion of SN luminosity, and, as a consequence, decrease the value of a given model's (reduced) χ^2-statistic – a measure of how well a model fits the data, the lower the χ^2 the better the fit (see section 4.2.1).

1.2.2 Ages

Using the ages and redshifts of passively-evolving luminous red galaxies (LRG's), [23] (based on [54] and references therein) showed that the quantity dz/dt can be constructed by measuring the age difference Δt of two ensembles of such galaxies that formed at the same time but separated by a small redshift interval Δz. The quantity dz/dt, as shall be shown in the next chapter, is directly related to the Hubble parameter H via

$$H(z) = -\frac{1}{1+z}\frac{dz}{dt}. \tag{1.2}$$

The absolute age of each passively-evolving LRG is estimated from synthetic stellar population models applied to the oldest stars in that galaxy. Galaxies within $\Delta z = 0.03$ of each other are grouped together, and the average age of the latter is then

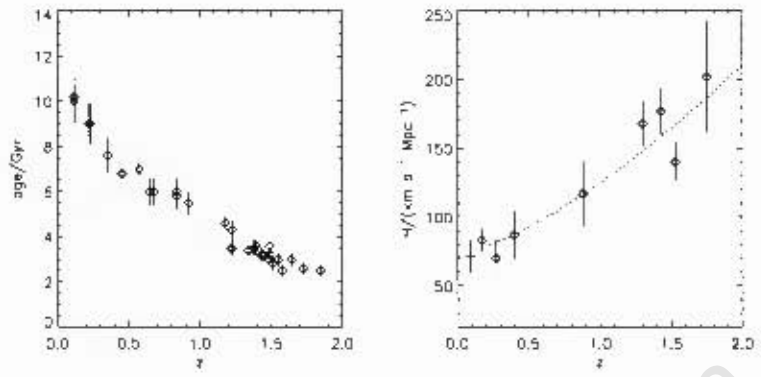

Figure 1.2: Left panel: Absolute ages for the 32 LRG's determined by [23] plotted as a function of redshift. Right panel: The resulting Hubble parameter estimates as a function of redshift, along with the best-fit ΛCDM model (dotted line)

determined to improve the estimate of the age of the universe as a function of redshift (see the left panel of Fig. 1.2). Age and redshift differences between pairs of the latter within $0.1 < \Delta z < 0.15$ of each other is then computed and provides us with the ratio $\Delta z/\Delta t$ (see the right panel of Fig. 1.2). From the 32 LRG sample, only 9 data points for the quantity dz/dt finaly arise, and the redshift of each point, needed for calculating $H(z)$ as shown in Eq. (1.2), is found by taking the average redshift of the pair of points (where each point referred to here is given by the galaxies that are grouped) that are subtracted to finally give dz/dt.

In our analysis we include the HST key project [56] data point for the value of H at the origin i.e. $H_0 = H(z = 0) = 72 \pm 8$ km/s/Mpc, giving us a total of 10 points to work with in the interval $0.0 \leq z \leq 1.75$. Finally note that, at the time of writing, follow-ups of the work done in [23] was carried out [125, 126], in which a few more points for $H(z)$ was added.

1.2.3 Other Observations

We briefly touch on two additional key observations used extensively in FLRW models today that require the use of perturbation theory, namely the Cosmic Microwave Background and the Baryon Acoustic Oscillations. Only when the observable quantities related to these observations are properly calculated in the LTB model should they be taken into account when confronting those models with observations.

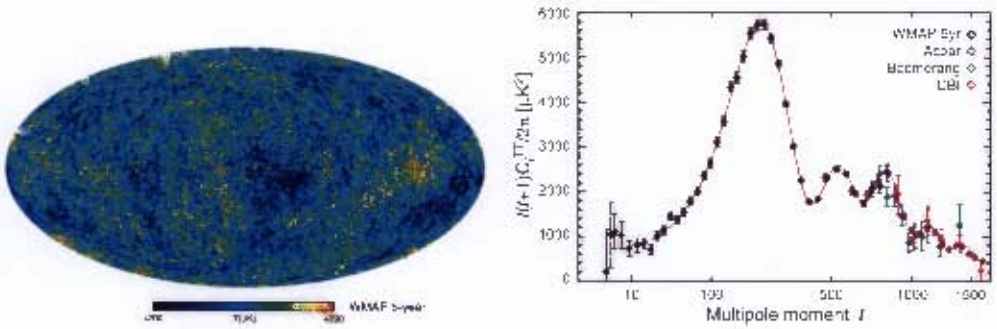

Figure 1.3: Left panel: The foreground-reduced Internal Linear Combination map based on the 5 year WMAP data [11]. Right panel: The WMAP 5-year TT power spectrum along with recent results from the ACBAR ([57], purple), Boomerang ([58], green), and CBI ([59], red) experiments. The red curve is the best-fit ΛCDM model to the WMAP5 data. Taken from [12].

Cosmic Microwave Background: Observations of the radiation that left the surface of last scattering, such as that from the Wilkinson Microwave Anisotropy Probe (WMAP), has provided us with valuable information pertaining to the physical processes that took place in the universe, as well as to some key cosmological parameters, during the first 380 000 years after the Big Bang. WMAP's observations covers five different frequencies: 22, 33, 41, 61 and 94 GHz. Adding linear combinations of all-sky temperature maps of these (for details, see [11]), and removing foreground contamination from galaxies etc., we obtain the so-called Internal Linear Combination map of the CMB sky (left panel of Fig. 1.3). The latter provides us with the amplitude of temperature fluctuations $\frac{\Delta T}{T}$ on the sky, which has been measured to be $\sim 10^{-5}$. The standard way of comparing models of large scale structure with observations is via power spectra, which are the harmonic transforms of the two-point correlation functions. For the CMB anisotropy power spectrum, we decompose $\frac{\Delta T}{T}$ into spherical harmonics as

$$\frac{\Delta T}{T}(\theta,\phi) - \sum_{l=1}^{\infty}\sum_{l=-m}^{l=m} a_{lm}Y_{lm}(\theta,\phi)\,, \tag{1.3}$$

where θ and ϕ correspond to the angular co-ordinates of a point on the two-sphere,

$$a_{lm} = \int_{\pi}\int_{0}^{\pi}\frac{\Delta T}{T}(\theta,\phi)Y^{*}(\theta,\phi)\sin\theta d\theta d\phi\,, \tag{1.4}$$

are the expansion coefficients, and Y_{lm} are the standard spherical harmonics. The

angular power spectrum of the CMB is defined as

$$C_l = \left\langle |a_{lm}|^2 \right\rangle , \tag{1.5}$$

and in the right panel of Fig. 1.3 we show a plot of the latter from the latest WMAP 5-year data (WMAP5), as well as that from ACBAR [57], Boomerang [58] and CBI [59]. The red curve shows the best-fit to WMAP5 ΛCDM model, thus supporting the need for an exotic energy component in the universe.

Baryon Acoustic Oscillations: During the radiation domination era early in the universe, baryons and photons were tightly coupled via Thomson scattering in a relativistic plasma, and the dark matter was clumping and setting up deep gravitational potential wells [60, 62, 61, 63, 64]. Primordial perturbations from inflation that entered the Hubble horizon[1] initialized acoustic (sound) waves in this plasma (showing up as the CMB acoustic peaks just discussed). As the universe expanded, overdensities in the initial baryon-photon density distribution were driven outwards in high pressure, nearly spherical 'bubbles', dragging the original distribution (i.e. the overdense peak) of dark matter (which is gravitationally attracted to the baryons) along very slowly. Once the universe was cool enough for neutral hydrogen to from, the photons were able to decouple from the baryons and free-stream away. This allowed one final outward motion of the spherical shells of baryonic matter by the residual momentum left over from the acoustic wave prior to decoupling, until coming to complete stop at an epoch known as the baryon-drag epoch. Although most of the dark matter remains present at the initial origin of the acoustic wave (i.e. at the center of the expanding bubble), a portion of it is attracted to the dense shell of baryons surrounding it. As such, a 'bump' in the two-point correlation function of galaxies is expected (see [65, 67] and references therein), not only at the origin, but at a scale corresponding to the radius of these spherical shells, which is related to the comoving sound horizon at the baryon-drag epoch. This scale has consequently been dubbed the Baryon Acoustic Oscillation (BAO) scale, the size of which depends mostly on the physical matter ($\Omega_M h^2$) and baryon ($\Omega_b h^2$) densities[2], as well as the time to recombination and the time of matter domination, and therefore provides a 'standard ruler' with which to measure the expansion history [69, 68].

[1] This is the length scale in cosmology within which physical processes can connect causally.

[2] The quantity $\boldsymbol{h}$ is related to the Hubble constant via $\boldsymbol{H}_0 = 100\boldsymbol{h}$ km/s/Mpc.

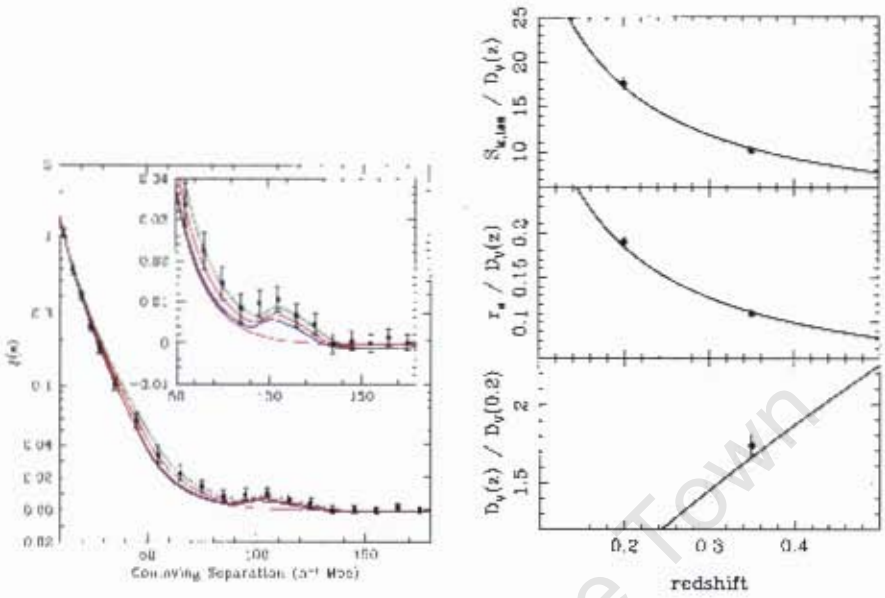

Figure 1.4: Left panel: The detection of the BAO peak in the two-point correlation function of LRG's in the SDSS [65]. The curves correspond to ACDM predictions for $\Omega_\nu h^2 = 0.12$ (green), 0.13 (red) and 0.14 (blue), and the magenta curve shows a ACDM model without baryons. Right panel: Three different methods of using BAO to constrain cosmological models [67]. Constraints from BAO observations are shown (solid circles with 1σ error), along with the best-fit ACDM model.

Recently, in fact, using a sample of LRG's from the Sloan Digital Sky Survey (SDSS), [65] detected such a feature – a 'bump' in the two-point correlation function at a scale $\sim 100h^{-1}$ Mpc (see left panel Fig. 1.4). In Fourier space, this bump corresponds to (damped, nearly harmonic) oscillations[3], hence the term 'oscillations' in the name BAO.

Assuming that the survey covers a small redshift and angular interval, Δz and $\Delta\theta$, respectively, and that the comoving line-of-sight (radial) galaxy seperation $r_\parallel$, which scales as [70]

$$r_\parallel(z) = \frac{c\Delta z}{H(z)}, \tag{1.6}$$

[3]The Fourier transform of the two-point correlation function is the power spectrum.

is equivalent to that of the angular scale[4],

$$r_{\_}(z) = (1+z)d_{\rm A}(z)\Delta\theta\,, \tag{1.7}$$

where $d_{\rm A}$ is the angular diameter distance (introduced later), combining the latter quantities, it can be shown that the measured galaxy seperations scale with the cosmological model via the distance measure

$$D_V(z) = \left[r_{\_}^2(z)r_{\_}(z)\right]^{1/3} = \left[\frac{(1+z)^2 d_{\rm A}^2(z)cz}{H(z)}\right]^{1/3}. \tag{1.8}$$

More recently, [70, 67] measured D_V at two redshifts, $z = 0.2$ and $z = 0.35$ ([65] did this just for $z = 0.35$), using SDSS and the Two Degree Field Galaxy Redshift Survey (2DFGRS). The right panel of Fig. 1.4 shows the recent results from [67], where they plot $S_k(1098)/D_V(z)$ (top), $r_s/D_V(z)$ (middle) and $D_V(z)/D_V(0.2)$ (bottom), where $S_k(1089)$ is the comoving angular diameter distance to last scattering (decoupling) and r_s is the comoving sound horizon scale at recombination. Again, we see consistency here with the ΛCDM model.

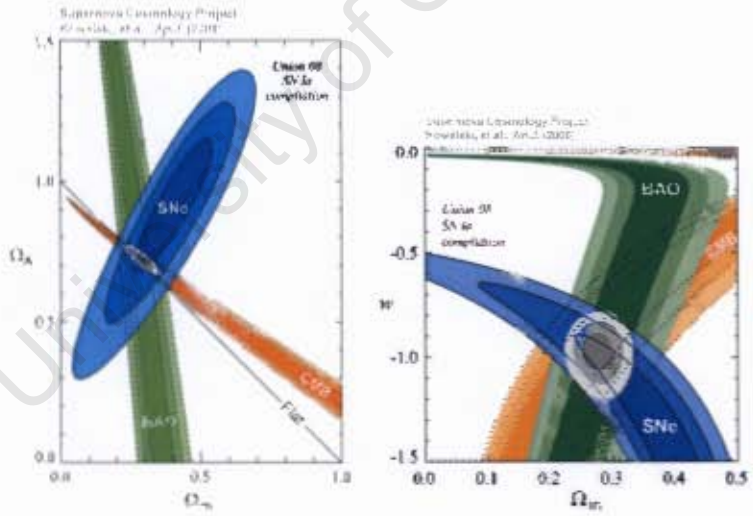

Figure 1.5: Left panel: 68.3%, 95.4% and 99.7% confidence level contours on Ω_Λ and Ω_M obtained from SN, BAO and CMB data, as well as their combination. Right panel: Confidence level contours on w and Ω_M, assuming a flat Universe. From [45].

[4] In reality, radial and angular scales on the sky generally differ, and is known as the Alcock-Paczynski effect [66].

In Fig. 1.5 we show individual and combined constraints on the degeneracies between the matter and vacuum energy densities, and the equation of state parameter and the matter energy density, from recent CMB, BAO and SN measurements. Now, although acceleration ($q_0 = q(z-0) < 0$) is predicted by the ΛCDM model, an interesting study [71], which parameterized dark energy in the so-called CPL form[5], $w = w_0 + w_a \frac{z}{1+z}$, recently revealed, as shown in Fig. 1.6, a discrepancy with that of the ΛCDM model. Instead of having $q_0 < 0$, [71] found $q_0 > 0$ from recent SN+BAO constraints (left), hinting towards the possibility that the universe may, in fact, be currently decelerating, and that the constant w assumption in the ΛCDM model, at least, could be a very restictive or perhaps incorrect one — but the quest remains. Of course, the CMB constrains the (angular diameter) distance to the surface of last scattering [11] — making it a stringent observational test for cosmological models — and, although not allowing a present-day effective deceleration[6] (right panel Fig. 1.6), the possiblity of the slowing of the expansion rate, at least, can be seen by the 'turn-over' in the gradient of q at low redshift that may lead to an eventual deceleration (i.e. $q_0 > 0$) in the future. In fact, we shall return to this quantity later, since our void models produce the same effective $q(z)$ as shown in Fig. 1.6.

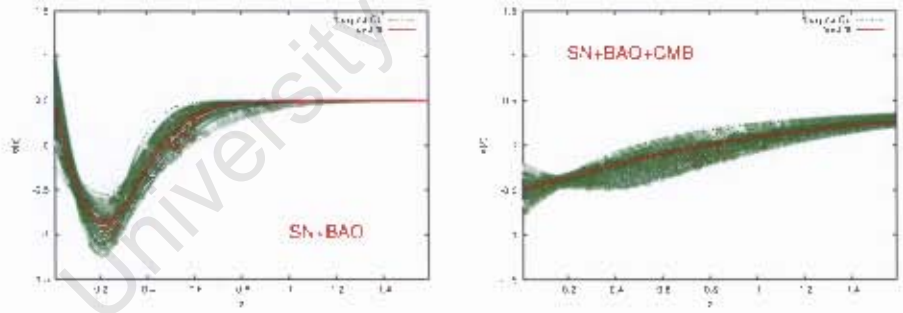

Figure 1.6: Effective $q(z)$ from SN+BAO (left) and SN+BAO+CMB (right) data using the CPL anzatz. The red curves indicate the best-fit model, and the green lines represent the models within 1-σ. Notice the current decelerated expansion (left) i.e. $q_0 > 0$, as expected in a universe with only matter. From [71].

[5]FLRW models that consider a varying equation of state for dark energy (with redshift) go by the term wCDM models. The CPL parameterization is one of many that has been studied in the literature.

[6]The CPL parameterization for DE is a special one, and, in particular, the CMB constrains it tightly at low redshift

Chapter 2

Cosmological Models

2.1 Friedmann-Lemaître-Robertson-Walker (FLRW) Spacetimes

In this section, we outline the basic features of the FLRW cosmology, the bulk of which can be found in modern-day cosmology textbooks such as [127]. In particular, we shall introduce the ΛCDM concordance model, due to its remarkable agreement with the numerous cosmological observations we have to date (see Fig.'s 1.1, 1.2, 1.3, 1.4 and 1.5). This model has undoubtedly set the stage for understanding the history, evolution and fate of our universe, and its dynamics is governed by the Einstein Field Equations (EFE):

$$G_{\mu\nu} \equiv R_{\mu\nu} - \frac{1}{2} g_{\mu\nu} R = 8\pi G T_{\mu\nu} - \Lambda g_{\mu\nu} \,, \tag{2.1}$$

where $G_{\mu\nu}$ is the Einstein tensor, $R_{\mu\nu}$ the Ricci tensor, R the Ricci scalar, G is Newton's gravitational constant, $T_{\mu\nu}$ the energy-momentum tensor and Λ is Einstein's (infamous) cosmological constant. The quantity $g_{\mu\nu}$ is the metric tensor, and determines the distance between events in spacetime as shown by the infinitesmal spacetime interval (or line element)

$$ds^2 = g_{\mu\nu} dx^\mu dx^\nu \,, \tag{2.2}$$

where x^μ represents the 4-dimensional spacetime coordinate. For simplicity we have set the speed of light $c = 1$ in Eq.(2.1), and shall continue with this convention throughout.

2.1.1 The Unperturbed FLRW Metric

Measurements from the Wilkinson-Microwave-Anisotropy-Probe (WMAP) of the CMB temperature fluctuations (see left panel Fig. 1.3) provide strong evidence that, on the largest scales, our universe is nearly isotropic (in fact, to 1 part in 10^5!). If we then assume that our place in the cosmos is not unique, i.e. the Copernican Principle holds, then the universe is forced to be (nearly) homogeneous. The line element describing a perfectly homogeneous and isotropic universe is given by the FLRW metric, written in spherical coordinates (t, r, θ, ϕ) as

$$ds^2 = -dt^2 + a^2(t)\left[\frac{dr^2}{1-kr^2} + r^2 d\Omega^2\right], \tag{2.3}$$

where t is proper time, r is comoving distance, $a(t)$ is the scale-factor determining the physical size of the universe and $d\Omega^2 = d\theta^2 + \sin^2\theta d\phi^2$ is the solid angle squared. The constant k characterizes the 3-dimensional spatial curvature of the universe, and takes on values -1, 0, or 1 depending on whether the universe is open/negatively curved (3-hyperboloid), spatially flat (Minkowski), or closed/positively curved (3-sphere), respectively[1]. The scale-factor $a(t)$ is an unknown in the above equation, and is determined by solving the EFE for a given matter/energy content usually chosen to be that of a perfect fluid,

$$T_{\mu\nu} = (\rho + p)u_\mu u_\nu + p g_{\mu\nu}\,, \tag{2.4}$$

where $\rho = \rho(t)$ is the physical energy density and $p = p(t)$ the pressure (as measured in the rest frame), and u^μ is the four-velocity of the fluid. In general, there is more than one fluid contributing to the total $T_{\mu\nu}$. Moreover, each fluid is often described to have a very simple barotropic equation of state (EOS) (i.e. $p = p(\rho)$) that is of the linear form

$$p = w\rho\,, \tag{2.5}$$

where w is known as the EOS parameter. Conservation of energy ($\nabla_\mu T^\mu_0 = 0$) then leads to the continuity equation

$$\frac{\dot{\rho}}{\rho} = -3(1+w)\frac{\dot{a}}{a}\,, \tag{2.6}$$

[1]Note that this has nothing to do with the global topology of the universe, only its geometric curvature, which determines whether geodesics propagating initially parallel diverge ($k = -1$), remain parallel ($k = 0$), or converge ($k = +1$).

where an over-dot denotes differentiation with respect to t, which upon integration yields

$$\rho = \rho_0 \left(\frac{a}{a_0}\right)^{-3(1+w)}, \tag{2.7}$$

where ρ_0 and a_0 are the values of the energy density and scale factor today, respectively. The ΛCDM model consists of three components that can be modelled by a perfect fluid, namely radiation (neutrinos + photons), matter (ordinary + dark) and the cosmological constant[2] or vacuum energy, whose EOS parameters are given by $w = 1/3$, 0 and -1, respectively.

2.1.2 The Field Equations

In what follows, we shall ignore the energy density due to radiation, as it was only significant at very early times (i.e. before decoupling). The EFE are then given by the well known Friedmann

$$\left(\frac{\dot{a}}{a}\right)^2 = \frac{8\pi G}{3}\rho_M - \frac{k}{a^2} + \frac{\Lambda}{3}, \tag{2.8}$$

and Raychaudhuri

$$\frac{\ddot{a}}{a} = -\frac{4\pi G}{3}\rho_M + \frac{\Lambda}{3}, \tag{2.9}$$

equations, where ρ_M is the energy density of matter (i.e. baryons plus dark matter). The quantity $\left(\frac{\dot{a}}{a}\right)$ in (2.8) defines the Hubble parameter, H, which measures the rate at which the universe is expanding normalized to its size. Eq. (2.9) is also referred to as the acceleration equation, since we define the deceleration parameter[3] as

$$q \equiv -\frac{a\ddot{a}}{\dot{a}^2} = -\frac{\ddot{a}}{aH^2} = \frac{4\pi G}{3H^2}\rho_M - \frac{\Lambda}{3H^2}, \tag{2.10}$$

which measures the rate at which the rate of expansion is changing. Another particularly useful quantity is the (dimensionless) total density parameter,

$$\Omega_{\text{tot}} \equiv \Omega_M + \Omega_\Lambda = \frac{8\pi G}{3H^2}\rho_{\text{tot}} = \frac{\rho_{\text{tot}}}{\rho_{\text{crit}}}, \tag{2.11}$$

where $\rho_{\text{tot}} \equiv \rho_M + \rho_\Lambda$. The critical density is defined by

$$\rho_{\text{crit}} = \frac{8\pi G}{3H^2}, \tag{2.12}$$

[2]Note that the physical energy density of the cosmological constant remains constant at all times, and can be shown to be given by $\rho_\Lambda = \frac{\Lambda}{8\pi G}$.

[3]So called due to common belief at that time that the acceleration of the universe should be slowing down, i.e. decelerating, since a universe dominated by pressureless matter would do so.

and termed so due to its affect on the FE (2.8) divided by H^2 throughout

$$\Omega_{\text{tot}} - 1 = \frac{k}{a^2 H^2} \equiv -\Omega_K \,, \tag{2.13}$$

since it determines the geometry of the universe as demonstrated below:

$$\rho < \rho_{\text{crit}} \;\leftrightarrow\; \Omega_{\text{tot}} < 1 \;\leftrightarrow\; k = -1 \;\leftrightarrow\; \Omega_K > 0 \;\leftrightarrow\; \text{open} \tag{2.14}$$

$$\rho = \rho_{\text{crit}} \;\leftrightarrow\; \Omega_{\text{tot}} = 1 \;\leftrightarrow\; k = 0 \;\leftrightarrow\; \Omega_K = 0 \;\leftrightarrow\; \text{flat} \tag{2.15}$$

$$\rho > \rho_{\text{crit}} \;\leftrightarrow\; \Omega_{\text{tot}} > 1 \;\leftrightarrow\; k = +1 \;\leftrightarrow\; \Omega_K < 0 \;\leftrightarrow\; \text{closed}\,. \tag{2.16}$$

Now, using Eq.'s (2.11), (2.8), (2.10) and (2.7) we can write down the FE in terms of present day quantities:

$$H^2 = H_0^2 \left[\Omega_{M0} \left(\frac{a_0}{a} \right)^3 + \Omega_{K0} \left(\frac{a_0}{a} \right)^2 + \Omega_{\Lambda_0} \right] , \tag{2.17}$$

where Ω_{M0}, Ω_{K0} and Ω_{Λ_0} are the dimensionless matter, curvature and vacuum energy density parameters today, and H_0 is Hubble's constant. Fixing the value of the scale factor today $a_0 = 1$ by convention, these present day values can be obtained by comparing with observational measurements.

Returning to the deceleration parameter, we can use Eq.'s (2.11), (2.10) and (2.7) to write q in a neat and compact form in terms of the dimensionless energy density parameters:

$$q = \frac{1}{2} \left(\Omega_M - 2\Omega_\Lambda \right) , \tag{2.18}$$

which can also be expressed purely in terms of present densities using Eq. (2.17) and the relation

$$\Omega_i = \Omega_{i,0} \left(\frac{H_0}{H} \right)^2 a^{-3(1+w_i)} , \tag{2.19}$$

which is true for both matter and the vacuum. We can also determine q purely from the Hubble rate and its derivative:

$$\begin{aligned} H \equiv \frac{\dot{a}}{a} \Rightarrow \dot{H} &= \frac{\ddot{a}}{a} - \left(\frac{\dot{a}}{a} \right) \\ &= \frac{\ddot{a}}{a} - H^2 \,. \end{aligned} \tag{2.20}$$

Substituting in the definition of q into the latter, we find

$$q = -\left(\frac{\dot{H}}{H^2} + 1 \right) . \tag{2.21}$$

Let us now turn to explaining how we go about comparing our models with the observations.

2.1.3 The Redshift and Distances in Cosmology

In an expanding universe, it is more practical to work with redshift z as it is easier to measure than the scale factor $a(t)$. The redshift of a luminous source, e.g. a galaxy, is defined as

$$z = \frac{\lambda_0 - \lambda_e}{\lambda_e}\,, \tag{2.22}$$

where λ_0 is the wavelength of the source as observed here on earth today, and λ_e is the wavelength emitted by the remote source at some earlier time t_e. Now, in what follows, it is more convenient to rewrite the FLRW metric in the following form:

$$ds^2 = -dt^2 + a^2(t)\left[d\chi^2 + S^2(\chi)d\Omega\right]\,, \tag{2.23}$$

where χ is the comoving coordinate distance, obtained by integrating the constraint equation for radial light rays (radial null geodesics, which have $ds^2 = 0$ and $d\Omega = 0$)

$$\chi \equiv \int_0^r \frac{dr}{\sqrt{1-kr^2}} = -\int_{t_0}^{t_e} \frac{dt}{a(t)}\,, \tag{2.24}$$

$$= \begin{cases} \sin^{-1} r & \text{for} \quad k = +1 \\ r & \text{for} \quad k = 0 \\ \sinh^{-1} r & \text{for} \quad k = -1\,, \end{cases} \tag{2.25}$$

and the function $S(\chi)$ is given by

$$S(\chi) = \begin{cases} \sin\chi & \text{for} \quad k = +1 \\ \chi & \text{for} \quad k = 0 \\ \sinh\chi & \text{for} \quad k = -1\,. \end{cases} \tag{2.26}$$

We can also define the proper distance to this object at some time t, given by

$$d_p(t) = a(t)\chi\,. \tag{2.27}$$

If we now consider another light ray emitted a small time later $t_e' = t_e + \delta t$ and received a small time later $t_0' = t_0 + \delta t_0$, equating the rhs of (2.24) for these two rays we have[4]

$$\int_{t_e'}^{t_0'} \frac{dt}{a(t)} = \int_{t_e}^{t_0} \frac{dt}{a(t)}\,, \tag{2.28}$$

[4]By definition, the lhs of (2.24), which corresponds to comoving coordinate distance, is fixed for each source as it is not affected by the expansion $a(t)$.

which, for small δt and hence small δt_0 gives us

$$\frac{\delta t_0}{a_0} = \frac{\delta t}{a}\,. \tag{2.29}$$

If, in fact, the frequency of the emitted light is given by $\nu_e = 1/\delta t$ and that of the received light by $\nu_0 = 1/\delta t_0$, then we have that

$$\nu_0 a_0 = \nu_e a\,, \tag{2.30}$$

or equivalently

$$\frac{a_0}{\lambda_0} = \frac{a}{\lambda_e}\,, \tag{2.31}$$

which we can then use to relate the redshift of a source to the size of the universe:

$$1 + z = \frac{a_0}{a}. \tag{2.32}$$

Now, we can obtain a useful relation between a redshift interval dz, and time interval dt, by differentiating the latter as follows:

$$dz = d(1+z) = d\left(\frac{a_0}{a}\right) = -\frac{a_0}{a^2}\dot{a}dt = -(1+z)H(z)dt\,. \tag{2.33}$$

The comoving coordinate distance to the source as a function of redshift is then given by

$$\chi(z) = -\int_{t_0}^{t_e} \frac{dt}{a(t)} = \frac{1}{a_0}\int_0^z \frac{dz}{H(z)}\,, \tag{2.34}$$

which can then be written purely in terms of redshift and present day quantities using (2.17) and (2.32):

$$\chi(z) = \frac{1}{H_0}\int_0^z \frac{dz}{\sqrt{\Omega_{M0}(1+z)^3 + \Omega_{K0}(1+z)^2 + \Omega_{\Lambda_0}}}\,, \tag{2.35}$$

where we set $a_0 = 1$. Although we have defined two distances, they are not practical in the sense that it not possible to go out and measure, say, proper distances as one would need to be able to hit the pause button on the expansion of the universe and physically measure the distance to an object using an extraordinarily long ruler. Thus, instead, we need to make use of the actual observable characteristics of an object such as its luminosity and size to make any progress.

The first such quantity we shall define is the angular diameter distance d_{A} of a source. Let's suppose that, in an FLRW universe, a given source has proper diameter l, and that it is a distance d away from us. If we assume, however, that spacetime is not curved (i.e Euclidean space), the source would subtend an angle $\Delta\theta = D/d$,

where D is its proper diameter in flat space. The angular diameter distance is thus defined in general as

$$d_{\rm A} = \frac{l}{\Delta\theta}\,, \tag{2.36}$$

where l is found by integrating the angular part of the metric over the angle θ ($dt = d\chi = d\phi = 0$)

$$l \equiv \int \sqrt{|g_{\theta\theta}|}d\theta = \int a(t)S(\chi)d\theta = a(t)S(\chi)\Delta\theta\,. \tag{2.37}$$

Substituting the latter into (2.36) we then obtain the more general formula for angular diameter distance

$$d_{\rm A} = a(t)S(\chi) = \frac{S(\chi)}{1+z}\,. \tag{2.38}$$

The second such quantity, and one which is used more often, is that of the luminosity distance $d_{\rm L}$ of a source:

$$d_{\rm L} \equiv \left(\frac{L}{4\pi F}\right)^{1/2}, \tag{2.39}$$

which derives from the simple inverse-square law for the dimming of a light source in Euclidean space, where L is its intrinsic (or absolute) luminosity (measured in $W = J.s^{-1}$), and F is the corresponding flux we receive (measured in Wm^{-1}). Now, let's consider an emitting source E with fixed comoving distance d_c relative to an observer O. Let's also assume that the absolute luminosity of E changes over time and is given by $L(t)$, and that the photons it emits reach O at cosmic time t_0. We also assume that the radiation is isotropic, and propagates through O as a sphere centered on E, whose proper area is given by

$$A = 4\pi a^2(t_0)S^2(\chi)\,. \tag{2.40}$$

Of course, the photons have to have been emitted some time t_e earlier, and thus their frequency is redshifted, causing O to measure

$$\nu_0 = \frac{\nu_e}{1+z}\,, \tag{2.41}$$

consequently reducing the arrival rate of photons to decrease by the same factor. Thus, the observed flux at O is then (with $a(t_0) = a_0 = 1$)

$$F(t_0) = \frac{L(t_e)}{4\pi S^2(\chi)}\frac{1}{(1+z)^2}\,, \tag{2.42}$$

so that the corresponding luminosity distance is given by

$$d_{\rm L} = (1+z)S(\chi)\,. \tag{2.43}$$

From (2.38) and (2.43) we obtain the reciprocity theorem,

$$d_{\rm L} = (1+z)^2 d_{\rm A}\,, \tag{2.44}$$

which is valid in all metric theories of gravity.

2.1.4 The Look-back Time and Age of the Universe

Using Eq. (2.33), we can define the 'look-back' time $t_0 - t$ of a comoving particle (galaxy) that emitted a photon at some early time t which is received by an observer today at $t = t_0$, as a function of the photon's redshift by

$$t_0 - t = \int_t^{t_0} dt \equiv \int_0^z \frac{dz}{(1+z)H(z)} \tag{2.45}$$

$$= \frac{1}{H_0}\int_0^z \frac{dz}{(1+z)\sqrt{\Omega_{M0}(1+z)^3 + \Omega_{K0}(1+z)^2 + \Omega_{\Lambda_0}}}\,, \tag{2.46}$$

We can also define a more important quantity using the latter, namely the age of the universe t_0. If we set $z = \infty$ in the above integral, the time coordinate (as well as the scale factor of course, as this is when the big bang occured) goes to zero, and the age of the universe is given by

$$t_0 = \int_0^{t_0} dt \equiv \frac{1}{H_0}\int_0^\infty \frac{dz}{(1+z)\sqrt{\Omega_{M0}(1+z)^3 + \Omega_{K0}(1+z)^2 + \Omega_{\Lambda_0}}}\,. \tag{2.47}$$

It should be noted here that density due to radiation Ω_r, which scales as $\Omega_{r_0}(1+z)^{-3}$, has been omitted since we shall be focussing on the dynamics of the late-time universe (i.e. since matter domination $\approx$ 380 000 years after the BB), but should be taken into account to determine a more accurate age estimate of the universe.

2.2 Lemaître-Tolman-Bondi (LTB) Spacetimes

In this section, we introduce the theory behind inhomogeneous, spherically symmetric matter-dominated LTB models, which have served as good toy models for reproducing many of the cosmological observations without DE. The approach we have taken to solve many of the equations in this spacetime can be found in [138,139], which provides a cosmology-friendly view of the LTB equations that can be easily compared with the standard FLRW ones.

2.2.1 The Unperturbed LTB Metric and Field Equations

In keeping with the high degree of isotropy on large scales, as indicated by the tiny CMB temperature anisotropies, but dropping the CP assumption, the line element describing a dust-filled inhomogeneous universe which is spherically symmetric about its center (only) can be written in general as [7,8,9]

$$ds^2 = -dt^2 + X^2 dr^2 + R^2 d\Omega^2 \tag{2.48}$$

where $X \equiv X(t,r)$ and $R \equiv R(t,r)$ are arbitrary functions of (proper) time t and (comoving) radial position r, and $d\Omega^2 = d\theta^2 + \sin^2\theta d\phi^2$ as before. The FLRW metric, being a special case of the LTB metric, can be recovered by setting

$$X(t,r) \to \frac{a(t)}{\sqrt{1-kr^2}},\ R(t,r) \to a(t)r. \tag{2.49}$$

Since we only consider pressure-less matter (or dust) to be present, the energy momentum tensor takes the simple form

$$T^{\mu}{}_{\nu} = -\rho_{_M}\delta^{\mu}_0\delta^0_{\nu}, \tag{2.50}$$

where $\rho_{_M} \equiv \rho_{_M}(t,r)$ is the matter density and $u^{\mu} = \delta^{\mu}_0$ represents the 4-velocity of the fluid. The corresponding EFE for the given line element (2.48) are given by:

$$-2\frac{R''}{RX^2} + 2\frac{R'X'}{RX^3} + 2\frac{\dot{X}\dot{R}}{AX} + \frac{1}{R^2} + \left(\frac{\dot{R}}{R}\right)^2 - \left(\frac{R'}{RX}\right)^2 = 8\pi G\rho_{_M}\,, \tag{2.51}$$

$$\dot{R}' = R'\frac{\dot{X}}{X}\,, \tag{2.52}$$

$$2\frac{\ddot{R}}{R} + \frac{1}{R^2} + \left(\frac{\dot{R}}{R}\right)^2 - \left(\frac{R'}{RX}\right)^2 = 0\,, \tag{2.53}$$

and

$$-\frac{R''}{RX^2}+\frac{\ddot{R}}{R}+\frac{\dot{R}\dot{X}}{RX}+\frac{R'X'}{RX^3}+\frac{\ddot{X}}{X}=0\,, \tag{2.54}$$

of which only three are independent. We can immediately solve Eq. (2.52) to find

$$X=CR'\,, \tag{2.55}$$

where $C\equiv C(r)$ is a function of integration (since we are dealing with partial derivatives). Redefining $C(r)\equiv 1/\sqrt{1+2E(r)}$, we obtain the more familiar expression for the LTB metric [116]:

$$ds^2=-dt^2+\frac{(R'(t,r))^2}{1+2E(r)}dr^2+R^2(t,r)d\Omega^2\,, \tag{2.56}$$

where $E\geq -\frac{1}{2}$ has both a geometric and a dynamic role, determining the local embedding angle of spatial slices as well as the local energy per unit mass of dust particles, respectively, and R is defined as the areal radius, which in LTB models is equivalent to the angular diameter distance (the rule of thumb is that the angular diameter distance is given by the quantity that multiplies the solid angle in the metric, which, as we saw previously is given by $a(t)S(\chi)$ in FLRW models). Substituting Eq. (2.55) into Eq.'s (2.51) and (2.53) gives us

$$\frac{\dot{R}^2-2E}{R^2}+\frac{2\dot{R}\dot{R}'-2E'}{RR'}=8\pi G\rho_{_M} \tag{2.57}$$

and

$$\dot{R}^2+2R\ddot{R}-2E=0\,, \tag{2.58}$$

respectively. Since we can obtain Eq. (2.54) from (2.55), (2.57) and (2.58), our original set of equations (2.51)−(2.54) reduces to only two independent equations, namely (2.57) and (2.58). Integrating the latter once gives

$$\frac{\dot{R}^2}{R^2}=\frac{M}{R^3}+2\frac{E}{R^2} \tag{2.59}$$

where $M=M(r)$ is another function of integration, usually defined as the effective gravitational mass. Substituting Eq. (2.59) into (2.57) we find that

$$8\pi G\rho_{_M}=\frac{M'}{R^2R'}. \tag{2.60}$$

Motivated by the form of the FLRW metric (2.3) and the corresponding FE (2.17), we introduce the following variables

$$a_\perp(t,r)\equiv\tfrac{R(t,r)}{r}\,,\quad a_\parallel\equiv(a_\perp r)'\,,\quad \kappa(r)\equiv-\tfrac{2E(r)}{r^2}\equiv-H^2_{\perp_0}(r)\Omega_{\kappa_0}(r)a^2_{\perp_0}(r)\,,$$
$$\tilde{\rho}_{_M}(t,r)\equiv\tfrac{3}{8\pi G}\tfrac{M(r)}{(a_\perp r)^3}\equiv\tfrac{3}{8\pi G}H^2_{\perp_0}(r)\Omega_{_{M0}}(r)\left(\tfrac{a_{\perp_0}(r)}{a_\perp}\right)^3\,, \tag{2.61}$$

to find

$$ds^2 = -dt^2 + \frac{a_\parallel^2(t,r)}{1-\kappa(r)r^2}dr^2 + a_\perp^2(t,r)r^2 d\Omega^2\,, \tag{2.62}$$

and the corresponding analogue of the FE and deceleration

$$H_\perp^2 \equiv \left(\frac{\dot{a_\perp}}{a_\perp}\right)^2 = \frac{8\pi G}{3}\tilde{\rho}_M - \frac{\kappa}{a_\perp^2} \tag{2.63}$$

$$= H_{\perp 0}^2\left[\Omega_{M0}\left(\frac{a_{\perp 0}}{a_\perp}\right)^3 + \Omega_{K0}\left(\frac{a_{\perp 0}}{a_\perp}\right)^2\right]\,, \tag{2.64}$$

where $a_{\perp 0} \equiv a_\perp(t_0, r)$ is the present day scale factor, $H_{\perp 0} \equiv H_\perp(t_0, r)$ the corresponding Hubble rate and we made use of the constraint $\Omega_{M0} + \Omega_{K0} = 1$. Notice how this new form of the LTB metric (2.62) makes it clear that we are indeed dealing with two different expansion rates here, i.e. in the directions tangential ($H_\perp \equiv \dot{a_\perp}/a_\perp$) and longitudinal ($H_\parallel \equiv \dot{a_\parallel}/a_\parallel$) to the surfaces of spherical symmetry. Substituting our new variables and above definitions into (2.57), we find that the longitudinal Hubble rate is given by

$$H_\parallel = \frac{1}{2}\left\{\frac{1}{H_\perp}\left[8\pi G\rho_M - \left(\frac{\kappa}{a_\perp^2} - \frac{(\kappa r^2)'}{a_\perp a_\parallel r}\right)\right] - H_\perp\right\}\,, \tag{2.65}$$

where, in terms of our new variables,

$$\rho_M = \frac{[\tilde{\rho}_M(a_\perp r)^3]'}{a_\perp a_\parallel r} = \tilde{\rho}_M + \frac{\tilde{\rho}_M' a_\perp r}{3a_\parallel}\,. \tag{2.66}$$

In addition, using the FLRW form of the dimensional energy density parameter given by Eq. (2.19), we can define latter quantity for matter in LTB models as

$$\Omega_M = \Omega_{M0}\left(\frac{H_{\perp 0}}{H_\perp}\right)^2\left(\frac{a_{\perp 0}}{a_\perp}\right)^3\,. \tag{2.67}$$

We can also write down an effective Raychaudhuri equation in these models, using Eq.'s (2.57) and (2.58):

$$\frac{2}{3}\frac{\ddot{a_\perp}}{a_\perp} + \frac{1}{3}\frac{\ddot{a_\parallel}}{a_\parallel} = -\frac{4\pi G}{3}\rho_M\,. \tag{2.68}$$

Alternatively, we can express the effective acceleration in each direction:

$$\frac{\ddot{a_\perp}}{a_\perp} = -\frac{4\pi G}{3}\tilde{\rho}_M r^3 \quad \text{and} \quad \frac{\ddot{a_\parallel}}{a_\parallel} = -4\pi G\left(\rho_M - \frac{2}{3}\tilde{\rho}_M r^3\right)\,. \tag{2.69}$$

Now, just as we have the freedom to choose the present-day value of the scale factor a_0 in the FLRW case to be any positive number (usually just fixed to 1),

here the scale factor today $a_{\perp_0}$ is allowed to be any smooth and invertible positive function. In particular, we will choose the conventional gauge $R(t_0, r) = r$, which necessarily implies that $a_{\perp_0} = 1$. From Eq. (2.64) it is now obvious that inhomogeneous, isotropic dust models are completely specified by two functions of the radial coordinate, namely the profile of the transverse Hubble parameter today $H_{\perp_0}(r)$ and that of the dimensionless matter density parameter $\Omega_{M_0}(r)$. With the selected gauge, integrating (2.64) from the time of the big bang $t_B \equiv t_B(r)$ to some later time t yields

$$t - t_B = \frac{1}{H_{\perp_0}} \int_0^{a_\perp(t,r)} \frac{dx}{\sqrt{\Omega_{M_0} x^{-1} + \Omega_{K_0}}}, \tag{2.70}$$

which can be solved parametrically in terms of $\eta = \eta(t, r)$, depending on the sign of Ω_{K_0}. For $\Omega_{K_0} > 0$

$$a_\perp = \frac{\Omega_{M_0}}{2\Omega_{K_0}} (\cosh \eta - 1) \tag{2.71}$$

$$t - t_B = \frac{\Omega_{M_0}}{2H_{\perp_0}\Omega_{K_0}^{3/2}} (\sinh \eta - \eta). \tag{2.72}$$

For $\Omega_{K_0} < 0$

$$a_\perp = \frac{\Omega_{M_0}}{2\Omega_{K_0}} (\cos \eta - 1) \tag{2.73}$$

$$t - t_B = \frac{\Omega_{M_0}}{2H_{\perp_0} (-\Omega_{K_0})^{3/2}} (\eta - \sin \eta). \tag{2.74}$$

Finally, for $\Omega_{K_0} = 0$, a parametric solution is not required, and we find

$$a_\perp = \frac{\left(18\Omega_{M_0} H_{\perp_0}^2\right)^3 (t - t_B)^{2/3}}{2}. \tag{2.75}$$

2.2.2 Light Rays and Distances

Following the approach in [128] (which was first shown in [9]), but still keeping with the general procedure of [138], we study how light propagates in an inhomogeneous, isotropic matter-dominated (LTB) spacetime in order to later compare our model with the observations. We begin (as we did in the FLRW case) by writing down the constraint equation for *incoming* radial light rays, acheived by setting $ds^2 = 0$ (null geodesic property) and $d\Omega = 0$ (because of 'radial') in (2.62):

$$\frac{a_\parallel dr}{\sqrt{1 - \kappa r^2}} = -dt. \tag{2.76}$$

We then consider two light rays emitted in the same direction, the second one later by a small time-interval τ. Let us then define the equation of the first ray as $t = T(r)$ and that of the second ray $t = T(r) + \tau(r)$. Both rays must obey (2.76), so

$$\frac{a_\parallel(T,r)dr}{\sqrt{1-\kappa r^2}} = -dT\,, \quad \frac{a_\parallel(T+\tau,r)dr}{\sqrt{1-\kappa r^2}} = -d(T+\tau) \tag{2.77}$$

Since $\tau(r)$ was assumed small, we have, to first order in τ,

$$A'(T+\tau,r) = a_\parallel(T,r) + \tau \dot{a_\parallel}(T,r)\,. \tag{2.78}$$

Using (2.78) and the first of (2.77) in the second of (2.77) we obtain

$$\tau\frac{\dot{a_\parallel}(T,r)dr}{\sqrt{1-\kappa r^2}} = -d\tau\,. \tag{2.79}$$

If τ at emission is the period of a wave, then, comparing it with the corresponding period at the point of observation, we obtain

$$\frac{\tau(r_{\rm obs})}{\tau(r_{\rm em})} = 1 + z(r_{\rm em})\,. \tag{2.80}$$

Keeping the observer at a fixed position and considering the sources at two distances, $r_{\rm em}$ and $(r_{\rm em} + dr)$, we find by differentiating the above with respect to r that

$$d\tau = -\frac{\tau}{1+z}dz\,, \tag{2.81}$$

and plugging this back into (2.79) we find that

$$\frac{dr}{dz} = \frac{\sqrt{1-\kappa r^2}}{(1+z)a_\parallel H_\parallel}. \tag{2.82}$$

Plugging the latter into (2.76) we then find

$$\frac{dt}{dz} = -\frac{1}{(1+z)H_\parallel}\,, \tag{2.83}$$

and we can thus determine the relation between the coordinates and observable redshift, i.e. $t(z)$ and $r(z)$, from the pair of differential equations (2.82) and (2.83) and prior knowledge of $a_\parallel(t,r)$ (found by solving Eq. (2.70) for $a_\perp$, and using the relationship $a_\parallel = \partial/\partial r(a_\perp r)$), $H_\parallel(t,r)$ and $k(r)$. Having done this we can then obtain $a_\perp(t(z),r(z))r(z) \equiv a_\perp(z)r(z)$, i.e. the angular diameter distance as a function of redshift, which we can then use to compute any cosmological distance

desired. In particular, we will compute the distance modulus μ defined in the usual way as

$$\mu = 5\log_{10}\left[\frac{d_{\rm L}}{1\ {\rm Mpc}}\right] + 25, \tag{2.84}$$

where $d_{\rm L} \equiv (1+z)^2 a_\perp r$ is the luminosity distance.

Finally note, that in any inhomogeneous universe, it is not possible to tell whether the evolution of a measured quantity is due to the presence of inhomogeneities in the spatial hypersurfaces or just due to pure temporal variation, since we observe along our past null cone which combines these two effects.

2.2.3 The Age of the Universe

The age of the universe in inhomogeneous models is more complicated as it generally depends on position. However, by using the same definition $t_{\rm AGE}(r) \equiv t_0(r) - t_B(r)$, we can carry out the integral on the rhs of (2.70), and obtain an expression for $t_{\rm AGE}$ depending on the sign of Ω_{K0}. For $\Omega_{K0} > 0$

$$t_{\rm AGE} = \frac{\sqrt{\Omega_{K0}} - \Omega_{M0}\sinh^{-1}\sqrt{\frac{\Omega_{K0}}{\Omega_{M0}}}}{H_{\perp_0}\left(\Omega_{K0}\right)^{3/2}}. \tag{2.85}$$

For $\Omega_{K0} < 0$

$$t_{\rm AGE} = \frac{\Omega_{M0}\sin^{-1}\sqrt{\frac{-\Omega_{K0}}{\Omega_{M0}}} - \sqrt{-\Omega_{K0}}}{H_{\perp_0}\left(-\Omega_{K0}\right)^{3/2}}. \tag{2.86}$$

Finally, for $\Omega_{K0} = 0$

$$t_{\rm AGE} = \frac{2}{3H_{\perp_0}}. \tag{2.87}$$

Although, note here that the radiation era is not included in this analysis, and we stress that the true age of the universe in our model should not be taken too seriously – of course, the true age of the universe would be greater in models with radiation included than that of dust-only models. For a recent aacount of LTB models that include pressure, see [129] and references therein.

2.3 FLRW/ΛCDM Diagnostics

We dedicate the last section of this chapter to introducing quantities that will, in the future, serve as very important tools for distinguishing FLRW/ΛCDM models from LTB models.

We begin by defining the standard deceleration parameter which depends purely on the Hubble rate and the observable redshift: Subsitituting Eq. (2.33) into Eq. (2.21), we obtain

$$q(z) = -1 + \frac{(1+z)}{H(z)}\frac{d}{dz}H(z)\,. \tag{2.88}$$

for the deceleration parameter in FLRW models. Now, using the relation between an infinitesimal redshift and time interval in LTB models, Eq. 2.83, we can define an effective deceleration parameter as follows,

$$q^{\text{eff}}(z) = -1 + \frac{(1+z)}{H_{\parallel}(z)}\frac{d}{dz}H_{\parallel}(z)\,, \tag{2.89}$$

where it is anticipated, given the results by [109], that models containing a weak-singularity would have $q_0^{\text{eff}} < 0$, and models without the singularity would give $q_0^{\text{eff}} > 0$. Note that from this point on until the rest of this section only, will be abbreviating d/dz with $'$, and the reader should not be confuse a $'$ with $\partial/\partial r$, as was the case in the previous section.

Returning to the topic of dark energy, Clarkson et al. [130] reconstructed the dark energy equation of state so that it depends solely on observable quantites such as d_{A}, $H_{\perp}$, and their derivatives. Assuming a spatially flat background (i.e. $\Omega_{_K} = 0$), the effective DE equation of state in terms of distance measurements [133] can be written as

$$w_{\text{DE}}^{\text{eff}}(z) = \frac{2(1+z)d_{\text{C}}'' + 3d_{\text{C}}'}{3\left[H_0^2\Omega_{_M}(1+z)^3 d_{\text{C}}'^2 - 1\right]d_{\text{C}}'}\,, \tag{2.90}$$

where $d_{\text{C}} = (1+z)d_{\text{A}}$ is the comoving angular diameter distance, and in terms of the Hubble rate,

$$w_{\text{DE}}^{\text{eff}}(z) = -\frac{2(1+z)HH' - 3H^2}{3\left[H_0^2(1+z)^3\Omega_{_M} - H^2\right]}\,. \tag{2.91}$$

Thus, if we are able to measure d_{A}', d_{A}'' and H', we could use the above reconstructed DE equations of state not only to rule out, or to strengthen the cosmological constant ($w = -1$) hypothesis, but could also determine an effective DE equation of state using those observable quantities as determined from an LTB model.

Finally, we turn the topic of Copernican tests. Testing the validity of the CP is a difficult, yet probably one of the most important tasks to be carried out in cosmology, since the very foundation of the current cosmological concordance model is based on the assumption that the CP holds, which, when combined with the assumption of isotropy, implies that our universe is homogeneous. A number of such tests, completely independent of any model of dark energy or theory of gravity,

constructed only from combinations of observables such as the angular diameter distance, Hubble rate and derivatives thereof have recently been provided in the literature [130,131]. Again, assuming a FLRW background that is spatially flat, the quantities we compute for our best-fit LTB models in chapter 4 are the reconstructed (effective) energy density due to matter [131],

$$\Omega_M^{\rm eff}(z) = \frac{\left[H_\parallel(z)/H_0\right]^2 - 1}{(1+z)^3 - 1}\,, \tag{2.92}$$

the reconstructed energy density due to curvature [132],

$$\Omega_K^{\rm eff}(z) = \frac{\left[d_{\rm c}(z)H_\parallel(z)\right]^2 - 1}{\left[d_{\rm c}(z)H_0\right]^2}\,, \tag{2.93}$$

and the numerators of the derivatives thereof,

$$L(z) = 2\left[(1+z)^3 - 1\right]H_0 d_{\rm c}''(z) + 3(1+z)^2 H_0 d_{\rm c}'(z)\left[1 - (H_0 d_{\rm c}'(z))^2\right]\,, \tag{2.94}$$

and

$$C(z) = 1 + H_\parallel(z)^2\left[d_{\rm c}(z)d_{\rm c}''(z) - d_{\rm c}'(z)^2\right] + H_\parallel(z)H_\parallel'(z)d_{\rm c}(z)d_{\rm c}'(z)\,, \tag{2.95}$$

respectively. The basic idea here is that if we do not live in a homogeneous universe, then at some redshift it is possible to measure values for the above quantities different from that expected in the flat ΛCDM, or FLRW, case, where, for instance, $\Omega_K(z) = L(z) = C(z) = 0$. Since we do have access to $H(z)$ data [23], we can actually compute the corresponding reconstructed Ω_M at those redshifts, and we can calculate the respective errors on this using the standard technique of error propagation[5]. If the spacetime metric describing our universe is indeed given by the FLRW metric, then Ω_M must have zero gradient. However, upon plotting Ω_M corresponding to the $H(z)$ data, we see that, after fitting a straight line to the points shown in Fig. 2.1 (note that the error bars are excluded, since they are enormous), the resulting slope Ω_M is different from zero. Although this seems to indicate a discrepancy from FLRW, there is no way, yet, of determining this with the current precision of $H(z)$ data.

[5]The errors on Ω_M, $\boldsymbol{\sigma}_{\Omega_M}$, given the those of $\boldsymbol{H}$, $\boldsymbol{\sigma}_H$, is given by: $\boldsymbol{\sigma}_{\Omega_M} = \boldsymbol{\sigma}_H\left(\frac{d\Omega_M}{dH}\right)^{1/2}$, where $\frac{d\Omega_M}{dH} = \frac{2H(z)}{H_0^2((1+z)^3-1)}$.

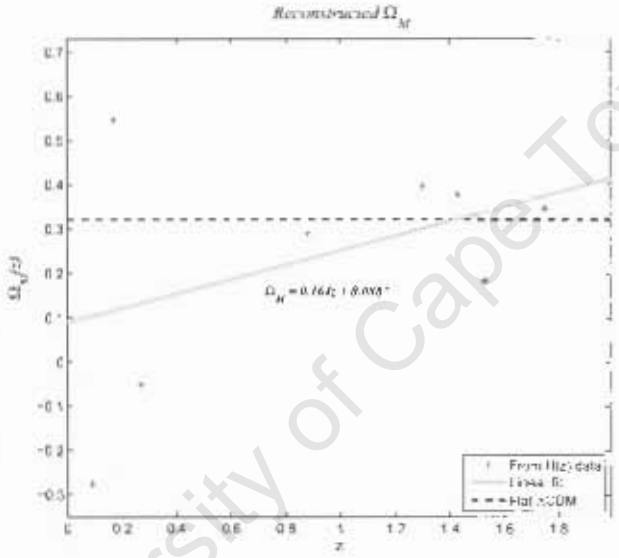

Figure 2.1: Plot of the effective $\Omega_M(z)$ (grey points) using $H(z)$ data showing a positive average gradient (grey line). Since FLRW models should yield a zero gradient for Ω_M, this result hints towards a non-FLRW behaviour of the universe, and may be confirmed with more accurate data in the future.

Chapter 3

Void Investigation

We mentioned in the review on LTB models that [116] proved that for a given FLRW model, there exists an LTB model capable of reproducing the distance modulus of that FLRW model. To summarize further, [113] showed that the curvature parameter of such models needs to be strongly cusped and non-differentiable at the origin (consequently referred to as being unrealistic, although such a scenario is not unnatural at all), whereas [115] showed that the dimensionless density parameter can be smooth (although still fairly cusped) at the origin and still reproduce the FLRW distance modulus curve. In addition, [109] showed that observers living in LTB spacetimes that are non-differentiable at the origin would necessarily observe an accelerated expansion today, whereas models that are differentiable at the origin exhibit a decelerated expansion. Thus, depending on the smoothness of the model at the center, one could obtain different results for the sign of the deceleration parameter today.

To avoid any a priori assumptions of whether the void should be differentiable at the origin or not, we introduce a void parameterization in the next section in which both scenarios are possible, i.e. weak-singularity $\rightarrow$ pointy void $\rightarrow$ acceleration, and no weak-singularity $\rightarrow$ smooth void $\rightarrow$ deceleration. The scenario of no weak-singularity, but a cuspy void is also possible, and would also yield a deceleration. We now introduce this parameterization, as well as other typical smooth profiles, that we have used in an attempt to reproduce μ^{FLRW} (section 3.4), and to fit to data (in the next chapter).

3.1 Parameterizations

The developement of our parameterization was motivated by: the form of the curvature profile [113] used to show its potential to trace out μ^{FLRW}; the fact that [115] showed it was possible to reproduce $\mu^{\Lambda\text{CDM}}$ albeit with a void profile without a weak-singularity at the center; and by the claim made by [113] regarding the testing of the CP using SN alone. We then came up with the following ansatz (from here on referred to as model # 1) for the dimensionless matter density profile today in order to both test the claim made by [113], and to see whether or not the current supernova data prefers steep voids, flat voids, or something in between:

$$\Omega_{M0}(r) = \Omega_{\text{in}} + \frac{\Omega_{\text{out}} - \Omega_{\text{in}}}{\nu - 1}\left[\nu \tanh\frac{r}{\sigma} - \tanh\frac{r\nu}{\sigma}\right], \tag{3.1}$$

where $\Omega_{\text{in}} \equiv \Omega_{M0}(r=0)$, $\Omega_{\text{out}} \equiv \Omega_{M0}(r=\infty)$, σ is related to the size of the void, ν controls how steep/flat the void is around the origin and, when finite, ensures that this function is C^2 at the origin (i.e. its first and second derivatives are zero at $r=0$; under $r \to -r$ this ensures differentiability). We also assume that $\Omega_{M0}(r)$ is even about $r=0$ so that $\Omega_{M0}(-r) \equiv \Omega_{M0}(r)$. Our void profile today then depends on four parameters: Ω_{in}, Ω_{out}, σ and ν. The first two are self-explanatory – the value of Ω_{M0} at the centre of the void and its value at infinity, respectively – but both are strictly positive definite, and in order to describe a void (underdense region), Ω_{in} must be less than Ω_{out}. The parameter σ characterizes the size of the void – the larger σ becomes, the larger the void gets, and so on – however, in general, σ is not necessarily a very descriptive quantity. A more physically useful quantity is the Full Width at Half Maximum (FWHM), calculated by solving

$$\Omega_{M0}\left(\frac{1}{2}r_{\text{FWHM}}\right) = \frac{(\Omega_{\text{out}} + \Omega_{\text{in}})}{2}, \tag{3.2}$$

for r_{FWHM} (numerically). Finally, the parameter ν gives us the power to control the gradient of the void at the origin: the larger ν is, the steeper the void; the smaller ν is, the flatter the void is at the centre. When $\nu = 1$, there is a 'hole' in the function, and we can fill it in to make Ω_{M0} continuous using

$$\Omega_{M0}(r) = \Omega_{\text{in}} + (\Omega_{\text{out}} - \Omega_{\text{in}})\left[\tanh\frac{r}{\sigma} - \frac{r}{\sigma}\text{sech}^2\frac{r}{\sigma}\right], \tag{3.3}$$

where the appropriate limit was taken using l'Hospital's Rule as ν approaches 1. When $\nu = 0$, $\Omega_{M0}(r) = \Omega_{\text{in}}$ and the universe is homogeneous. We restrict $\nu \geq 0$ as its entire meaning breaks down when $\nu < 0$, since the gradient 'jumps' to being

steep again. Our parameterization therefore allows for a smooth transition from an FLRW model (which, to mimick requires a pointy void i.e. ν very large) to a 'realistic' LTB void model (in which ν must be small and finite), and can be used to test whether cosmological data prefers a steep void or not, as opposed to restricting the profile to either being pointy at the origin (see the model by [120] for example), or having a Gaussian smoothness, say. More importantly, however, is whether or not the data prefers a void over ΛCDM, and the answer to that shall be revealed in the next chapter.

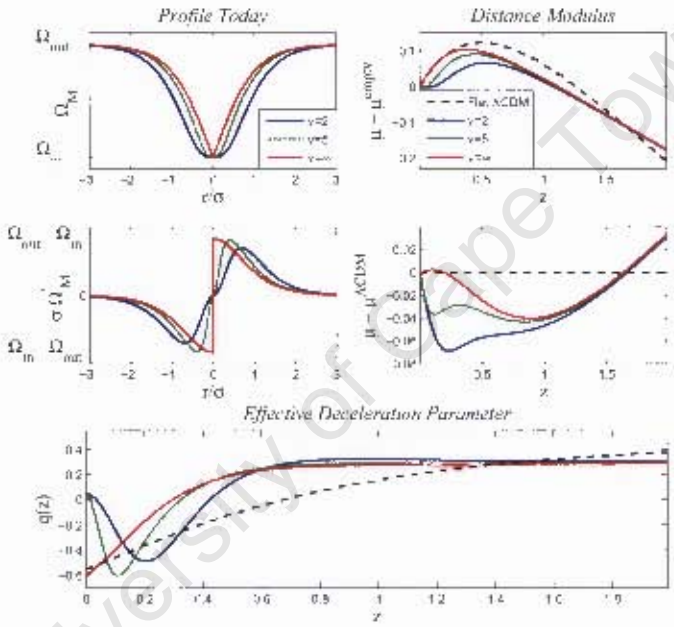

Figure 3.1: Example plots of model #1 illustrating the effects ν has on the slope of the profile (top left) around the origin, the corresponding differentiated profile (middle left), distance modulus (top right) normalized to that of an empty (Milne) universe, difference between the corresponding distance modulus and that of the ΛCDM model (middle right), and finally the effective deceleration parameter (bottom).

As for specifying the profile of the transverse Hubble parameter today, we shall take into account the argument recently posed by Zibin [16], that if we are to set up realistic void profiles which agree with the standard picture of extreme post-inflationary homogeneity, it will be necessary to drop the decaying mode, i.e. fluc-

tuations in the bang time function $t_B(r)$ (see [124]), since otherwise density perturbations would be larger in the past than today, and we would therefore find the early universe to be very inhomogeneous. As a result, the age of the universe t_{AGE} is then a constant, and the time today t_0 is consequently equal to the age of the universe. So, by solving (2.86), (2.85) and (2.87) for $H_{\perp_0}(r)$, we have that:

For $\Omega_{K0} > 0$

$$H_{\perp_0} = \frac{\sqrt{\Omega_{K0}} - \Omega_{M0} \sinh^{-1} \sqrt{\frac{\Omega_{K0}}{\Omega_{M0}}}}{t_0 \left(\Omega_{K0}\right)^{3/2}}. \tag{3.4}$$

For $\Omega_{K0} < 0$

$$H_{\perp_0} = \frac{\Omega_{M0} \sin^{-1} \sqrt{\frac{-\Omega_{K0}}{\Omega_{M0}}} - \sqrt{-\Omega_{K0}}}{t_0 \left(-\Omega_{K0}\right)^{3/2}}. \tag{3.5}$$

Finally, for $\Omega_{K0} = 0$

$$H_{\perp_0} = \frac{2}{3t_0}. \tag{3.6}$$

We then defined the Hubble constant H_0 as being the value of $H_{\perp_0}$ at the origin, i.e. $H_0 \equiv H_{\perp_0}(r = 0)$, whose value in terms of the age of the universe can be found by setting $r = 0$ in Eq.'s (3.4–3.6). Thus, in order to calculate the distance modulus μ for instance, we need to specify Ω_{in}, Ω_{out}, σ, ν and H_0.

In Fig. 3.1 we demonstrate the effect ν has on the distance modulus and the deceleration parameter for three different values of ν, keeping the other parameters, which were chosen specifically for illustration purposes, fixed. In the figure we plot the dimensionless density profile of the void as a function of the comoving radial coordinate r (which has units of Mpc). Below that we plot the derivative of the dimensionless density profile with respect to r multiplied by σ (to make it dimensionless), to show that the void is indeed singular at the origin when $\nu = \infty$. The plot of the corresponding distance modulus (top right) normalized to that of an empty Milne universe (in which $\Omega_M = 0$, $\Omega_\Lambda = 0$ and $\Omega_K = 1$) with the same H_0 as that of the specific model (although H_0 for our model and that of ΛCDM were chosen to be the same in this case, there is a subtlety regarding H_0 that shall be tackled in section 3.3), reiterates the result by [113]: the shape of the distance modulus curve near the origin reflects that of the void profile, and that pointy voids mimick μ^{LCDM} whereas smooth voids deviate from the latter. The plot below the latter shows the difference between μ^{void} and μ^{LCDM}, and illustrates the point further that at low redshifts their exists a characteristic difference in distance moduli between smooth voids and that of ΛCDM. Turning now to the corresponding plot of the effective

deceleration parameter as a function of redshift (bottom panel), we find exactly the result of [109]: LTB models containing a weak-singularity accelerate today (i.e. $q_0 < 0$), whereas models without the weak-singularity decelerate today ($q_0 > 0$).

In addition to parameterization # 1, we also considered the following (smooth) void profiles:

$$\# 2: \quad \Omega_{M0}(r) = \Omega_{\rm out} - (\Omega_{\rm out} - \Omega_{\rm in}) \exp\left[-\left(\frac{r}{\sigma}\right)^2 \right],$$

$$\# 3: \quad \Omega_{M0}(r) = \Omega_{\rm out} - (\Omega_{\rm out} - \Omega_{\rm in}) \frac{\sigma^2}{\sigma^2 + r^2},$$

$$\# 4: \quad \Omega_{M0}(r) = \Omega_{\rm out} - (\Omega_{\rm out} - \Omega_{\rm in}) \frac{\sigma \sin\left(\frac{r}{\sigma}\right)}{r},$$

$$\# 5: \quad \Omega_{M0}(r) = \Omega_{\rm out} - (\Omega_{\rm out} - \Omega_{\rm in}) \frac{\sigma^2 \sin^2\left(\frac{r}{\sigma}\right)}{r^2}.$$

In Fig. 3.2 illustrate the density profiles of models 2, 3, 4 and 5, where we fixed the void parameters to be $\Omega_{\rm in} = 0.1$, $\Omega_{\rm out} = 1$ and $\sigma = 1$ Gpc in each case.

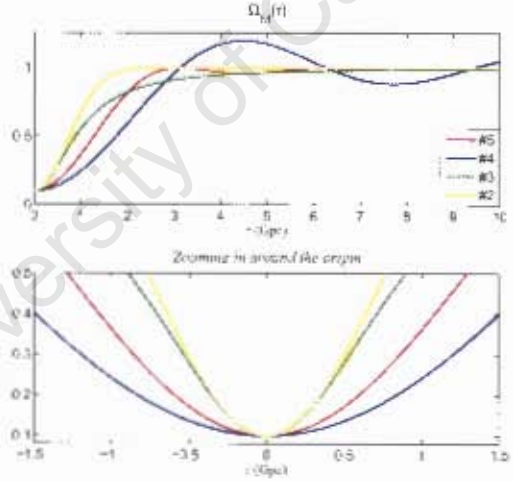

Figure 3.2: Plots of the void profiles 2, 3, 4 and 5 for a fixed set of parameter values to compare their behaviour.

3.2 Evolution of the Void

In this section, we study the behaviour of how a typical void evolves over time. We shall do this as follows: choose a typical void profile today i.e. $\Omega_{M0}(r)$, and using Eq.'s (2.67) and (2.66), evolve the profile backward, as well as forward in time to check that our results agree with the literature [124,96]. We use void model # 1 for illustration purposes, and choose, for argument sake, choose $H_0 = 65.0$ km/s/Mpc, $\Omega_{\text{in}} = 0.1$, $\Omega_{\text{out}} = 1.0$, $\sigma = 2.0$ Gpc and $\nu = 2.0$. In addition, we present the (backward) evolution in the case of in inhomogeneous bang time model, obtained by adding in tiny fluctuations to the Hubble profile today $H_{\perp 0}(r)$.

3.2.1 Backward Evolution

In Fig. 3.3 we plot the dimensionless density $\Omega_M(t(z), r)$ (left) of the void as a function of r for different redshifts, where we made use of Eq. (2.67). We see that at earlier times (larger z), the void was both shallower and narrower, and possessed a larger Ω_M on average than that at later times. The physical density $\rho_M(t(z), r)$ in Fig. 3.4 (left) portrays the same behaviour, and this is characteristic of models with a homogeneous bang time [124,106]. On the right panel of each of the figures just mentioned, we plot the corresponding densities calculated along the past null cone, i.e. $\Omega_M(t(z), r(z))$ and $\rho_M(t(z), r(z))$. As expected, Ω_M tends to 1 (i.e. Einstein de Sitter) at large redshifts, and ρ_M tends to infinity.

We were also interested in the evolution of the density contrast δ_ρ, which we defined as

$$\delta_\rho = \frac{\rho_M(t, r) - \rho(t, \infty)}{\rho(t, \infty)}, \tag{3.7}$$

where $\rho(t, \infty)$ is the background density as a function of time, and show its behaviour in Fig. 3.5. Again, as we go back in time, density fluctuations (δ_ρ) decrease in amplitude, as such agreeing with the study done in [106] (based on the idea posed in [124]), showing that the early universe is approximately homogeneous when $t_B = 0$.

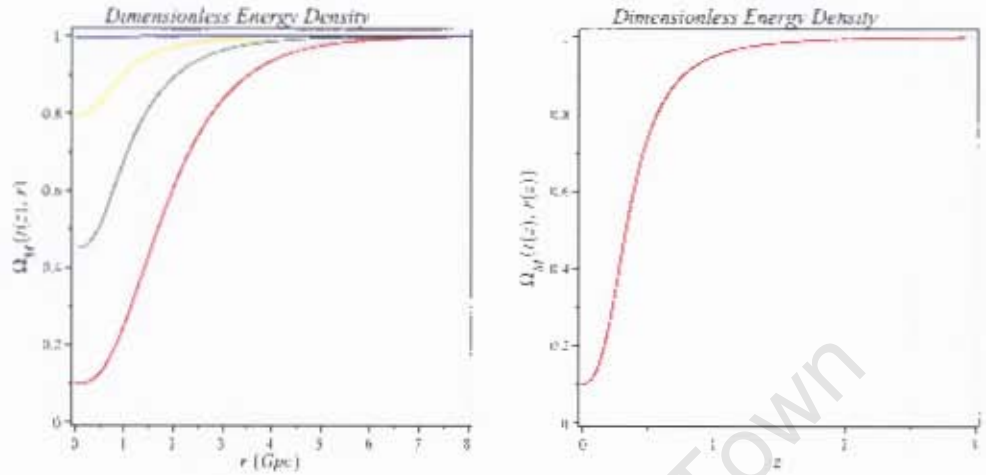

Figure 3.3: Left panel: Plots of the radial dependence of the dimensionless density $\Omega_M(t(z), r)$ of the void as a function of time, corresponding to redshifts $z = 0$ (red), 4 (yellow), 20 (green) and 1000 (blue). Right panel: The corresponding dimensionless density $\Omega_M(t(z), r(z))$ as seen along the past null cone.

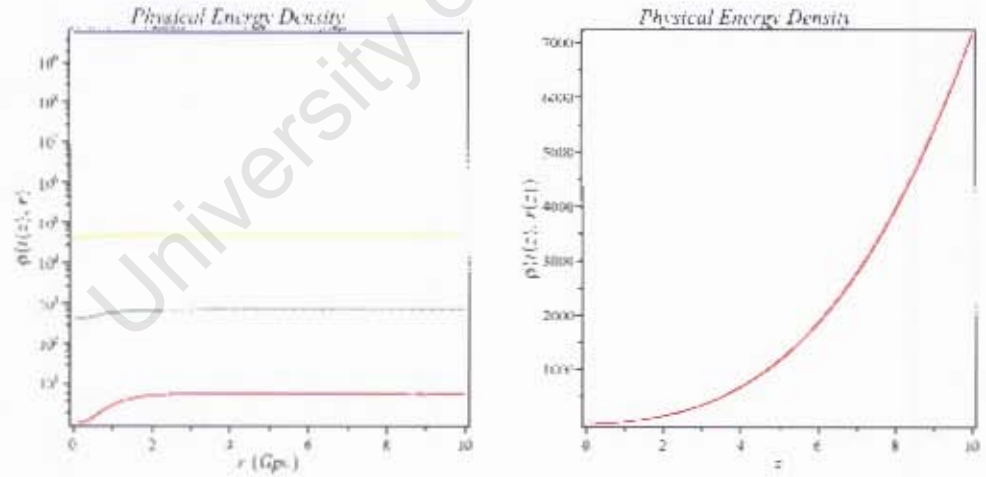

Figure 3.4: Left panel: Plots of the radial dependence of the physical density $\rho_M(t(z), r)$ of the void as a function of time, corresponding to redshifts $z = 0$ (red), 4 (yellow), 20 (green) and 1000 (blue). Right panel: The corresponding physical density $\rho_M(t(z), r(z))$ as seen along the past null cone.

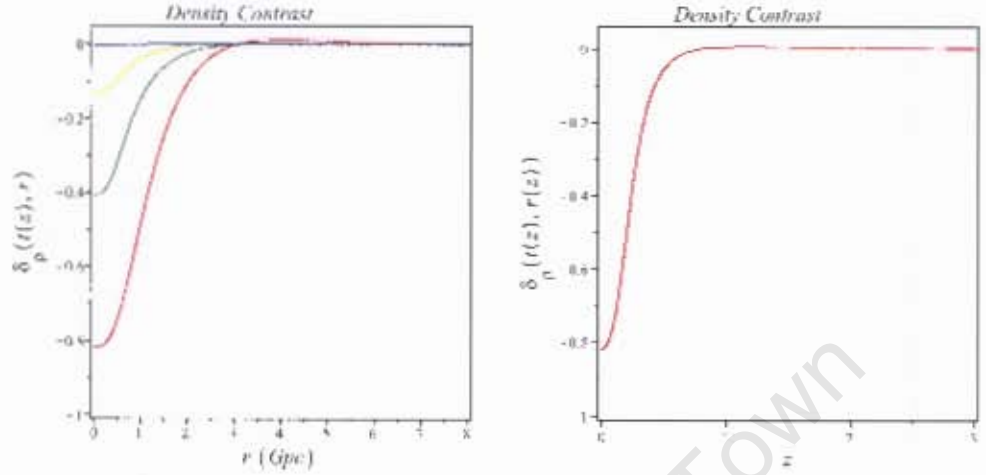

Figure 3.5: Left panel: Plots of the radial dependence of the density contrast $\delta_\rho(t(z), r)$ of the void as a function of time, corresponding to redshifts $z = 0$ (red), 4 (yellow), 20 (green) and 1000 (blue). Right panel: The corresponding density contrast $\delta_\rho(t(z), r(z))$ as seen along the past null cone.

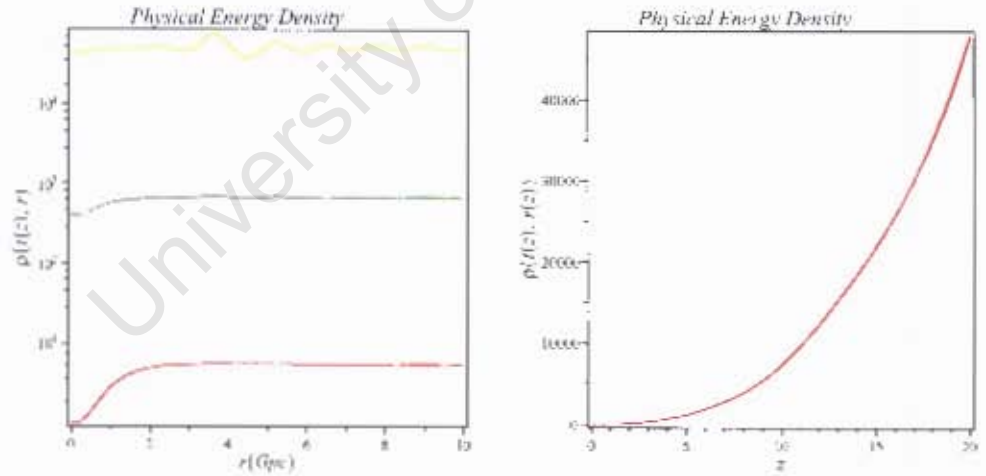

Figure 3.6: Left panel: Plots of the radial dependence of the physical density $\rho_M(t(z), r)$ of the void with an inhomogeneous bang time, as a function of time, corresponding to redshifts $z = 0$ (red), 4 (yellow) and 20 (green). Right panel: The corresponding physical density $\rho_M(t(z), r(z))$ as seen along the past null cone.

In addition, the effects of adding small oscillations in $H_{\perp 0}$ – corresponding to fluctuations in $t_B(r)$ – has on the (backward) evolution of the void was also investigated. The effects of the fluctuation we added is not easily visible in terms of $\Omega_M(r)$, however a plot of the physical density ρ_M as given by Fig. 3.6, as well as the density contrast δ_ρ as shown in Fig. 3.7 offers the desired result: that the presence of even a tiny gradient in t_B today would correspond to a universe that was significantly more inhomogeneous in the past [124].

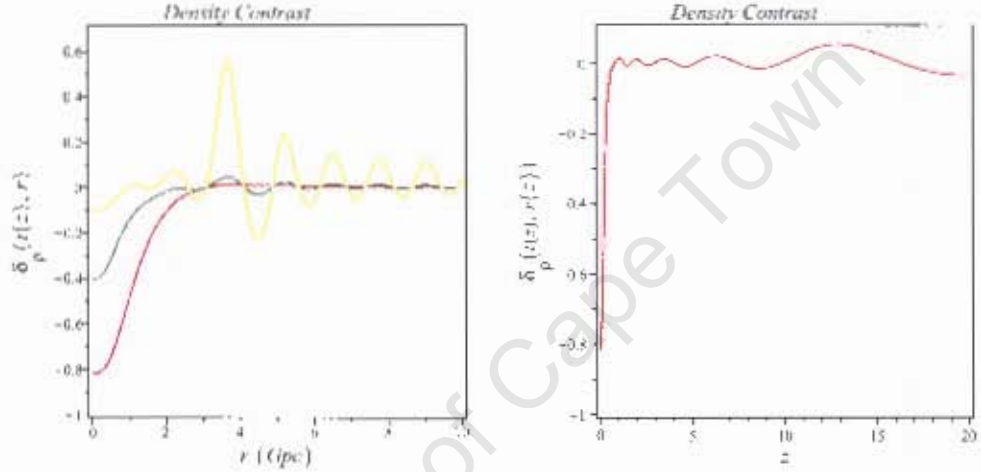

Figure 3.7: Left panel: Plots of the radial dependence of the density contrast $\delta_\rho(t(z), r)$ of the void with an inhomogeneous bang time,as a function of time, corresponding to redshifts $z = 0$ (red), 4 (yellow) and 20 (green). Right panel: The corresponding density contrast $\delta_\rho(t(z), r(z))$ as seen along the past null cone.

3.2.2 Forward Evolution

In Fig.'s 3.8, 3.9 and 3.10 we plot the dimensionless density $\Omega_M(t, r)$, the physical density $\Omega_M(t, r)$ and density contrast $\delta_\rho(t, r)$, respectively, of the void as a function of r for increasing times. We see that as time progresses, the void continues to grow in amplitude as well as width, and eventually starts to exhibit a shell-like feature at (much) later times, in agreement with that found in [166].

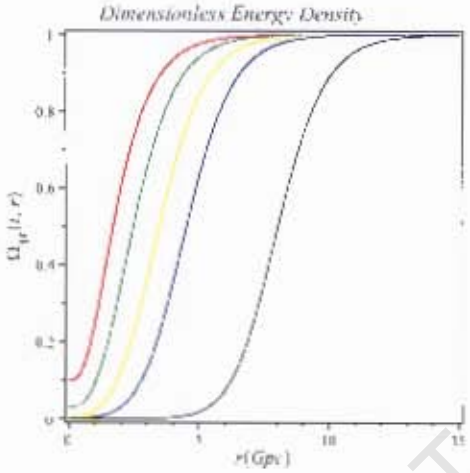

Figure 3.8: Plots of the radial dependence of the dimensionless density $\Omega_M(t(z), r)$ of the void as a function of time, for $t = t_0$ (red), $4t_0$ (yellow), $20t_0$ (green), $100t_0$ (blue) and $20000t_0$(black).

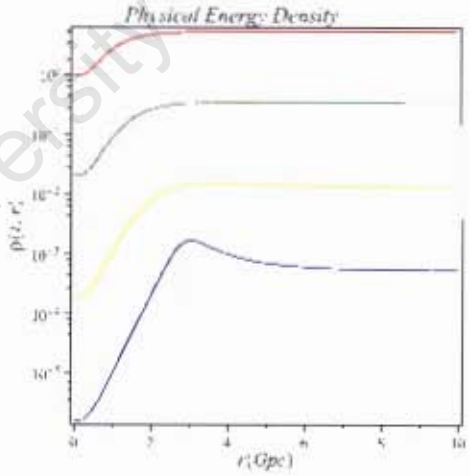

Figure 3.9: Plots of the radial dependence of the dimensionless density $\rho_M(t(z), r)$ of the void as a function of time, for $t = t_0$ (red), $4t_0$ (yellow), $20t_0$ (green) and $100t_0$ (blue).

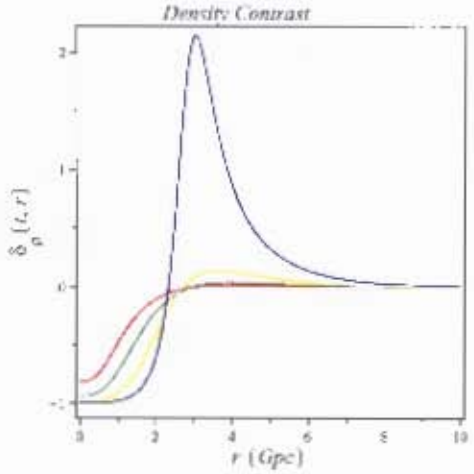

Figure 3.10: Plots of the radial dependence of the density contrast δ_ρ of the void as a function of time, for $t = t_0$ (red), $4t_0$ (yellow), $20t_0$ (green) and $100t_0$ (blue).

3.3 Non-trivial Normalization with H_0

Only very late into our study, we came across a non-trivial normalization issue regarding the distance modulus curve and the value of the transverse Hubble parameter today, at the origin, H_0. In the (flat) FLRW case, since H_0 is just a magnitude offset related to the intrinsic (absolute) luminosity of a SN, it is usually removed from the analysis by marginalizing over it. Of course, if the distance modulus, for instance, is to be calculated, a value for H_0 is required. This is taken care of by not actually computing μ, but μ minus that of an empty Milne universe (with the same H_0), i.e. $\mu - \mu^{\text{empty}}$, since all factors of H_0 drops out: From Eq.'s (1.1),(2.43), the fact that $S(\chi) = \chi$ in flat FLRW models, and Eq. (2.35), we have that

$$\begin{aligned}\mu &= 5\log_{10}\left[\frac{(1+z)}{H_0}\int_0^z \frac{dz}{\sqrt{\Omega_{M_0}(1-z)^3+\Omega_{\Lambda_0}}}\right] - 25 \\ &- 5\log_{10}\left[(1+z)\int_0^z \frac{dz}{\sqrt{\Omega_{M_0}(1+z)^3+\Omega_{\Lambda_0}}}\right] - 5\log_{10} H_0 - 25\,. \qquad (3.8)\end{aligned}$$

Similarly, for the empty (flat) Milne universe (in which $\Omega_{M0} = \Omega_{\Lambda_0} = 0, \Omega_{K_0} = 1$),

$$\begin{aligned}\mu^{\text{empty}} &= 5\log_{10}\left[\frac{(1+z)}{H_0}\int_0^z \frac{dz}{\sqrt{(1+z)^2\Omega_{K_0}}}\right] + 25 \\ &= 5\log_{10}[(1+z)\ln(1+z)] - 5\log_{10} H_0 + 25. \end{aligned} \tag{3.9}$$

Taking the difference we find

$$\mu - \mu^{\text{empty}} = 5\log_{10}\left\{(1+z)\left[\int_0^z \frac{dz}{\sqrt{\Omega_{M0}(1-z)^3 + \Omega_{\Lambda_0}}} - \ln(1+z)\right]\right\}, \tag{3.10}$$

which is completely independent of H_0. In the LTB case, however, we found that H_0 not only determines the value of the function $H_0(r)$ today at the center (recall $H_0(r=0) \equiv H_0$), but also affects its value at infinity. As a result, higher (lower) values of H_0 not only shifts the distance modulus curves down (up), but also changes the overall shape too (because of its dependency on radial position). This is an important issue, and, to the best knowledge of the author, has not been pointed anywhere in the literature. We illustrate this point in Fig 3.11.

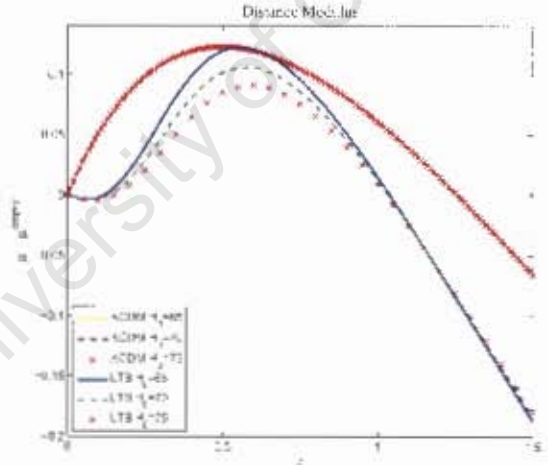

Figure 3.11: Plots of $\mu - \mu^{\text{empty}}$ for FLRW and LTB models for different choices of H_0, to illustrate that, in the LTB case, H_0 not only affects the vertical displacement of $\mu(z)$, but also its shape, and thus we cannot simply marginalize over it as we can in the FLRW case.

Although the actual process of marginalizing over H_0 is a relatively simple one, and as we mentioned above, is done in FLRW models, we have shown here that one

runs the risk of losing vital information as H_0 affects LTB observables at non-zero redshifts too. Further investigation into this matter needs to be carried out, which would involve fitting to the intrinsic SN magnitudes M at the same time, and shall be done in future work.

3.4 Fitting to ΛCDM

In this section, we fit the distance moduli of each of our 5 different void parameterizations to that of the flat ΛCDM model, for different values of the ΛCDM $\Omega_{_M}$. The point of doing this to check whether any of our void parameterizations falls into the category of being capable of reproducing an FLRW model [116], and therefore keep us from distinguishing such a model from the ΛCDM model observationally.

This process was carried out in Maple using a fitting routine provided by its built-in statistics package. Taking (roughly) the redshift range of current SN data, we created a fake set of data given by the flat ΛCDM distance modulus, starting from $z_{min} = 0.1$ and ending at $z_{max} = 1.61$, with a redshift spacing of $\Delta z = 0.01$, such that there are 17 data points as input. Since the option for neglecting errors on the data was available, we opted for that route as the input data is actually a model. As we shall now reveal, decents fits were generally found when we fixed $\Omega_{\text{out}} = 1$, and even better fits when Ω_{out} was allowed to vary.

For the ΛCDM model used here, we chose an $H_0 = 65$ km/s/Mpc. Indeed, a ΛCDM model with a different H_0 would certainly produce different results (recall from the previous subsection, that H_0 in the LTB case not only affects the vertical displacement of the distance modulus curve, but also its overall shape), however, we have left that as a topic for future work.

3.4.1 Fixing $\Omega_{\text{out}} = 1$

In Fig. 3.12 we show the magnitue difference (top panel) and the corresponding perecentage difference (bottom panel) between μ^{void} and $\mu^{\Lambda\text{CDM}}$ as a function of $\Omega_{_{M0}}$ where we fixed $\Omega_{\text{out}} = 1$. It turns out that all 5 void models can reproduce the ΛCDM model well enough to deem them indistinguishable from ΛCDM using SN data. Moreover, when setting $\nu = \infty$ in void model #1, we find that we can fit to the ΛCDM distance modulus to arbitrary accuracy, as already discovered by [113], and is therefore an example of such an LTB model capable of exactly matching $\mu^{\Lambda\text{CDM}}$ [116].

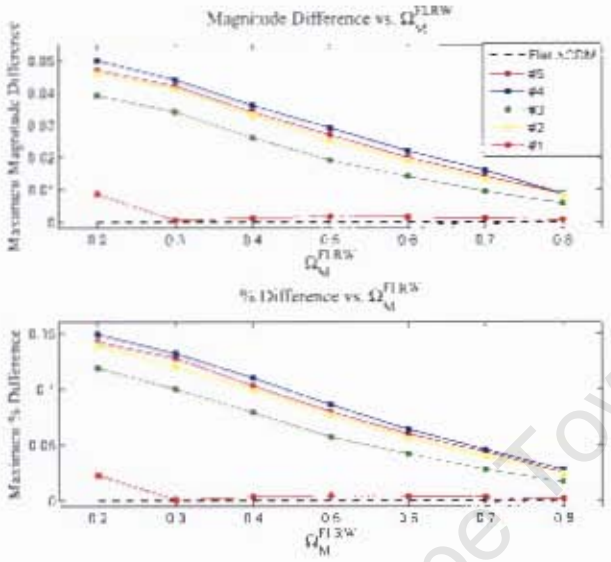

Figure 3.12: Plots of the magnitude difference $\mu^{void} - \mu^{\rm FLRW}$ (top) and percentage difference $(\mu^{void} - \mu^{\rm FLRW}) \times 100/\mu^{\rm FLRW}$ for LTB void models which have been fit to FLRW models with different matter energy densities Ω_{in}. Parameterization # 1 clearly fits the FLRW $\mu(z)$ curve far better than the other parameterizations, so much so that it would be virtually impossible to distinguish between such an LTB model and that of FLRW using SN data alone.

Table 3.1: Best-fit model parameters for our 5 different void models after fitting to $\mu^{\Lambda CDM}$ with $\Omega_{out} = 1$.

Model	H_0	Ω_{in}	σ	$\mu - \mu^{\Lambda CDM}$	$\frac{\mu-\mu^{\Lambda CDM}}{\mu^{\Lambda CDM}}$	FWHM
#	km/s/Mpc		Gpc	mag	%	Gpc
1	65.02	0.09	10.23	0.0004	0.0011	11.23
2	63.61	0.12	4.97	0.0410	0.1200	8.28
3	63.82	0.12	4.11	0.0340	0.1000	8.84
4	63.50	0.12	2.14	0.0440	0.1320	9.17
5	63.56	0.12	2.94	0.0420	0.1280	8.28

Fig. 3.13 shows plots of the resulting radial profiles of the fit to $\Omega_{M0} = 0.3$ ΛCDM (i.e. the concordance value) void models (two upper panels), the corresponding magnitude and percentage differences (third panel from top) as well as the effective deceleration parameter as a function of redshift (bottom panel). As we show later in Fig. 4.1, the maximum comoving distance reached by the SN do not exceed $r \simeq 5$ Gpc, and so beyond that distance, the shape of the void can do anything it likes. In any case, we see that, the shapes of the voids models $2 - 5$ are virtually the same up to $r \sim 2$ Gpc, such that their distance modulus curves lie close to one another. However, due to the sharpness of void #1 at the center (i.e. large ν), the degeneracies in the parameters, as we shall reveal in Chapter 4, causes such a void to be emptier at the center (i.e. lower $\Omega_{\rm in}$), as well as larger in size (i.e. larger σ). This can be understood as follows: since the sharpness at the origin is needed to give a better fit to $\mu^{\Lambda\rm CDM}$ than that of a smoother void, in order to mimick a smoother void which increases the effective size of a void, a larger and emptier void is required to give the same $\mu(z)$, or in this case, a $\mu(z)$ that fits $\mu^{\Lambda\rm CDM}$ orders of magnitude better. In Table 3.1 we show the parameters of our void models that result when fitting to $\mu^{\Lambda\rm CDM}$.

Although the distance modulus for void #1 reproduces that of ΛCDM almost exactly, the resulting effective deceleration parameter is noticably different, which suggests that the resulting Hubble rates are not that similar either. We return to the latter when fitting our voids to the data.

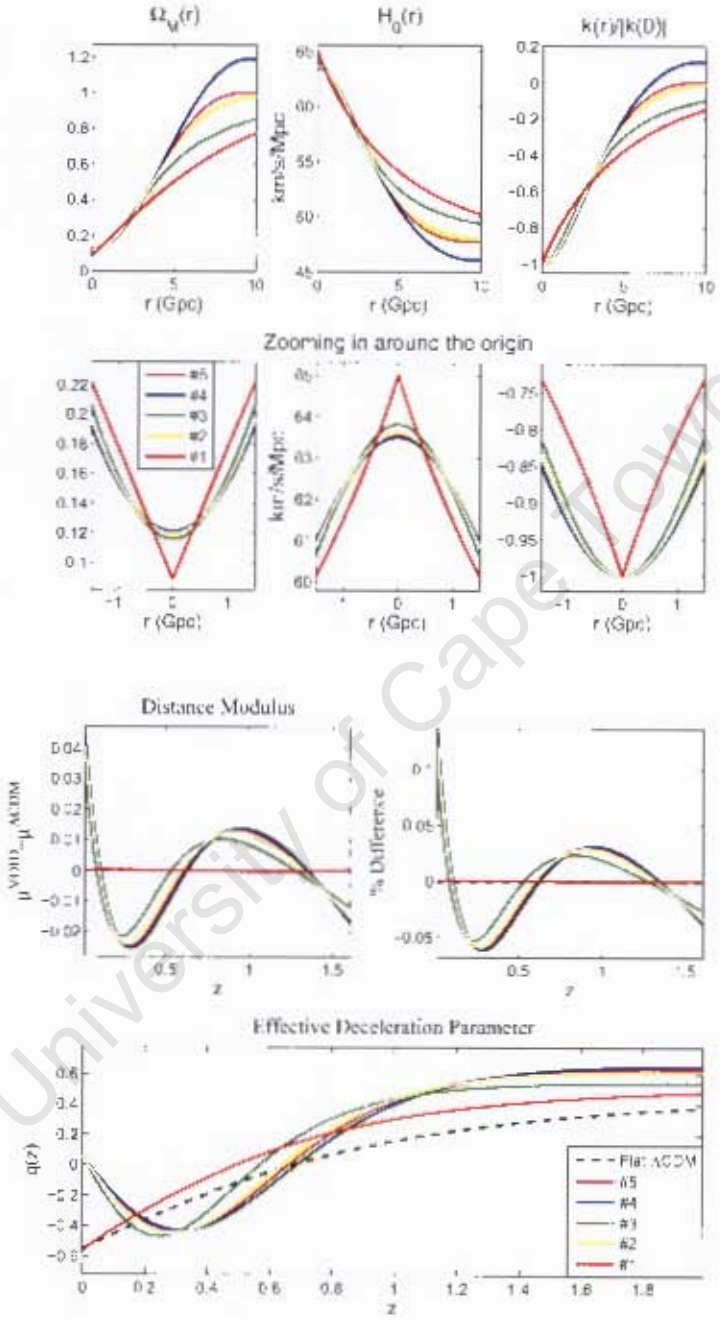

Figure 3.13: Present day radial profiles (top two rows) and corresponding difference in distance moduli for each void and that of ΛCDM (third row), as well as the resulting effective deceleration parameter as a function of redshift (bottom), after fitting each void to ΛCDM with $\Omega_{out} = 1$.

3.4.2 Leaving $\Omega_{\rm out}$ free

In Fig. 3.14 we show the magnitude difference (top panel) and the corresponding percentage difference (bottom panel) between μ^{void} and $\mu^{\Lambda\rm CDM}$ as a function of Ω_{M0} where we allowed $\Omega_{\rm out}$ to vary. As expected, when we free up $\Omega_{\rm out}$, we obtain better fits to $\mu^{\Lambda\rm CDM}$, and thus makes it that much harder to distinguish between LTB void models and ΛCDM using SN data alone.

Fig. 3.15 shows plots of the resulting radial profiles of the fit to $\Omega_{M0} = 0.3$ ΛCDM (i.e. the concordance value) void models (two upper panels), the corresponding magnitude and percentage differences (third panel from top) as well as the effective deceleration parameter as a function of redshift (bottom panel). Here we see an interesting result: that, although $\Omega_{\rm out}$ is allowed to vary, void model #1 picks out $\Omega_{\rm out} \sim 1$, whereas all of the other void parameterizations have a mean $\Omega_{\rm out} \sim 0.35$. Also notice that the outer parts of void models #4 and #5 showing the small-scale structure is visible, which is due to the fact that the voids are effectively smaller (i.e. lower σ), although, this is a result of a lower $\Omega_{\rm out}$ and density contrast: in order to reproduce the same $\mu(z)$ curve, an observer placed in a void with less matter contrast around it would have an effectively lower contrast in the expansion rate than otherwise, and would therefore see brighter SN luminosities, so $\mu(z)$ would shift down at higher z, thus decreasing the size of the void (or essentially this effect) would be necessary. In addtion, the fact that there are small-scale inhomogeneties present also allows the void to be smaller than if there was no small-scale structures present, and agrees with studies by [115].

Again we see that even though the distance modulus for void #1 reproduces that of ΛCDM almost exactly, the resulting effective deceleration parameters do not match up, implying differences in their respective Hubble rates. In addition, we notice that even low amplitude small-scale inhomogeneities in $\Omega_{M0}(r)$ (at large r) can affect the behaviour of $q(z)$ (at high z) significantly, and future observations of $q(z)$ shall either support such behaviour, or rule it out.

Finally, we note that one could invent a model an arbitrary number of parameters capable of matching $\mu^{\Lambda\rm CDM}$ to arbitrary precision, however, that approach is not practical. A more practical approach is that of the 'inverse problem', as tackled in [115], which essentially involves specifying the desired result (i.e. setting $\mu^{\rm void} = \mu^{\Lambda\rm CDM}$), and then working backwards to find the required input functions (i.e. $\Omega_{M0}(r)$). In any event, void model #1 allows for such a practical feat using the simpler 'forward problem' approach (first pointed out by [113].

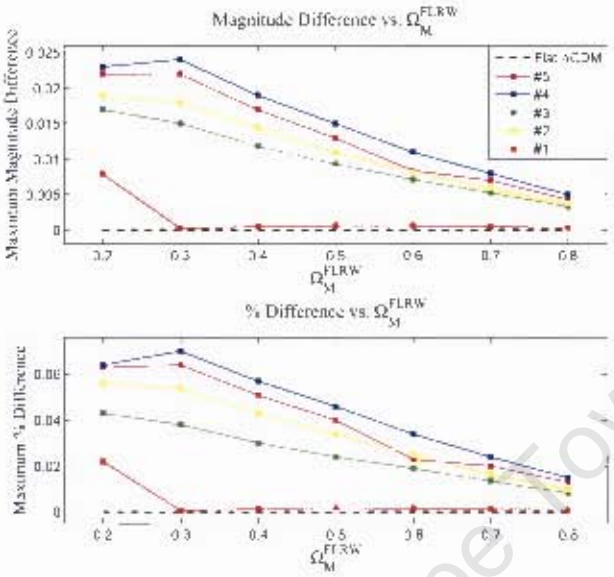

Figure 3.14: Plots of the magnitude difference $\mu^{void} - \mu^{\rm FLRW}$ (top) and percentage difference $(\mu^{void} - \mu^{\rm FLRW}) \times 100/\mu^{\rm FLRW}$ for LTB void models which have been fit to FLRW models with different matter energy densities Ω_{M0}. Parameterization # 1 clearly fits the FLRW $\mu(z)$ curve far better than the other parameterizations, so much so that it would be virtually impossible to distinguish between such an LTB model and that of FLRW using SN data alone.

Table 3.2: Best-fit model parameters for our 5 different void models after fitting to $\mu^{\Lambda\rm CDM}$ with $\Omega_{\rm out}$ free.

Model	H_0	$\Omega_{\rm in}$	σ	$\Omega_{\rm out}$	$\mu - \mu^{\Lambda\rm CDM}$	$\frac{\mu-\mu^{\Lambda\rm CDM}}{\mu^{\Lambda\rm CDM}}$	FWHM
#	km/s/Mpc		Gpc		mag	%	Gpc
1	65.01	0.09	11.62	1.12	0.0002	0.0005	12.77
2	64.27	0.10	1.95	0.37	0.0180	0.0540	3.21
3	64.43	0.10	1.97	0.45	0.0150	0.0380	3.91
4	64.12	0.11	0.78	0.32	0.0240	0.0700	3.34
5	64.18	0.11	1.17	0.36	0.0220	0.0640	3.24

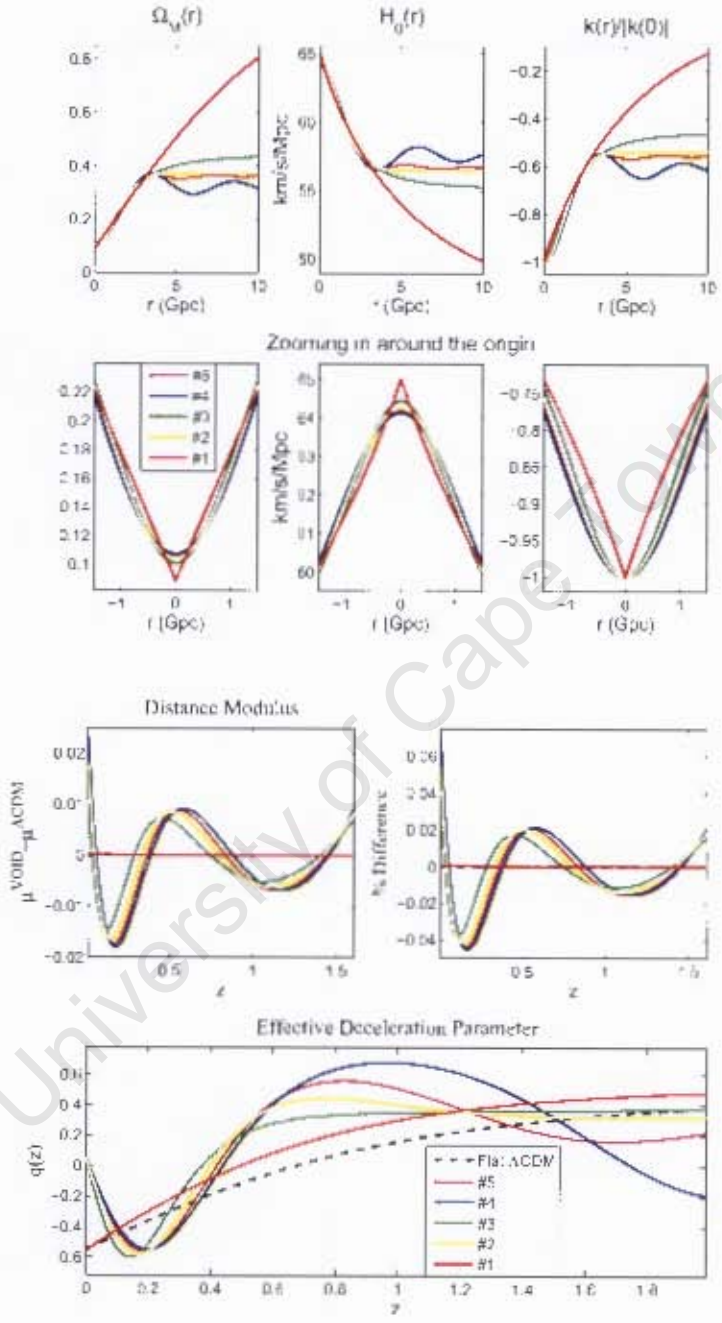

Figure 3.15: Present day radial profiles (top two rows) and corresponding difference in distance moduli for each void and that of ΛCDM (third row), as well as the resulting effective deceleration parameter as a function of redshift (bottom), after fitting each void to ΛCDM with Ω_{mat} free.

Chapter 4

Fitting Voids to Data

We dedicate this section to fitting our 5 different void models to the SN and $H(z)$ data, in order to determine whether either of these void models are preferred over ΛCDM or not. We also perform a likelihood analysis specifically on void model #1, in order to: provide confidence limits on each parameter, which we then use to determine the range of ν values that give an equally well fit to the data, allowing us to discuss the issue of the smoothness at the center [109,110,111]; understand the degeneries between any two parameters.

4.1 Overview of the Method and Codes Used

We made use of the publically available easyLTB Fortran90 code provided by [120] to run through more than a million different parameter values, simultaneously computing $\mu(z)$, $H(z)$ and the χ^2 statistic for each model with the intent of finding the best-fit parameters for the voids considered. We found the best-fit parameters by manually narrowing and refining the range and grid-spacing (i.e. priors) of each parameter, in order to search for the smallest χ^2 – indeed, this is not a very efficient method, however, after numerous checks, the results that we shall finally quote corresponds to the global minimum (as opposed to the local minimum) to well within a percent.

The code is setup to compute χ^2 for the SN (χ^2_{SNE}), BAO (χ^2_{BAO}) and CMB data (χ^2_{CMB}), but we have left the testing of the LTB models against the last two for future work due to the fact that these quantities are affected by the growth of structure in the universe, thereby requiring the use of linear perturbation theory – only once we have calculated the full CMB power spectrum as predicted by LTB

models can we really trust those results. On the other hand, we have added the Hubble rate data (from here on referred to as H) given by [23] into our analysis, and we have used the longitudinal Hubble rate $H_{\parallel}$ as our model prediction, since [23] determined $H(z)$ via dt/dz measurements, which in the LTB case (see Eq. (2.83)) is related to $H_{\parallel}$. The main reason for adding the $H(z)$ data into our analysis is, not only because it does not require the use of LTP, but because, as we revealed in the previous chapter, all of our void parameterizations can fit $\mu^{\Lambda\text{CDM}}$ (although we know this already from [116]), making it impossible for us to distinguish between two such models, yet alone test the CP [113], using SN alone, so using $H(z)$ in addition to the SN data allows us the opportunity to find detectable differences between ΛCDM and LTB void models (if any). Now, even though the $H(z)$ data contains only 10 points, after adding in the HST key project value of $H_0 = 72 \pm 8$ km/s/Mpc [56]), it will still offer an improvement to the constraints provided by the largest sample of SN to date, the Constitution set [19] consisting of 397 SN.

The easyLTB code is not set up to compute models in which $\Omega_{M0}(r) > 1$ – only for values equal to or less than unity. Although for our main investigation we have, when fitting to the data, fixed Ω_{out} to 1 anyway (thus $\Omega_{M0}(r) \leq$ for all the profiles we considered, except # 4 and # 5), we modified the code to allow $\Omega_{M0}(r)$ to take on any value, and shall include the main results for that case, however, focus more on the case Ω_{out} fixed to 1, in the next chapter.

In a nutshell, the easyTLB code works, for the case of a homogeneous big bang, as follows:

- choose the function $\Omega_{M0}(r)$ with however many parameters describing it.
- insert the latter as well as its (analytic) derivative in the 'model.f90' file in the '\Experiments\constrained' directory.
- in the same directory, choose the parameter ranges (priors) in the 'input.txt' file as well as the courseness of the grid (i.e. the number of points n).
- after compiling and running the code, a file is saved in the '\data' folder entitled 'constrained.dat' (which can, too, be modified by the user) that contains columns of the parameter values scanned verses the corresponding χ^2 values.
- finally, perform a likelihood analysis, either using the IDL routines provided with the code or by some other method, to determined the constraints on the parameters of the model.

Of course, one can modify the code in any desired way, as we have done to cater for $\Omega_{M0}(r) > 1$. In order to convince ourselves that every quantity in the easyLTB code was computed properly, and to ensure that the best-fit values came out correctly, we compared the necessary outputs from the latter with that calculated in an existing Maple code written by us before-hand, which was also checked on numerous occasions by comparing with results from other studies – in particular, we ran the same parameterization for the homogeneous bang time model investigated by [138], and was able to reproduce their Fig. 4. In addition, when setting a $\Omega_M(r) = 1$ throughout, the resulting distance modulus matched that of the EdS model, and thus gave us further confidence in our code.

4.1.1 Statistical Analysis and Likelihoods

Regarding the fitting of our void models to data, we computed the χ^2 statistic in the usual way [123]

$$\chi^2(p) = \sum_{i=1}^{N} \frac{(D(p, z_i) - M(p, z_i))^2}{\sigma^2_{D_i}}\,, \tag{4.1}$$

where p refers to the model parameters, M to the value of the predicted observable, D to the value of the measured observable with corresponding error σ_D and N is the total number of data points. The best-fit parameters are those that minimize χ^2. When comparing two different models, it is customary to compute the reduced χ^2 instead, obtained by dividing the χ^2-statistic by the number of degrees of freedom (ndf),

$$\text{ndf} = \text{number of data points} - \text{number of parameters} + 1\,, \tag{4.2}$$

where the preferred model is the one with the lower $\frac{\chi^2}{\text{ndf}}$.

The easyLTB code outputs a file with seven columns (after removing χ^2_{BAO} and χ^2_{CMB} and adding in χ^2_H): the five parameters H_0, Ω_{in}, σ, $\log_{10}\nu$ and Ω_{out} in that order, then χ^2_{SNE} and finally χ^2_H, respectively. Notice that we wrote down $\log_{10}\nu$ instead of just ν. We did this because, due to the nature of how ν affects the shape of $\Omega_{M0}(r)$, once it exceeds a value $O(10^3)$, $\Omega_{M0}(r)$ (and therefore $\mu(z)$) does not change significally (if at all), thus using such a log scale not only allows us to specify the range of ν more easily as we can cover a large range in ν by only focussing on a relatively small range in $\log_{10}\nu$, but allows us to include all of its important behavioural properties in our analysis (i.e. where it causes a flat, steep or a void with intermediate gradient at the origin).

The next task we undertook was to calculate the joint- and one-parameter likelihood distributions in order to understand the degeneracy that exists between pairs of parameters i.e. how shifting the value of one parameter necessitates a shift in the other in order to maintain the same χ^2, and to provide confidence limits on each parameter i.e. to be able to say how confidence we are that the best-fit value is within the given upper and lower bounds of the marginalized (to be defined in a moment) best-fit value. The likelihood is defined as

$$L(p) = L_{max} \exp\left[-\frac{\left(\chi^2(p) - \chi^2_{min}(p)\right)}{2}\right], \tag{4.3}$$

where χ^2_{min} is the minimum χ^2, and L_{max} is the maximum likelihood (which corresponds to the best-fit model). Although IDL routines for doing the likelihood analysis is provided, we wrote our own procedure in Maple in order to compute joint-parameter likelihood contours and one-parameter likelihood curves using SN data alone, as well as combining SN and $H(z)$ data (from here on referred to as SN+H). To work out the likelihood, specifically in the combined case (as in the SN case alone, things are slightly simpler), we added the columns of the corresponding χ^2's (equivalent to multiplying the respective likelihoods), before applying equation (4.3).

Now, in order to construct the 2-D (i.e. joint-parameter) likelihood contours and the 1D (i.e. one-parameter) likelihood curves, we needed to perform marginalization. The general formula for marginalization of a quantity is given by

$$\tilde{L}(p_1, ..p_j) = \int dp_{j+1}..dp_m \, L(p)\,, \tag{4.4}$$

if there are in total m parameters and we are interested in j of them ($j < m$). However, since we were only working with discrete values of L (recall that the Fortran code scans through a grid of parameter values), we needed to approximate the integral in (4.4). We used the simple Riemann sum approximation

$$\tilde{L}(p_1, ..p_j) = \sum_{i=1}^{n_{p_{j+1}}} ... \sum_{i=1}^{n_{p_m}} L(p_1, ..p_j; p_{j+1,i}..p_{m,i}) \Delta p_{j+1} ... \Delta p_m\,, \tag{4.5}$$

where

$$\Delta p = \frac{\max(p) - \min(p)}{n_p - 1}\,, \tag{4.6}$$

and n_p refers to the number of points the parameter p is chosen to have in its range $[\min(p), \max(p)]$, such that the sum is essentially over all the models in which

the parameters $p_1..p_j$ stay the same. Indeed, there exists other numerical methods that are capable of providing better approximations to Eq. (4.4), however, we compared our results with that from the IDL routines provided, and found significant agreement between the two.

Joint-parameter (or 2-D) likelihood contours were then constructed as follows:

- using the 3-dimensional surface respresenting $\tilde{L}(p_1, p_2)$, we divided it by its maximum height ($\tilde{L}_{max}(p_1, p_2)$) so that its magnitude varies from 0 to 1.
- we then could work out, using the form of Eq. (4.3) divided through by L_{max}, and the values in Table I in [123], the different heights in $\tilde{L}/\tilde{L}_{max}$ that corresponds to the different confidence levels within which the best-fit marginalized value, which corresponds to the peak of the distribution, falls. The different heights are given by

$$\frac{\tilde{L}}{\tilde{L}_{max}} = \exp\left[-\frac{\Delta\chi^2}{2}\right], \tag{4.7}$$

where $\Delta\chi^2 = \chi^2 - \chi^2_{min} = 2.30$, 6.17 and 11.80 for the 68.3%, 95.4% and 99.7% confidence levels, respectively.

The respective 2-D confidence contours shown in section 4.3.2 are effectively the slices of the corresponding likelihood surface corresponding to those numbers. One-parameter (or 1-D) likelihood distributions for a particular parameter is determined by marginalizing over all of the other parameters, leaving a 1-dimensional function $\tilde{L}(p_1)$ to work with. From our results (as we shall come to in section 4.3) it was clear that our parameters were not entirely governed by Gaussian statistic, due to the skewness of their likelihood distributions. Therefore, in order to provide a more accurate result, at least in this case (i.e. the 1-D case), we rather integrated under the curve, from the left and right, to find the lower and upper bounds, respectively, on each parameter, such that the area to the left of the lower bound, and to the right of the upper bound, each makes up x% of the total area under the curve, where x corresponds to 15.8, 0.023, 0.0015 in the 68.3%, 95.4% and 99.7% cases respectively. In the case of a Gaussian distribution, the 68.3%, 95.4% and 99.7% confidence levels are also known as the $1-\sigma$, $2-\sigma$ and $3-\sigma$ levels, respectively, where σ is the parameter used to define the width of the Gaussian which is directly proportional to the width of the confidence regions.

4.2 Results and Analysis

4.2.1 Fitting to Cosmological Data

Now that we have an idea of how well these voids can reproduce $\mu^{\Lambda\mathrm{CDM}}$, let us see how well they can fit the SN and SN+H data. Table 4.2 shows best-fit models to SN only, along with the corresponding χ^2, χ^2/ndf and r_{FWHM}. Here we have fixed $\Omega_{\mathrm{out}} = 1$ in all of the models considered. The main reason for doing this is for simplicity – the number of parameters describing our model is kept to a minimum – but we are also aware that the value of Ω_M tends to 1 anyway as one goes back into the past (or similarly large distances or redshifts)[1]. One should keep in mind here, however, that by setting $\Omega_{\mathrm{out}} = 1$ we may be restricting the freedom of our models, since, as tables 3.1 and 3.2 suggest, this may influence the resulting void FWHM required to fit the observations. On the other hand, as Fig. 4.1 shows, the current data fails to probe the outer regions of the void, where $\Omega_{\mathrm{out}} = 1$, so based on that alone we can infer that allowing Ω_{out} to vary should not make much of a difference to the best-fit χ^2 value. In appendix A we explore the case of allowing Ω_{out} to vary, and show that, indeed, Ω_{out} is not well constrained by the data, implying that we need observations at higher redshifts to have any chance of constraining Ω_{out}.

In Table 4.1, we show the best-fit parameters of a flat ΛCDM model after fitting to SN and SN+H data. Notice that we obtain a reduced minimum χ^2 that is less than unity (the reduced χ^2 for the best-fit model should be $\gtrsim 1$), due to the fact that we increased the errors on the SN data (as mentioned in the Introduction), which has the effect of decreasing the overall χ^2 and thus $\frac{\chi^2}{\mathrm{ndf}}$ as well.

In Tables 4.2 and 4.3 we show the best-fit parameters for our 5 different void models after fitting to SN and SN+H data, respectively, along with the corresponding χ^2 and $\frac{\chi^2}{\mathrm{ndf}}$ values. The basic conclusion from these tables (4.1,4.2,4.3) is that: all of the $\frac{\chi^2}{\mathrm{ndf}}$ values are comparable, so that the best-fit void and ΛCDM models are statistically the same (to one decimal place or so), and later we shall compute other statistical quantities that basically leads to the same conclusion; the best-fit ν value for void #1 is small and finite in the fit to SN case, corresponding to an $\Omega_{M0}(r)$ profile that is smooth at the center, and slightly larger yet still finite in the fit to SN+H case, indicating that void models with $\Omega_{M0}(r)$ smooth at the center are (only slightly) favoured over sharper void profiles (as we shall later see). Of course,

[1] This can be shown by taking the limit, in both Eq.'s (2.19) (after setting $\Omega_K = 0$) and (2.67), as the scale factor tends to zero.

taking into account the second and third decimal places, we see different $\frac{\chi^2}{\text{ndf}}$ values, and in particular, the lowest and hence the most preferred model is void model #4 in the fit to SN case, and #3 in the SN+H case.

Table 4.1: Best-fit parameters for the flat ΛCDM model from SN and SN+H constraints.

Data	H_0 km/s/Mpc	Ω_M	χ^2	$\frac{\chi^2}{\text{ndf}}$
SN	64.93	0.29	311.18	0.786
SN+H	64.55	0.32	326.51	0.804

Table 4.2: Best-fit model parameters from SN data.

Model #	H_0 km/s/Mpc	Ω_{in}	σ Gpc	$\log_{10}\nu$ $\times 10^6$	χ^2_{SN}	$\frac{\chi^2_{SN}}{\text{ndf}}$	FWHM Gpc
1	64.17	0.149	2.05	4.0	308.82	0.784	5.13
	64.36	0.140	3.29	–	308.83	0.782	5.47
3	64.39	0.129	3.21	–	309.36	0.783	6.42
4	64.34	0.148	1.35	–	308.54	0.781	5.77
5	64.35	0.143	1.90	–	308.70	0.782	5.29

Table 4.3: Best-fit model parameters from SN+H data.

Model #	H_0 km/s/Mpc	Ω_{in}	σ Gpc	$\log_{10}\nu$	χ^2_{SN+H}	$\frac{\chi^2_{SN+H}}{\text{ndf}}$	FWHM Gpc
1	64.24	0.119	4.94	0.71	321.64	0.796	6.81
	64.33	0.120	3.77	–	321.74	0.794	6.28
3	64.38	0.114	3.59	–	321.57	0.794	7.17
4	64.30	0.125	1.55	–	321.81	0.795	6.65
5	64.35	0.121	2.21	–	321.86	0.795	6.14

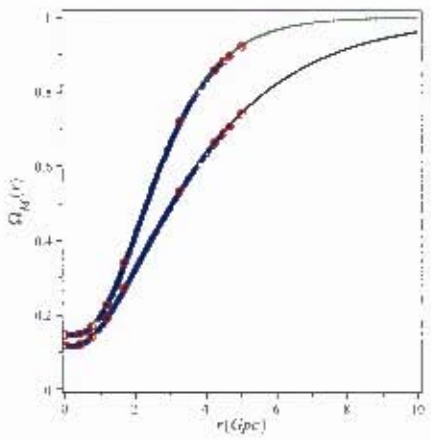

Figure 4.1: Plot showing the radial positions corresponding to the reshift of each SN (blue circles) and $H(z)$ (red circles) data point. The curves show the best-fit to SN (green) and SN+H (black) $\Omega_{\Lambda 0}(r)$ profiles for void #1. The lack of data outside the void implies that Ω_{out} is weakly constrained (see Appendix A).

Looking at the columns of FWHM in the above tables, we see that its value varies little between each void. Specifically, in the SN case we find that its average value with 68% confidence[2] is 5.6 ± 0.5 Gpc, and 6.6 ± 0.4 Gpc in the SN+H case, giving us true cosmological-sized voids in agreement with results from [120], where the corresponding FWHM is 6.5 Gpc.

In Fig. 4.1 we show the comoving radial distances corresponding to the redshifts of each SN (blue circles) and $H(z)$ data (red circles) corresponding to the best-fit to SN (green curve) and best-fit to SN+H data (black curve) $\Omega_{\Lambda 0}(r)$ profile, respectively, for void model #1. The point of this plot is to show that their is insufficient data outside of the underdense region[3], so that trying to constrain the behaviour of the $\Omega_{\Lambda 0}(r)$ profile in the outer regions of the void is futile. The data only probe comoving distances out to about 5 Gpc, and so we should not be worrying to plot the best-fit profiles (as we shall now do) beyond that distance, although we do just for illustrative purposes. In addition, allowing Ω_{out} to vary would have little or no consequence on the value of the resulting $\frac{\chi^2}{\text{dof}}$ in that case, although we briefly highlight some of the results we obtained in the latter case in Appendix A.

[2]This is just the standard deviation of the mean (average) value quoted.

[3]This is true for the best-fit models, due to their large sizes. The SN and $H(z)$ data would probe the outer parts of the $\Omega_{\Lambda 0}(r)$ profile for smaller voids, although, as we have found, it is the huge cosmic-sized voids that are preferred.

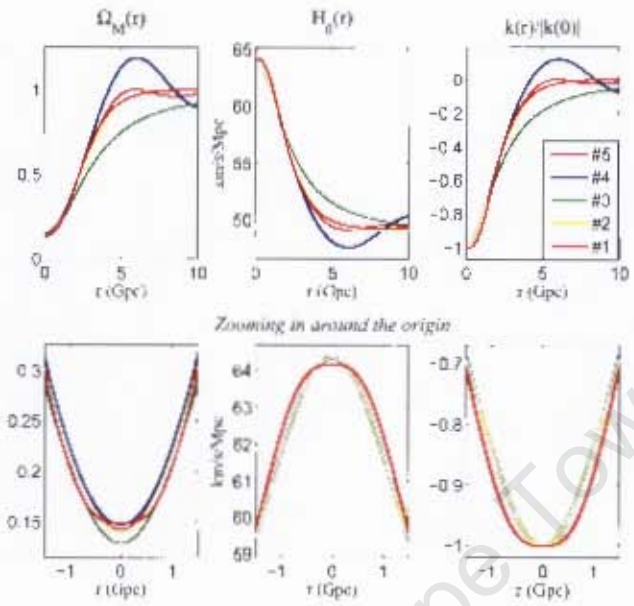

Figure 4.2: Best-fit void profiles from SN data.

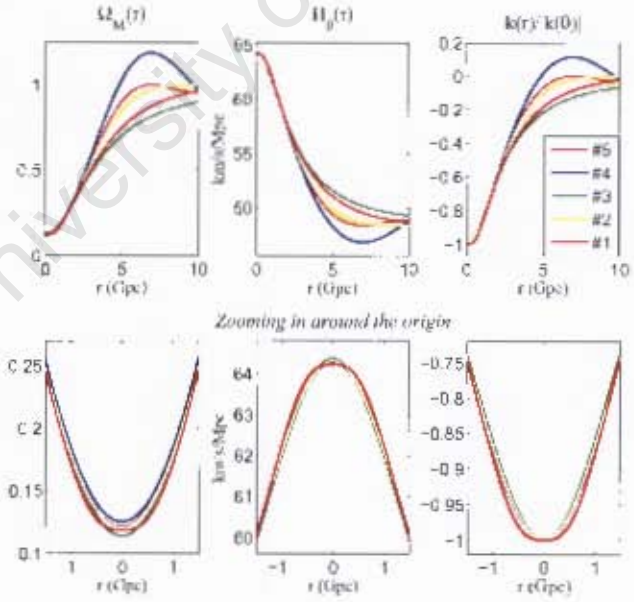

Figure 4.3: Best-fit void profiles from SN+H data.

In Fig.'s 4.2 and 4.3 we show plots of $\Omega_{M0}(r)$, $H_{\perp 0}(r)$ and $k(r)$ for our 5 different best-fit void models from SN and SN+H data, respectively. All of these void models are virtually indistinguishable up to a comoving distance of about 2 Gpc in both cases (i.e. SN and SN+H, respectively), indicating that the data constrains the behavioural features of such voids fairly tightly, but further out the voids deviate slightly from one another. Thus, having more data at higher redshifts, say from $z > 1$ till about $z = 4$, could allow the ruling out of some of these models considered, since, of course, differences in the shape of the void (i.e. $\Omega_{M0}(r)$) leads to differences in the observable quantities such as $\mu(z)$ and $H(z)$, as we shall now turn to.

Fig.'s 4.4 and 4.4 shows the corresponding distance moduli with an empty universe subtracted off for each best-fit void model as well as that of the best-fit ΛCDM and EdS models (left panel), and the difference between each void model's distance modulus and that of ΛCDM (right panel), for the fits to SN and SN+H data, respectively. In both cases, the void $\mu(z)$ curves are all virtually the same (see the left panels), but when comparing the void and ΛCDM $\mu(z)$ curves (right panels), the differences between the latter is different in the SN and SN+H cases. Although in both cases $\mu - \mu^{\Lambda\text{CDM}}$ is within the accuracy of current SN data (i.e. the two models are indistinguishable) up to $z \sim 1$, beyond that redshift we see that in the fit to SN data case, $\mu - \mu^{\Lambda\text{CDM}}$ is much larger than that in the fit to SN+H case, so that if the accuracy of data improves, we may be able to support or rule these LTB void models in favor of the ΛCDM model.

Since there is no way of distinguishing between LTB and ΛCDM in the fit to SN+H data case using SN data alone (right panel Fig. 4.5), let us see what the plots of the corresponding Hubble rate tells us. The main outcome that stems from Fig. 4.6 is that the resulting best-fit $H_{\parallel}(z)$ curves for our 5 different void models traces the shape of the $H(z)$ data remarkably well. In fact, as an example, when we compute the χ^2's for the $H(z)$ curves corresponding to the best-fit to SN+H data of void model and that of ΛCDM, we find the following: void model produces a $\chi^2 = 12.45$, and consequently $\frac{\chi^2}{\text{ndf}} = 1.56$, whereas the corresponding best-fit to SN+H data ΛCDM $H(z)$ curve has $\chi^2 = 14.20$ and a $\frac{\chi^2}{\text{ndf}} = 1.58$, so actually, the χ^2's are, just as in the fit to SN and SN+H cases, comparable, with the void model fitting slightly better. So, although by 'eye' it seems that the void models fit the data significantly better than the ΛCDM model, the number of data points are too few to do any good statistics with, and therefore, does not currently do these models justice.

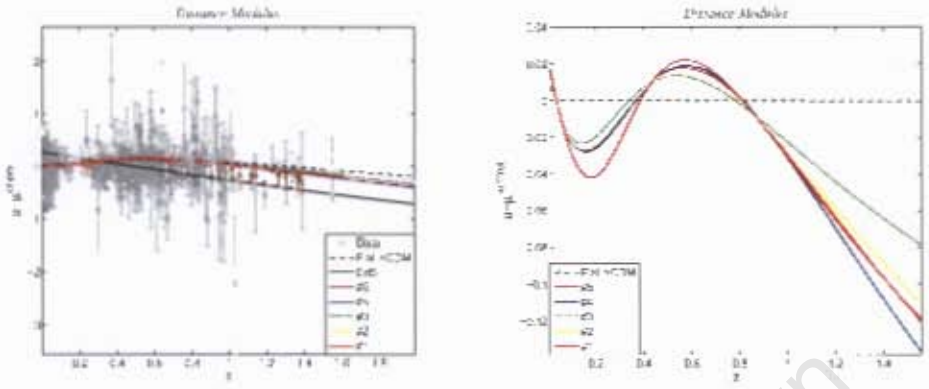

Figure 4.4: Left panel: Best-fit SN distance moduli, normalized to that of a Milne universe with H_0 given by that of the best-fit ΛCDM model, for each void along with that of the best-fit ΛCDM and EdS models, as well as the Constitution SN data points (grey circles). Right panel: Difference in distance moduli between the best-fit SN voids and that of ΛCDM. Up till a redshift $z \sim 1$, these void models are practically indistinguishable from that of ΛCDM, however beyond $z \sim 1$, such a difference could be detected given future accuracy estimates for SN data.

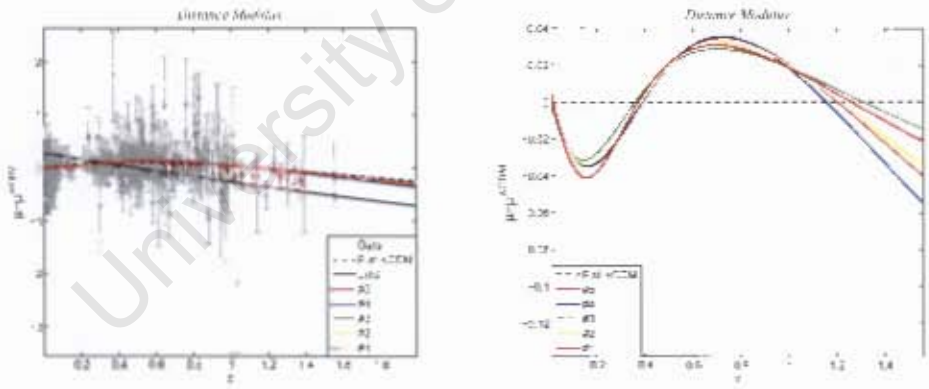

Figure 4.5: Left panel: Best-fit SN+H distance moduli, normalized to that of a Milne universe with H_0 given by that of the best-fit ΛCDM model, for each void along with that of the best-fit ΛCDM and EdS models, as well as the Constitution SN data points (grey circles). Right panel: Difference in distance moduli between the best-fit SN+H voids and that of ΛCDM. These void models are practically indistinguishable from that of ΛCDM for the entire redshift range considered.

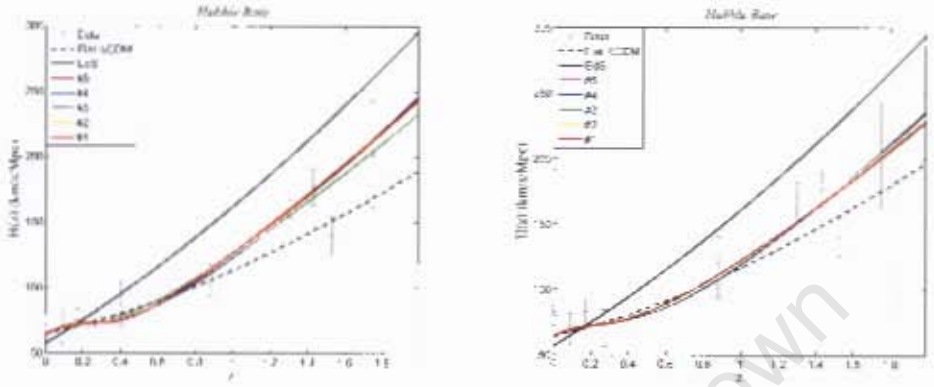

Figure 4.6: Plots of the Hubble rate for our 5 best-fit void models to SN (left) and SN+H (right) data, as well as that for ΛCDM and EdS. Notice how well the void models go through the data points.

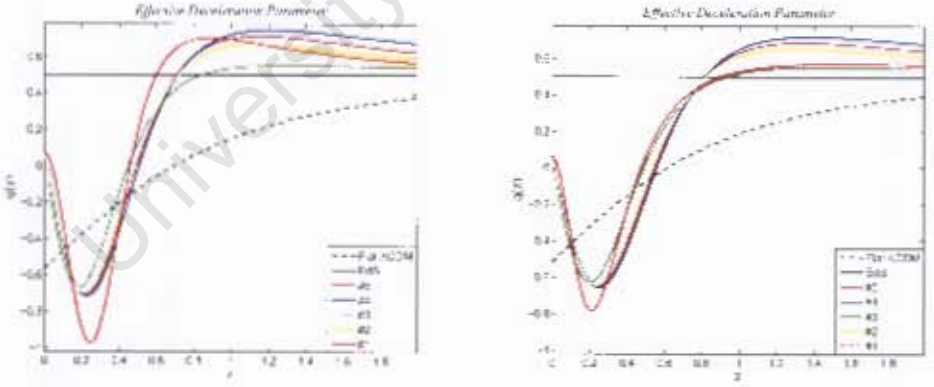

Figure 4.7: Effective deceleration parameter for the best-fit models to SN (left) and SN+H (right) for our 5 different void models, as well as that for ΛCDM and EdS. Note that for all these voids models we have an effective deceleration today.

Given the differences shown in the Hubble rate for the two models, we plot the effective deceleration parameter, $q^{\rm eff}(z)$, which depends on the gradient of the Hubble rate, in Fig. 4.7. As expected, $q(z)$ for our 5 different best-fit void models is noticably different from that of the ΛCDM model, therefore observations of $\frac{d}{dz}H(z)$, and thus $q(z)$, too, will either further support the idea that we live in a giant cosmic void, or rule the latter out in favour of ΛCDM. In any event, we do see striking resemblance between our void $q(z)$ curves and that shown in Fig. 1.6 (left panel), which suggests that our best-fit void models are effectively mimicking dynamical DE models.

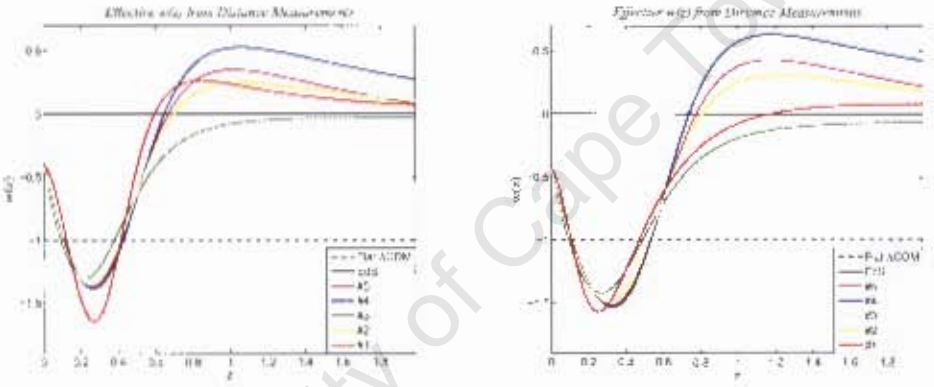

Figure 4.8: Effective equation of state parameter from distance measurements for the best-fit models to SN (left panel) and SN + H (right panel) for our 5 different void models, as well as that for ΛCDM and EdS.

We finally close this chapter off with results of our reconstructed DE equation of state for our 5 different best-fit to SN and best-fit to SN+H void models. From Fig.'s 4.8 and 4.9 we see that w_{DE}^{eff} varies over redshift, as would a dynamical DE FLRW model. In addition, all of the plots show phantom-like behaviour, i.e. where $w_{DE}^{\text{eff}} < -1$, at $z \sim 0.2$. At higher redshift, w_{DE}^{eff} tends to zero, as expected in a matter-dominated universe (i.e. EdS).

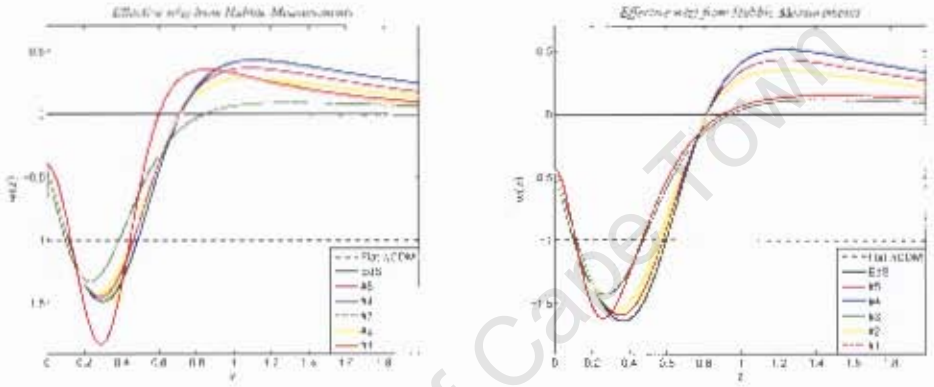

Figure 4.9: Effective equation of state parameter from Hubble measurements for the best-fit models to SN (left panel) and SN+H (right panel) for our 5 different void models, as well as that for ΛCDM and EdS.

4.2.2 Likelihood Contours

In this section, we reveal the degeneracies between all the possible pairs of parameters by constructing joint-parameter likelihood contours, and also determine the likelihood distributions of each parameter from SN and SN+H constraints for void model #1.

Table 4.4: Marginalized best-fit parameters at 95% confidence from SN and SN+H constraints

Data	H_0	$\Omega_{\rm in}$	σ	$\log_{10}\nu$
	km/s/Mpc		Gpc	
Priors	58.00–74.00	0.00–0.24	0.00–24.00	-1.30–3.70
SN	$64.61^{+1.69}_{-1.39}$	$0.10^{+0.09}_{-0.07}$	$6.72^{+17.68}_{-5.17}$	$3.3^{-\infty}_{-3.97}$
SN+H	$64.72^{+1.58}_{-1.49}$	$0.10^{+0.07}_{-0.05}$	$7.84^{+12.51}_{-6.27}$	$3.5^{-\infty}_{-3.81}$

Table 4.4 shows the marginalized best-fit parameters for void model #1 with 95% confidence limits, from fitting to SN and SN+H data, where the priors are also given. We see again that the main difference between the parameter values in the SN and SN+H cases is the value of σ: the SN+H case yields a higher value for σ, which arises from the fact that (not shown here), when fitting void models to $H(z)$ data only, extremely large ($\sigma \sim 20$) Gpc and empty ($\Omega_{\rm in} \sim 0.01$) voids are the ones that give the minimum χ^2, so when combining with the fit to SN results which has a lower value for σ, it is only natural that σ is then larger in the fit to SN+H case than in the fit to SN case only. Notice in the column for the smoothness parameter ν (or $\log_{10}\nu$ as shown), that the best-fit values are roughly 3 orders of magnitude larger than that in the unmarginalized case (see Tables 4.2 and 4.3), indicative of sharp, spikier voids, yet still differentiable and continuous at the center. Also note that there is no upper bound on ν, only a lower one, but we shall come to this again just now. As will also be clear just now, is the fact that, when combining data, the constraints on each parameter tightens – a common result in the literature.

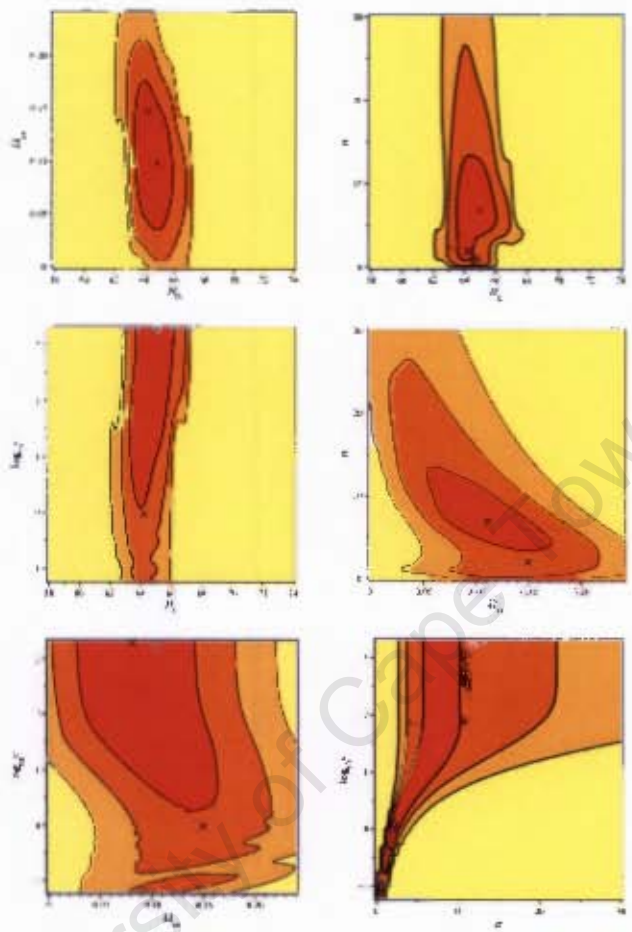

Figure 4.10: Joint-parameter likelihood contours from SN constraints. Black crosses indicates the marginalized best-fit values and blue crosses show the best-fit to SN values.

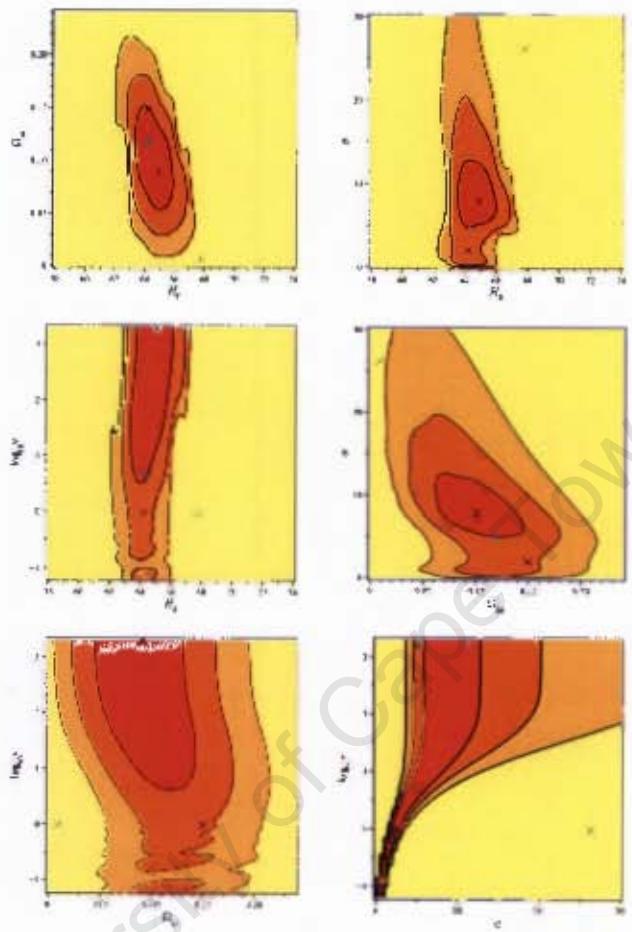

Figure 4.11: Joint-parameter likelihood contours from SN+H constraints. Black crosses indicates the marginalized best-fit values, blue crosses show the best-fit to SN values, green crosses are the best-fit to $H(z)$ values, and cyan crosses shows the best-fit to SN+H values.

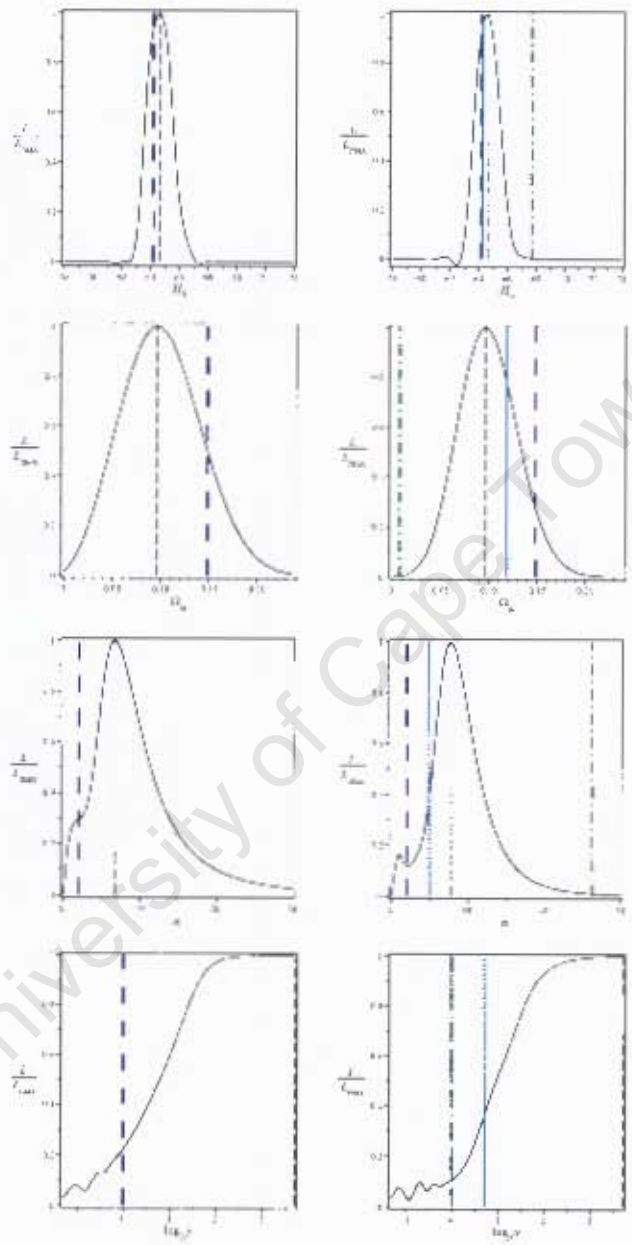

Figure 4.12: 1D likelihood distributions for each parameter from SN (left) and SN+H (right) constraints. Black dashed lines corresponds to marginalized best-fit values, while the blue, green and cyan lines correspond to the best-fit to SN, $H(z)$ and SN+H values, respectively.

In Fig.'s 4.10 and 4.11 we show the joint-parameter likelihood plots from SN and SN+H constraints, respectively. The inner, red-filled regions represent the 68.3% confidence level, the orange regions 95.4%, and the off-yellow regions correspond to the 99.7% level, and the remaining regions includes everything > 99%. Just to recall, the way to view these plots are as horizontal slices at different heights[4] through the 3-dimensional surface that represents the marginalized likelihood functional of the given two parameters. The crosses indicate the positions of: the best-fit to SN data (blue), the best-fit to $H(z)$ data (green), the best-fit to SN+H data (cyan), and the best-fit mariginalized (black), parameters.

Let us quickly discuss the degeneracies that exist between the parameters. The strongest degeneracies are between all the possible pairs of $\Omega_{\rm in}$, σ and ν, and can be interpreted as follows: in order to give the same (or very similar) χ^2, if one wants a larger void (i.e. larger σ), then $\Omega_{\rm in}$ must decrease (i.e. the void must be emptier), and the void must be sharper at the origin (i.e. larger ν), and vice versa. The degeneracies between those same parameters and H_0 are less obvious, but still present: Emptier (i.e. lower $\Omega_{\rm in}$) and sharper (i.e. larger ν) voids require a larger H_0, whereas a larger void (i.e. larger σ) needs a lower H_0 in order to give the same (or very similar) χ^2, and vice versa. As mentioned in the beginning of this section, when we combine constraints from SN with constraints from $H(z)$ data, the resulting constraints on the parameters tighten, and we can see this occuring in Fig.'s 4.10 and 4.11.

In Fig. 4.12 we show the one-parameter likelihood distributions for each parameter from SN (left) and SN+H (right) constraints – this is a graphical version of Table 4.4. The vertical lines corresponds to: the best-fit to SN (blue, space-dashed), best-fit to $H(z)$ (green, dot-dashed), best-fit to SN+H (cyan, solid) and marginalized best-fit (black, dashed), parameters. Notice that H_0 and $\Omega_{\rm in}$ are fairly well constrained, whereas σ, and even more so, ν, is poorly constrained. Although σ has both a (well-defined) lower and an (not so well-defined) upper bound, ν only has a (not very well-defined) lower bound, no upper bound. This made is difficult to determine the constraints on ν, as the likelihood distribution does not have a definite peak, and does not drop off at large ν. This, and the observation that in the 2-D plots of σ vs. $\log_{10}\nu$ that the best-fit model to SN (blue cross), and the best-fit model to SN+H (cyan cross), each coincides with their corresponding marginalized

[4]As stated earlier in section 4.1.1, these heights correspond to $\exp(-\Delta\chi^2/2)$, where $\Delta\chi^2 = 2.30, 6.17$ and 11.80 corresponding to 68.3%, 95.4% and 99.7% levels, respectively.

best-fits (black cross), whereas in the other 2-D plots no such thing happens, can be understood as follows: first of all, the reason why ν is does not have an upper bound arises from the fact that, once ν reaches a certain large value ($\sim 10^3$), increasing it further does not change the resulting $\Omega_{M0}(r)$ profile, and so we expect that an upper bound on ν would not come easily since the liklihood distribution would not change after that critical value of ν; second of all, since H_0 and $\Omega_{\rm in}$ are well constrained, marginalizing over them to produce the 2-D σ vs. $\log_{10}\nu$ contour plot should preserve (and does) the best-fit to data models and that of the marginalized best-fits, hence the intersection of the crosses. The moment we marginalize over either one of σ or ν, the degeneracy existing between the latter, and the fact that ν has no upper bound, causes a difference between the best-fit to data models and that of the marginalized best-fits.

Finally, we end off with one final point that, although was initially perceived as problematic, ended up just being a minor issue that was eventually overcome by the numerous checks carried out. The basic issue that we came across when fitting to SN data was the fact that the best-fit ν was extremely close to 1 – the value at which parameterization # 1 has a 'hole' – which we thought to be a very unlikely situation. As such we checked the Fortran code for possible subtleties that we may have overlooked. We ruled out the possibly that the precision of the code was not high enough, which would lead to numerical rounding errors. We compared the output of $\Omega_{M0}(r)$ from the Fortran code with that from Maple, as well as the value of the corresponding χ^2 for a given model when $\nu = 1$, and found exact agreement. We then checked whether different datasets also prefer a value $\nu \sim 1$ in order to finally put the issue of $\nu = 1$ to rest. As Table B.1 shows in Appendix B, other SN datasets produce a different value for the smoothness parameter ν, thus supporting the finding from our other checks that our code was working correctly, and that the new Constitution dataset preferred a value of ν close to the where $\Omega_{M0}(r)$ cannot be evaluated.

4.2.3 Which model is favoured the most?

In this section, we determine which model, out of all considered, is favoured the most by the observations. If we compare the reduced χ^2's for the best-fit void models $(1-5)$ with that from the best-fit ΛCDM model, we see that $\frac{\chi^2}{\text{ndf}}$ for the void models are roughly a quarter percent smaller (at worst) than that of the ΛCDM model in the fit to SN case, and roughly one percent smaller (at worst) in the SN+H case. This immediately implies that the void models considered here are, very slightly, favoured over ΛCDM. However, there are more sophisticated techniques applicable to model selection, such as the Akaike information criterion (AIC) [135]

$$\text{AIC} = \chi^2_{\text{min}} + 2k + \frac{2k(k-1)}{N-k-1}\,, \tag{4.8}$$

where k is the number of parameters and N the number of data points, and the Bayesian information criterion (BIC) [136]

$$\text{BIC} = \chi^2_{\text{min}} + k \ln N\,. \tag{4.9}$$

A lower AIC or BIC implies a more favoured model. In Table 4.5 we summarize the AIC and BIC values for each void model as well as that of ΛCDM.

Table 4.5: Information criterion for the best-fit void models and that of ΛCDM model from SN+H constraints

Model	AIC	BIC
1	329.70	332.08
2	327.78	329.58
3	327.60	329.40
4	327.84	329.64
5	327.89	329.69
ΛCDM	330.52	331.73

From the AIC, we see that void model # 1 is only slightly favoured over the ΛCDM model. From the BIC, we see obtain the opposite result: the ΛCDM model is slightly favoured over void model # 1. In any case, the most favoured void is given by void model [illegible], although, it is not possible to say with any confidence which model is favoured the most: a large void embedded in an otherwise EdS universe, or a flat dark energy dominated FLRW model. To accomplish such a feat, we would require data with much better accuracy, and possibly to use additional observations not considered here.

4.2.4 Non-Concordance Diagnostics

In this section, we provide plots of the reconstructed densities given by Eq.'s (2.92) and (2.93), as well as the numerator of the derivatives thereof, Eq.'s (2.94) and (2.95), respectively.

To begin, we reveal an interesting result obtained by [71] for the reconstructed matter density in Fig. 4.13, since, as Fig. 4.14 shows, our best-fit to SN models are remarkably similar to their best-fit to SN+BAO model, which uses the CPL parameterization for the dark energy.

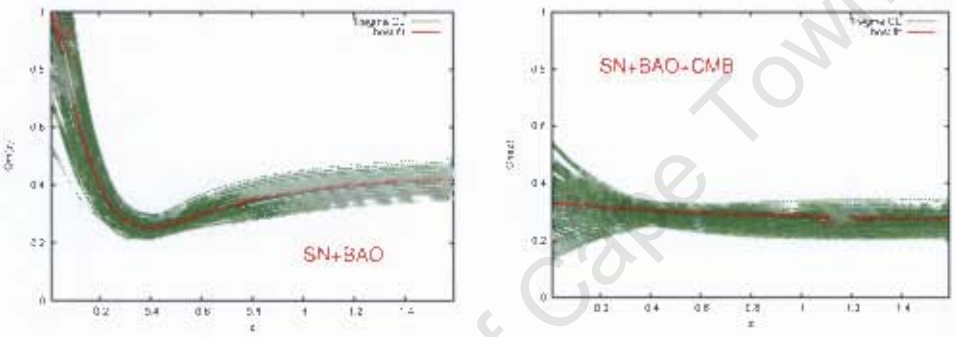

Figure 4.13: Reconstructed $\Omega_M(z)$ from SN+BAO (left) and SN+BAO+CMB (right) data using the CPL parameterization. Taken from [71].

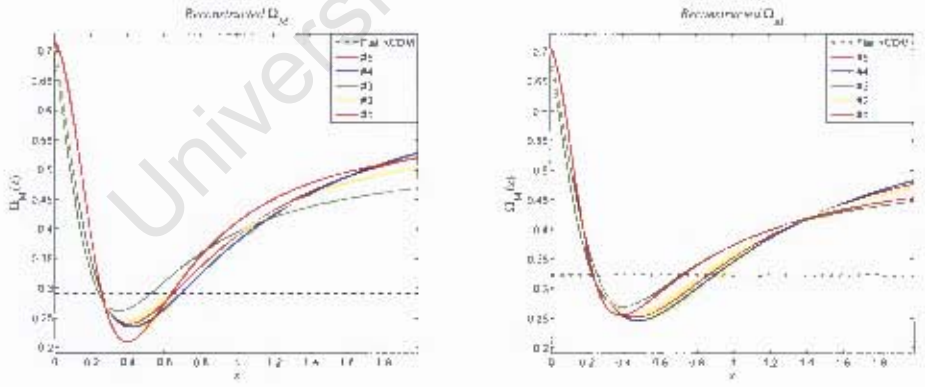

Figure 4.14: Effective $\Omega_M(z)$ for our 5 best-fit void models to SN (left) and SN+H (right) data, along with that of the ΛCDM model. Notice how similar these void curves are to those from [71].

Comparing these to the plot shown earlier, Fig. 2.1, we see similarities over most of the redshift range. However, the data calculates negative Ω_M at some of the low redshift points, which can be classed as unphysical, as Ω_M is strictly positive definite, although we should keep in mind that Ω_M reconstructed from the data should have error bars on it, anyway, so nothing rigorous can be said about the CP using this quantity just yet.

In Fig. 4.15 we plot the effective Ω_K for our 5 best-fit void models to SN (left) and SN+H (right) data, as well as that for the flat ΛCDM model given by the black dotted line going through $\Omega_K = 0$. Notice the huge difference between the void models and that of ΛCDM as we get close to the origin. In the future we may be able to compute Ω_K as given by the observations, and thus, not only determine whether our universe is curved or not, but whether or not we live at the center of a large cosmic void described by the LTB solution.

Finally, we show plots of $L(z)$ and $C(z)$ in Fig.'s 4.16 and 4.17, respectively. Both of these quantities are zero in FLRW models, however in LTB models they are generally different from zero, as such, providing us with a test of the CP.

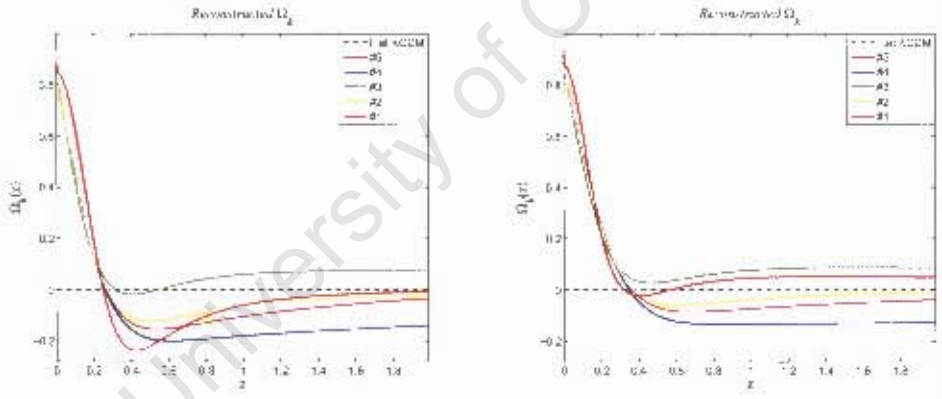

Figure 4.15: Effective $\Omega_K(z)$ for our 5 best-fit void models to SN (left) and SN+H (right) data, along with that of the ΛCDM model.

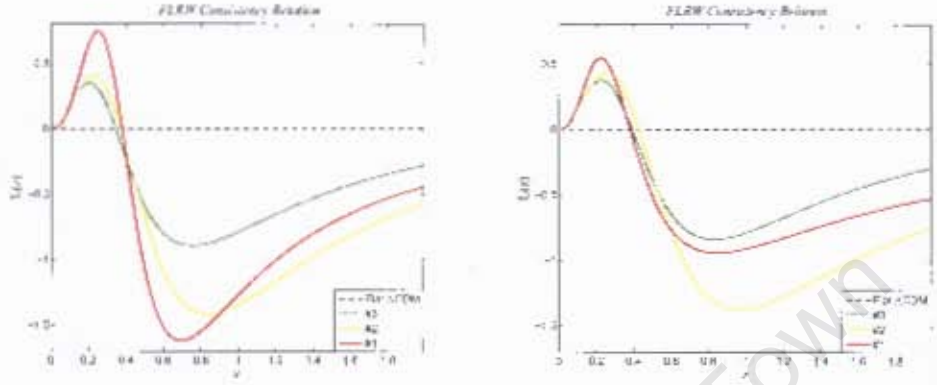

Figure 4.16: $L(z)$ diagnostic for our 5 best-fit void models to SN (left) and SN + H (right) data.

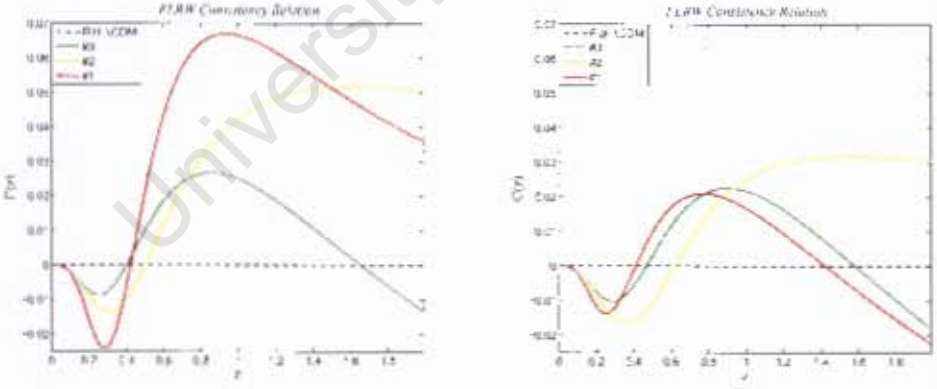

Figure 4.17: $C'(z)$ diagnostic for our 5 best-fit void models to SN (left) and SN+H (right) data.

Chapter 5

Conclusion and Outlook

The present phase of accelerated expansion of the universe, as deduced from the redshifting of type Ia supernovae (SN), is widely accepted as being due to some exotic cosmological fluid possessing a negative pressure that has been dubbed 'dark energy' (DE). In particular, when this DE is assumed to be in the form of Einstein's cosmological constant Λ, and further assuming spatially flat hypersurfaces, requires it to make up approximately 74% of the total energy in the universe, with dark matter contributing roughly 26%, and the baryons of which we are made accounts for only 4%. This current concordance model of cosmology, the ΛCDM model which is based on the homogeneous and isotropic Friedmann-Lemaître-Roberton-Walker (FLRW) metric, can account for the bulk of the cosmological data we have at present, yet we have no theoretical understanding of the origin and nature of Λ. For this reason, we have investigated the isotropic but inhomogeneous Lemaître-Tolman-Bondi (LTB) model, as it currently displays remarkable potential as a viable alternative to dark energy. Although forcing us to be close to the center of the universe in order to agree with the highly isotropic background radiation field we observe as the Cosmic Microwave Background (CMB), occupying a large (few gigaparsecs) underdense region in spacetime, or void, containing only baryons and DM, allows us to account for the observed accelerated expansion of the universe without the need for a cosmological constant.

Our investigation into LTB void models confirmed numerous results that already exist in the literature regarding LTB models in general. We studied 5 different parameterizations of the dimensionless matter density today, i.e. $\Omega_{M0}(r)$, and in particular, introduced a new parameterization that could control the smoothness of the void at the center. First of all, we considered the effective deceleration parameter

$q(z)$, and showed that when a 'weak-singularity' exists, the universe will necessarily undergo acceleration today (i.e. $q_0 < 0$), whereas when the weak-singularity is absent, then an effective deceleration (i.e. $q_0 > 0$) is peceived, thus confirming the result by [109]. Secondly, we showed that all of our 5 different void models considered can fit the ΛCDM distance modulus to well within the current accuracy of SN data, and in particular, the new parameterization we came up with can do so to arbitrary accuracy (although already shown by [113], thus supporting the result of [116] that for a given FLRW model, there exists an LTB model that can match its distance modulus.

Secondly, we confronted all 5 void parameterizations with the largest compilation of SN to date, namely the Constitution set consisting of 397 SN [19], as well as the Hubble rate ($H(z)$) data [23] consisting of 10 points after adding in the HST [134] point, and obtained better fits to these observations than the ΛCDM model. Our findings pointed out that using the SN data alone will not suffice to allow the testing of the Copernican Principle (CP), in contrast to previous claims [113]. We then pointed out that the $H(z)$ data, when used in conjunction with the SN data, could potentially be used as a means to distinguish between ΛCDM and LTB void models that abide by the idea of post-inflationary homogeneity by having a zero bang time function (i.e. $t_B(r) = 0$). The resulting voids we found had a mean FWHM of 6.6 ± 0.4 Gpc, which is truly cosmic in size, and is in excellent agreement with that found in previous studies [120], where the FWHM is 6.5 Gpc. In addition, best-fit model corresponding to the new parameterization came out to be not only one which is smooth at the center, but smoother than that of the best-fit Gaussian model, implying that the latest SN dataset prefers voids that are smooth at the center, although we found that pointier voids can give comparable fits to the data.

We finally note that our best-fit void models show remarkable similarities in terms of the observables studied in [71], which involved the application of the CPL DE parameterization to the current SN, BAO and CMB datasets in an FLRW context. Excluding the tight constraints on the parameters from the CMB, [71] showed that the universe may actually be undergoing deceleration today – a conclusion we reach as well when we consider the effective deceleration parameter – which is in contrast with the present-day accelerated expansion as predicted in the concordance model. Moreover, we discovered another hint of non-ΛCDM behaviour upon contructing the effective dimensionless matter density $\Omega_{_M}(z)$ using the Hubble rate data, as we found, on average, that $\Omega_{_M}(z)$ had a non-zero slope, which is impossible

in a ΛCDM universe. However, more accurate $H(z)$ data will reveal whether or not our result can be confirmed, or whether it is next to impossible to achieve the required accuracy needed to detect a non-ΛCDM universe.

At least two topics has so far arisen out of this study. The subtlety regarding the way in which the Hubble parameter today (H_0) not only affects the overall scaling of the $\mu(z)$ curve, but also its overall shape. We propose to fit for the intrisic luminosity of the SN, which is related to H_0, at the same time in order to obtain the best-fit possible to the data, as well as to find a way to successfully marginalize over H_0 without losing information such as the overall shape of $\mu(z)$. In another study, we plan to determine the matter power spectrum as predicted by the LTB model, where we will use the results of [17] (see Appendix C), as this would provide the much-needed rigorous constraints on LTB models, so that we may finally rule them out in favour of ΛCDM, or support the idea that we live at the center of a giant cosmic void in an otherwise Einstein de Sitter universe.

Appendix A

Allowing $\Omega_{\rm out}$ to be Free

We briefly highlight the investigation we undertook into allowing $\Omega_{\rm out}$ to be free when fitting to the SN data, using void model #1. The best-fit to SN parameters we found were: $H_0 = 64.10$ km/s/Mpc, $\Omega_{\rm in} = 0.17$, $\sigma = 2.95$ Gpc, $\log_{10}\nu = 2.2\times10^{-5}$ and $\Omega_{\rm out} = 2.28$.

Fig. A.1 shows the joint-parameter confidence contours between $\Omega_{\rm out}$ and the other parameters (note that $\Omega_{\rm out}$ vs. ν is not shown, due to time constraints). The degeneracies between these parameters were briefly discussed in Chapter 3, and these plots simply serve as a supporting illustration.

Fig. A.2 shows the 1D likelihood distribution of $\Omega_{\rm out}$, and we see that $\Omega_{\rm out}$ is poorly constrained, due to the lack of higher redshift data.

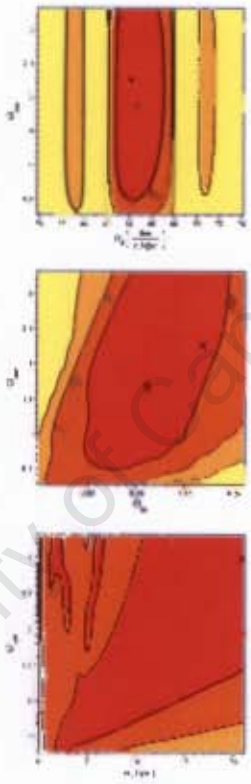

Figure A.1: Joint-parameter likelihood contours from SN constraints. Black crosses indicates the marginalized best-fit values and blue crosses show the best-fit to SN values.

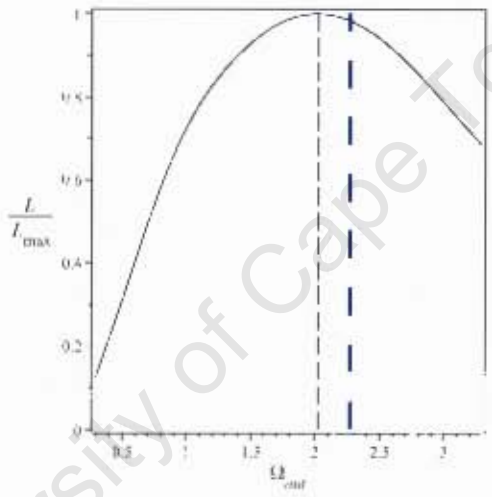

Figure A.2: One-parameter likelihood distribution for Ω_{out} from SN constraints. The black dashed line corresponds to the marginalized best-fit value, while the blue space-dashed line indicates the best-fit to SN value.

Appendix B

Results from other SN Data Sets

In light of the $\nu = 1$ issue arising from fitting void model #1 to the Constitution sample [19], we wanted to see what results our Fortran code would give when fitting the void to other SN data sets, as a check to see that the code was not picking out $\nu = 1$ everytime. In Table B.1, we show the best-fit model parameters of void #1 when fitting to the Davis et al. sample [44] (A), the Union sample [45] (B), the original Constitution sample [19] (C) (recall that we modified the errors to account for intrisic dispersion) and finally the ConstitutionT (where "T" stands for "truncated") sample [137] (D), who removed a total of 34 SN from the Constitution sample in order to avoid tension between the data sets regarding the results of cosmological parameters. From these results we see that the best-fit ν is different

Table B.1: Best-fit parameters of void model #1 from various SN data sets.

Data Set #	H_0 km/s/Mpc	$\Omega_{\rm in}$	σ Gpc	$\log_{10}\nu$	χ^2_{SN}	$\frac{\chi^2_{SN}}{\rm ndf}$	FWHM Gpc
A	65.78	0.065	9.26	2.95	195.38	1.03	10.19
B	70.60	0.095	6.50	5.00	310.68	1.02	7.14
C	64.18	0.140	2.17	8×10^{-6}	459.93	1.17	5.44
D	64.00	0.158	2.33	3.4×10^{-2}	270.88	0.75	5.52

for the other data sets, and higher in fact, due to the lack of low-redshift SN in those samples, since ν only affects $\Omega_{M_0}(r)$ close to the origin.

Appendix C

Perturbation Theory in LTB Cosmology

In this appendix, the paper published by the author along with Dr. Chris Clarkson and Dr. Timothy Clifton has been inserted verbatim. This paper derives the set of 'Master equations' describing the evolution of the linearly perturbed background quantities in an LTB spacetime. This work is important for future studies of the matter-power spectrum as well as the Baryon Acoustic Oscillations present in the galaxy power spectrum as observed in an LTB spacetime, which is expected to put enormous strain on these models and may even rule them out once and for all.

Although the paper was not written in the own words of the author, the author was actively involved in the research that was carried out, and contributed mainly to the calculating and checking of all of the LTB perturbation and background equations.

Journal of Cosmology and Astroparticle Physics
An IOP and SISSA journal

Perturbation theory in Lemaître-Tolman-Bondi cosmology

Chris Clarkson,[a] **Timothy Clifton**[b] **and Sean February**[a]

[a]Cosmology & Gravity Group, Department of Mathematics and Applied Mathematics, University of Cape Town, Rondebosch 7701, Cape Town, South Africa
[b]Department of Astrophysics, University of Oxford, Keble Road, Oxford, OX1 3RH, U.K.

E-mail: chris.clarkson@uct.ac.za, tclifton@astro.ox.ac.uk, sean.astrofizik@gmail.com

Received April 14, 2009
Accepted May 25, 2009
Published June 18, 2009

Abstract. The Lemaître-Tolman-Bondi solution has received much attention as a possible alternative to Dark Energy, as it is able to account for the apparent acceleration of the Universe without any exotic matter content. However, in order to make rigorous comparisons between these models and cosmological observations, such as the integrated Sachs-Wolfe effect, baryon acoustic oscillations and the observed matter power spectrum, it is absolutely necessary to have a proper understanding of the linear perturbation theory about them. Here we present this theory in a fully general, and gauge-invariant form. It is shown that scalar, vector and tensor perturbations interact, and that the natural gauge invariant variables in Lemaître-Tolman-Bondi cosmology do not correspond straightforwardly to the usual Bardeen variables, in the limit of spatial homogeneity. We therefore construct new variables that reduce to pure scalar, vector and tensor modes in this limit.

Keywords: cosmological perturbation theory, gravity

ArXiv ePrint: 0903.5040

doi:10.1088/1475-7516/2009/06/025

JCAP06(2009)025

Contents

1 Introduction

The concordance model of cosmology is a result of assuming that the Universe is approximately the same at all points in space, and that at every point it appears isotropic. The observations we make locally can then be extrapolated to the Universe at large, and the resulting Friedmann-Lemaître-Robertson-Walker (FLRW) model can be used to interpret all cosmological observations. The FLRW models are, of course, very well understood, and have proved to be highly successful in very many different capacities. Unfortunately, despite its aesthetic appeal and mathematical simplicity, the adoption of the FLRW cosmology has led

JCAP06(2009)025

to the undesirable requirement that the Universe must be filled with a smoothly distributed and gravitationally repulsive exotic substance, known as Dark Energy. The conceptual problems associated with Dark Energy are well known, and are distressing enough that it now seems worth investigating alternative, less appealing models.

One such alternative is the spherically symmetric, dust dominated cosmological solution of Lemaître, Tolman and Bondi [1]. This model is isotropic about a single point in space, in agreement with local galaxy surveys and observations of the Cosmic Microwave Background, but is anisotropic everywhere else [2]. As such, we are required to live very near the centre of symmetry, indicating a break with the Copernican Principle that *"the Earth is not in a central, specially favoured position"* [3]. The Lemaître-Tolman-Bondi (LTB) model allows the Hubble rate to vary with radial distance from the centre of symmetry, as well as with time, and so allows for the possibility of apparent acceleration (if observations within them are interpreted in an FLRW frame-work), while no part of them need undergo any accelerating expansion.

One may then try and argue on aesthetic grounds, or on the grounds of presumed early Universe physics, which of these models is more likely. Clearly there are good reasons to disfavour either, depending on which one abhors most: the Earth being in a special position in the Universe, or the existence of Dark Energy, which requires us to live at a special time when the acceleration is just starting to kick in. However, a more objective (and scientific) approach to the problem would be to try and distinguish between the two models with direct observations. This has been attempted a number of different times in the literature already [4]. However, in order to make comparisons to different types of astrophysical data it is absolutely necessary to have a proper understanding of how structures form and behave in these models, and this means understanding their perturbation theory. An alternative approach is to try to test the Copernican principle directly [5], but this is very difficult to achieve at present through direct tests.

For observations such as the integrated Sachs-Wolfe effect, Rees-Sciama effect, or matter power spectrum it is obvious that a proper interpretation of the data is dependent on understanding the relevant perturbation theory. However, other observations, that do not necessarily require perturbation theory in FLRW, will also require a knowledge of perturbation theory in the LTB case. An example is the use of baryon acoustic oscillations as a probe of cosmology. In FLRW it suffices to consider comoving points in an unperturbed fluid, to see how length scales at recombination are evolved onto distance measures on our past light cone. In an LTB universe, however, the rate of growth of structure can be different at different places, and the peculiar velocity of perturbations need not cancel when averaged over suitable scales (in fact, one may naively expect otherwise). Likewise, when considering light reflecting off a galaxy cluster in FLRW it may suffice to consider that on average the motions of galaxy clusters will cancel out, so that approximating galaxy clusters as being comoving with the background fluid may be sufficient to get accurate results. In an LTB universe this is unlikely to be true, as gradients in gravitational potentials will develop due to different growth rates at different positions.

As well as the requirement of understanding linear perturbation theory in order to accurately account for already established probes of cosmology, there is also the possibility of finding new observational phenomena that could be used to distinguish the LTB and FLRW cosmologies, or constrain the type of LTB models that are observationally viable. An example of this is the potential coupling of scalar gravitational potentials to tensor gravitational waves. In an FLRW background (to linear order) the decomposition theorem ensures that no such

coupling occurs. On a homogeneous background scalar, vector and tensor modes then evolve independently. In an inhomogeneous LTB background, however, the decomposition theorem will only be valid on the two dimensional surfaces of spherical symmetry. In the three dimensional space there will be no such theorem, and in general one should expect coupling to occur between what we conventionally think of as 'scalar', 'vector' and 'tensor' modes. Though complicated, such effects could potentially be used as probes of the geometry of the universe.

In section 2 we introduce the formalism required for perturbation theory about a spherically symmetric background. In section 3.1 and 3.2 we present the perturbation equations, and in section 3.3 and 4 we discuss their solutions and how they relate to perturbation theory in FLRW. Finally, in section 5 we conclude. The appendices contain information about gauge invariant quantities for the metric perturbation, and the perturbation equations for some special cases.

We use units in which $c = G = 1$, throughout.

2 Perturbation theory on a spherically symmetric background

Perturbations on a spherically symmetric space-time have been considered a number of times in the literature, mostly in the context of modelling static and stationary stars [6]. A time dependent formalism was first developed by Seidel [7], and later specialised to a space-time containing a perfect fluid by Gundlach and Martín-García (GMG) [8]. Perturbations of self similar models have recently been investigated in [9], and have the advantage that all PDEs reduce to ODEs in the system of perturbation equations. A limited class of perturbations in LTB cosmology have also been studied by Zibin [10].

Different formalisms exist in the literature for constructing both the system of perturbation equations, and the gauge-invariant variables. Gerlach and Sengupta [11] (GS) developed a formalism based on a 2+2 covariant split of the metric and energy-momentum tensor. This turns the field equations into a system of second-order PDEs, and was made explicit by GMG, who found a closed set of master equations describing all perturbations. Their approach was used in the study of self-similar LTB perturbations performed in [9]. Alternatively, a covariant 1+1+2 formalism has been developed in [12], which builds on the covariant 1+3 formalism that has been usefully applied in cosmology [13]. Here the Bianchi and Ricci identities, plus the Ricci rotation coefficients for the semi-tetrad introduced, are covariantly split into a system of first-order differential equations. This formalism has not yet been reduced to a tractable set of master equations for a general space-time, but has been used by [10] to study LTB perturbations. Here we apply the GS formalism developed by GMG to the case of an LTB space-time. This results in a simple set of coupled second-order PDEs that describe general perturbations to the space-time, in a gauge invariant way.

2.1 The LTB background

The unperturbed LTB line-element can be written

$$ds^2 = -dt^2 + \frac{a_\parallel^2(t,r)}{(1-\kappa r^2)}dr^2 - a^2(t,r)r^2 d\Omega^2, \tag{2.1}$$

where $a_\perp = (ra_\perp)_{,r}$ and $\kappa = \kappa(r)$ is a free function of r. The FLRW scale factor, a, has been replaced here by two new scale factors, $a_\parallel$ and $a_\perp$, describing expansion parallel and

perpendicular to the radial direction, respectively. For future use we will define the radial and azimuthal Hubble rates to be

$$H_{\parallel} \equiv \frac{\dot{a}_{\parallel}}{a_{\parallel}} \quad \text{and} \quad H_{\perp} \equiv \frac{\dot{a}_{\perp}}{a_{\perp}}, \tag{2.2}$$

where an over-dot denotes partial differentiation with respect to t. The analogue of the Friedmann equation in this space-time is then given by

$$H_{\perp}^2 = \frac{M}{a_{\perp}^3} - \frac{\kappa}{a_{\perp}^2}, \tag{2.3}$$

where $M = M(r)$ is another free function of r, and the locally measured energy density is

$$8\pi\rho = \frac{(Mr^3)_{,r}}{a_{\parallel}a_{\perp}^2 r^2}, \tag{2.4}$$

which obeys the conservation equation

$$\dot{\rho} + (2H_{\perp} + H_{\parallel})\rho = 0. \tag{2.5}$$

The acceleration equations in the perpendicular and parallel directions are

$$\frac{\ddot{a}_{\perp}}{a_{\perp}} = -\frac{M}{2a_{\perp}^3} \quad \text{and} \quad \frac{\ddot{a}_{\parallel}}{a_{\parallel}} = -4\pi\rho + \frac{M}{a_{\perp}^3}. \tag{2.6}$$

For what follows it will also be useful to define the radial derivative

$$X' \equiv \frac{\sqrt{1 - \kappa r^2}}{a} X_{,r}. \tag{2.7}$$

This derivative does not commute with the time derivative, but instead obeys

$$(\dot{X})' = (X')^{\cdot} - H_{\parallel} X'. \tag{2.8}$$

We also define the curvature function

$$W \equiv \frac{\sqrt{1 - \kappa r^2}}{a_{\perp} r}. \tag{2.9}$$

The following relations are then obeyed

$$H_{\perp}' = W(H_{\parallel} - H_{\perp}), \tag{2.10}$$

$$\dot{W} = -H_{\perp} W, \tag{2.11}$$

$$W' = -W^2 - 4\pi\rho - H_{\perp}H_{\parallel} + \frac{M}{2r^3}. \tag{2.12}$$

In the perturbation equations that follow we will choose to eliminate κ in favour of W, so that the equations take their simplest form.

2.2 Harmonic functions

A natural way to split this space-time is in a 2+2 decomposition, so that the space-time manifold becomes $M^4 = M^2 \times S^2$, where S^2 indicates the 2 dimensional spherically symmetric surfaces. We will use lower case Latin indices $a, b, c, \ldots$ to denote coordinates in S^2, upper case Latin indices $A, B, C, \ldots$ to denote coordinates in M^2, and Greek indices $\mu, \nu, \xi, \ldots$ to denote coordinates that run over all 4 space-time dimensions.

In FLRW cosmology, any perturbation can be split into scalar, vector and tensor (SVT) modes that decouple from each other, and so evolve independently (to first order). This classification is based on how they transform on the homogeneous and isotropic spatial hypersurfaces, and is essentially just a generalisation of Helmholtz's theorem [14].

Such a split cannot usefully be performed in the same way here, as the background is no longer spatially homogeneous, and modes written in this way would couple together (as we shall see). However, one can perform an analogous classification based on how the perturbations transform on the surfaces of spherical symmetry. This results in a decoupling of the perturbations into two independent modes, called 'polar' (or even) and 'axial' (or odd), which are analogous, but not equivalent, to scalar and vector modes in FLRW. Unlike the FLRW case, however, there is no further decomposition into tensor modes as no non-trivial symmetric, transverse and trace-free rank 2 tensors can exist on S^2. Therefore, only two distinct sectors exist. Scalars (rank 0 tensors) on S^2 can then be expanded as a sum of polar modes, and higher rank tensors on S^2 can be expanded in sums over both the polar and axial modes. Only a scalar can contain spherical perturbations (given by $\ell = 0$, defined below), and only scalars and vectors (i.e., tensors of rank 0 and 1) can contain a dipole term ($\ell = 1$). Higher multipoles can be present in all tensors.

An appropriate family of basis functions for this split are tensor spherical harmonics. These are derived from the usual spherical harmonic functions, $Y^{(\ell m)}(x^a)$, that obey

$$\bar{\nabla}^2 Y^{(\ell m)} = -\ell(\ell-1) Y^{(\ell m)}, \tag{2.13}$$

where the Natural number, ℓ, gives the angular scale of the perturbation. The Laplacian, $\bar{\nabla}^2$ here, is on the surface of spherical symmetry, and is given by $\bar{\nabla}^2\phi = \gamma^{ab}\phi_{:ab}$, where the colon subscript indicates a covariant derivative with respect to the metric on the unit sphere, γ_{ab}. Scalar perturbations on S^2 can then be written with their angular dependence given in terms of the solutions to this equation, and expanded as

$$\phi(x^A, x^a) = \sum_{\ell=0}^{\infty} \sum_{m=-\ell}^{m=\ell} \phi^{(\ell m)}(x^A) Y^{(\ell m)}(x^a). \tag{2.14}$$

It is now possible to construct a basis for all higher rank tensors from $Y^{(\ell m)}$, its covariant derivatives, and the contractions of those derivatives with the fundamental antisymmetric tensor, ϵ_{ab}. Modes that can be described without requiring ϵ_{ab} are called polar, while those that require ϵ_{ab} are called axial.

We can now form harmonic functions for higher rank tensor perturbations with polar degrees of freedom by first defining the vector, for $\ell \geq 1$:

$$Y_a^{(\ell m)} \equiv Y_{:a}^{(\ell m)}. \tag{2.15}$$

We define also the trace-less tensor, for $\ell \geq 2$:

$$Y_{ab}^{(\ell m)} \equiv Y_{:ab}^{(\ell m)} + \frac{\ell(\ell+1)}{2} Y^{(\ell m)} \gamma_{ab}. \tag{2.16}$$

Taking divergences of $Y_a^{(\ell m)}$ and $Y_{ab}^{(\ell m)}$ reduces these expressions to equations involving $Y^{(\ell m)}$.

For axial perturbations on S^2 we define a divergence-free vector harmonic, for $\ell \geq 1$,

$$\bar{Y}_a^{(\ell m)} \equiv \epsilon_a{}^b Y_b^{(\ell m)}. \tag{2.17}$$

We can then construct a symmetric and trace-free rank-2 axial harmonic function by defining, $\ell \geq 2$,

$$\bar{Y}_{ab}^{(\ell m)} \equiv 2\bar{Y}_{(a:b)}^{(\ell m)} = -2\epsilon^d{}_{(a} Y_{:b)d}^{(\ell m)}, \tag{2.18}$$

where round brackets around indices denote symmetrisation, as usual. Taking covariant derivatives, this tensor harmonic can be reduced to an expression involving $\bar{Y}_a^{(\ell m)}$.

For both parities, the 'vector harmonics' obey

$$\bar{\nabla}^2 Y_a^{(\ell m)} = [1 - \ell(\ell+1)] Y_a^{(\ell m)} \tag{2.19}$$

(similarly for $\bar{Y}_a^{(\ell m)}$), and the 'tensor harmonics' obey

$$\bar{\nabla}^2 Y_{ab}^{(\ell m)} = [1 - \ell(\ell+1)] Y_{ab}^{(\ell m)}. \tag{2.20}$$

Because the vector harmonics are orthogonal for each ℓ, any rank-1 tensor perturbation can now be expanded as

$$\begin{aligned} \phi_a(x^A, x^a) = \sum_{\ell=1}^{\infty} \sum_{m=-\ell}^{m=\ell} & \phi^{(\ell m)}(x^A) Y_a^{(\ell m)}(x^\alpha) \\ & + \bar{\phi}^{(\ell m)}(x^A) \bar{Y}_a^{(\ell m)}(x^a), \end{aligned} \tag{2.21}$$

where $\phi^{(\ell m)}$ and $\bar{\phi}^{(\ell m)}$ are independent for each (ℓm), and are given by

$$\phi^{(\ell m)} = \frac{1}{\ell(\ell+1)} \int \mathrm{d}\Omega \, (\phi^a{}_{:a}) Y^*_{(\ell m)} \tag{2.22}$$

and

$$\bar{\phi}^{(\ell m)} = \frac{1}{\ell(\ell+1)} \int \mathrm{d}\Omega \, (\epsilon^{ab} \phi_{b:a}) Y^*_{(\ell m)}. \tag{2.23}$$

There are no $\ell = 0$ vector dof because $\ell = 0$ describes spherical modes.

Finally, let us consider trace-less rank 2 tensor perturbations on S^2. A suitable orthogonal basis in this case, for $\ell \geq 2$, is given by the two harmonic functions $Y_{ab}^{(\ell m)}$ and $\bar{Y}_{ab}^{(\ell m)}$, defined above. Any rank 2 trace-free tensor perturbation can then be written

$$\begin{aligned} \phi_{ab}(x^A, x^a) = \sum_{\ell=2}^{\infty} \sum_{m=-\ell}^{m=\ell} & \phi^{(\ell m)}(x^A) Y_{ab}^{(\ell m)}(x^a) \\ & + \bar{\phi}^{(\ell m)}(x^A) \bar{Y}_{ab}^{(\ell m)}(x^a), \end{aligned} \tag{2.24}$$

where

$$\begin{aligned} \phi^{(\ell m)} &= 2\frac{(\ell-2)!}{(\ell+2)!} \int \mathrm{d}\Omega \, (\phi^{ab}{}_{:ba}) Y^*_{(\ell m)}, \\ \bar{\phi}^{(\ell m)} &= 2\frac{(\ell-2)!}{(\ell+2)!} \int \mathrm{d}\Omega \, (\epsilon_a{}^c \phi^{ab}{}_{:bc}) Y^*_{(\ell m)}. \end{aligned} \tag{2.25}$$

As our background is spherically symmetric, all perturbations with different (ℓm) decouple from each other. This is analogous to the decoupling of Fourier modes in FLRW. We shall therefore drop the (ℓm) labels on all quantities that follow. Where a function of x^A is multiplied by a harmonic function, a sum over ℓ and m is implied.

2.3 Metric perturbations

Gauge invariant variables for general perturbations of a spherically symmetric background, with arbitrary matter content, have been formulated by Gerlach and Sengupta (GS) [11]. We reiterate their results, relevant to the present study, in appendix A. We then review the perfect fluid formalism of GMG, specialised to a dust filled universe, in appendix B. These studies show that there is a preferred gauge, known as the Regge-Wheeler (RW) gauge [15], in which the perturbation variables are equal to gauge invariant quantities (comparable to the longitudinal, or conformal Newtonian gauge, of FLRW). The RW gauge is the choice that any off-diagonal polar modes in the metric that have an angular index are zero, and that in the axial modes there is no perturbation to the g_{ab} components (i.e. the S^2 components). Calculations performed in the RW gauge are then equivalent to those performed when considering the gauge invariant variables of [8] and [11].

The general form of polar perturbations to the metric can now be written, in RW gauge, as[1]

$$\mathrm{d}s^2 = -\left[1+(2\eta-\chi-\varphi)Y\right]\mathrm{d}t^2 - \frac{2a_\parallel \varsigma Y}{\sqrt{1-\kappa r^2}}\mathrm{d}t\mathrm{d}r \tag{2.26}$$

$$-\left[1+(\chi+\varphi)Y\right]\frac{a_\parallel^2\mathrm{d}r^2}{(1-\kappa r^2)} - a^2 r^2(1+\varphi Y)\mathrm{d}\Omega^2,$$

where $\eta(t,r)$, $\chi(t,r)$, $\varphi(t,r)$ and $\varsigma(t,r)$ are equal to the gauge invariant quantities of GS and GMG, as shown in appendices A and B. The general form of polar matter perturbations in this gauge are parameterised by

$$u_\mu = \left[\hat{u}_A - \left(w\hat{n}_A + \frac{1}{2}h_{AB}\hat{u}^B\right)Y, vY_a\right] \tag{2.27}$$

$$\rho = \rho^{\mathrm{LTB}}(1+\Delta Y), \tag{2.28}$$

where v, w and Δ are equal to the gauge invariant quantities of GS and GMG, again, as shown in appendices A and B. The vectors $\hat{u}^A$ and $\hat{n}^A$ indicate background unit vectors in the time-like and space-like radial directions, respectively. They are given by

$$\hat{u}^A = (1,0) \qquad \text{and} \quad \hat{n}^A = \left(0, \frac{\sqrt{1-\kappa r^2}}{a_\parallel}\right). \tag{2.29}$$

The h_{AB} in (2.27) correspond to the linear perturbations to g_{AB}, as shown in (2.26), and are included to ensure the normalisation $u^\mu u_\mu = -1$.

The general form of axial perturbations to the metric, in RW gauge, are

$$\mathrm{d}s^2 = -\mathrm{d}t^2 + \frac{a_\parallel^2}{(1-\kappa r^2)}\mathrm{d}r^2 + a^2 r^2\mathrm{d}\Omega^2 \tag{2.30}$$

$$+ 2k_A\bar{Y}_b\mathrm{d}x^A\mathrm{d}x^b, \tag{2.31}$$

where k_A is equal to the gauge invariant perturbation of GS, from appendix A. Following GS, we also define for later convenience the new variable

$$\Pi = \epsilon^{AB}\left(\frac{k_A}{a_\perp^2 r^2}\right)_{|B}, \tag{2.32}$$

[1] We have changed notation from GMG to avoid potential confusion with notation that is often used in cosmology. In particular we have replaced: $k \to \varphi, \chi \to \chi, \psi \to \varsigma, \eta \to \eta, \alpha \to v, \beta \to \bar{v}, \omega \to \Delta, \gamma \to w$.

where the fundamental anti-symmetric tensor $\epsilon_{AB} = n_A u_B - u_A n_B$ and a pipe denotes the covariant derivative on M^2. The only axial perturbation that can then occur to the matter content is a perturbation to the matter four velocity, such that

$$u_a = (\bar{u}_A, \bar{v}\bar{Y}_\alpha), \tag{2.33}$$

where $\bar{u}^A$ is defined as in the polar case, and $\bar{v}$ equals one of the gauge invariant variables of GMG, in appendix B.

2.3.1 'Scalar-vector-tensor' variables

The GI variables defined above give a very concise set of governing equations (see below). However, in the FLRW limit we shall see that they mix up the normal SVT modes in a complicated way – for example, the variable φ contains all three types of perturbations. By taking combinations of the variables defined in the perturbed metric we may form variables which do reduce to scalars, vectors, or tensors in the FLRW limit, and so may be used to identify generalised SVT modes. Such variables are:

Tensors:

$$\text{polar:} \quad \hat{\chi} = \chi \tag{2.34}$$

$$\text{axial:} \quad \hat{\Upsilon} = \Pi'' - 6W\Pi' + \left(8W^2 - \frac{\ell(\ell+1)-2}{a_\perp^2 r^2}\right)\Pi + 16\pi\frac{(\rho v)'}{a_\perp^2 r^2}, \tag{2.35}$$

Vectors:

$$\text{polar:} \quad \hat{\xi} = \frac{3a_\perp}{2W}\left[\frac{1}{r^3}\left(r^2\chi\right)' + \left(\frac{\varsigma}{r}\right)'' + 2W\left(\frac{\varsigma}{r}\right)' - \left(\frac{\ell(\ell+1)-3}{a_\perp^2 r^2} - 3W^2\right)\frac{\varsigma}{r}\right] \tag{2.36}$$

$$\text{axial:} \quad \hat{v} = \bar{v}, \tag{2.37}$$

Scalars:

$$\hat{\zeta} \equiv \lambda'' + 2W\lambda' - \frac{\ell(\ell+1)}{a_\perp^2 r^2}\lambda + rW\xi' + r\left(3W^2 - \frac{1}{a_\perp^2 r^2}\right)\xi, \tag{2.38}$$

where

$$\hat{\lambda} \equiv 8\pi\rho a_\perp \left[H_\perp^{-1}\Delta - 3v\right]. \tag{2.39}$$

We shall justify these variables in section 4.3.

3 Master equations

The equations of motion governing the dynamics may be reduced to a coupled system of evolution equations and constraints. For the polar sector the equations come in the form of three coupled PDEs for χ, φ and ς, with all other non-trivial gauge invariant variables determined from the solution of this system. For the axial modes, the dynamics are determined by a much simpler system of equations for the variables Π and $\bar{v}$.

3.1 Polar perturbation equations for $\ell > 2$

Substituting the polar perturbed metric tensor (2.26), and the perturbed matter quantities, (2.27) and (2.28), into the field equations results in a system of three coupled master evolution equations for the three variables χ, φ and ς. The remaining variables associated with the fluid can then be determined directly from the solution to this system.

The three evolution equations are

$$-\ddot{\chi} - \chi'' - 3H_{\parallel}\dot{\chi} - 2W\chi' + \left[16\pi\rho - \frac{6M}{a_{\perp}^3} - 4H_{\perp}(H_{\parallel} - H_{\perp}) - \frac{(\ell-1)(\ell+2)}{a^2 r^2}\right]\chi \quad (3.1)$$
$$- -2(H_{\parallel} - H_{\perp})\varsigma' - 2\left[H_{\parallel}' - 2(H_{\parallel} - H_{\perp})W\right]\varsigma$$
$$- 4(H_{\parallel} - H_{-})\dot{\varphi} - 2\left[8\pi\rho - \frac{3M}{a_{-}^3} - 2H_{-}(H_{\parallel} - H_{-})\right]\varphi,$$

and

$$\ddot{\varphi} + 4H_{-}\dot{\varphi} \quad 2\left(\frac{1}{a_{\perp}^2 r^2} \quad W^2\right)\varphi = \quad H_{-}\dot{\chi} + W\chi' \quad \left[2W^2 \quad \frac{\ell(\ell+1)+2}{2a_{-}^2 r^2}\right]\chi$$
$$+2W(H \quad H_{\parallel})\varsigma, \quad (3.2)$$

and

$$\dot{\varsigma} + 2H_{\parallel}\varsigma - \chi', \quad (3.3)$$

together with the constraint

$$\eta = 0. \quad (3.4)$$

These four equations are the LTB version of Equations (GMG87), (GMG88), (GMG89) and (GMG82) from [8].

The three constraint equations can then be written as

$$8\pi\rho w = (\dot{\varphi})' - (H_{\parallel} - 2H \quad)\varphi' - W\dot{\chi} + H_{\perp}\chi' \quad (3.5)$$
$$+ \left[\frac{\ell(\ell+1)+2}{2a^2 r^2} + H_{\perp}^2 + 2H_{-}H_{\parallel} - W^2 - 4\pi\rho\right]\varsigma,$$
$$8\pi\rho\Delta = -\varphi'' - 2W\varphi' + (H \quad + 2H_{\perp})\dot{\varphi} + W\dot{\chi}' + H_{-}\dot{\chi} \quad (3.6)$$
$$- \left[\frac{\ell(\ell+1)}{a_{\perp}^2 r^2} + 2H^2 + 4H_{\parallel}H_{-} \quad 8\pi\rho\right](\chi + \varphi)$$
$$- \frac{(\ell-1)(\ell+2)}{2a_{-}^2 r^2}\chi + 2H_{\perp}\varsigma' - 2(H_{\parallel} - H_{\perp})W\varsigma,$$
$$8\pi\rho v = -\dot{\varphi} - \frac{\dot{\chi}}{2} + H_{\parallel}(\chi + \varphi) + \frac{\varsigma'}{2}. \quad (3.7)$$

These are the LTB versions of the equations (GMG93), (GMG94) and (GMG95) from [8]. It is also useful to consider the evolution equations that result from differentiating (3.5), (3.6) and (3.7). These take the particularly simple form

$$\dot{v} = \frac{\dot{\chi}}{2} + \frac{\dot{\varphi}}{2}, \quad (3.8)$$
$$\dot{w} = \frac{\varphi'}{2} - H_{\parallel}w - \frac{H_{\parallel}}{2}\varsigma, \quad (3.9)$$

$$\dot{\Delta} + \left(w + \frac{\varsigma}{2}\right)' = -\frac{\dot{\chi}}{2} - \frac{3\dot{\varphi}}{2} + \frac{\ell(\ell+1)}{a_\perp^2 r^2} v - \frac{\rho'}{\rho}\left(w + \frac{\varsigma}{2}\right) - 2W\left(w + \frac{\varsigma}{2}\right), \tag{3.10}$$

and are the LTB versions of (GMG96), (GMG97) and (GMG98). There are then six coupled equations for the six variables χ, φ, ς, w, Δ and v.

Equations (3.1) (3.10) are clearly more complicated than their FLRW counterparts, but the fact that they can be written as concisely as they are above is quite remarkable.

For very large angle fluctuations, with $\ell = 0$ or 1, the field equations no longer give $\eta = 0$, which has been used to simplify the equations in this section. Instead, there are additional gauge freedoms that can be used to simplify (3.1) (3.10). These are discussed in appendix C.

3.2 Axial perturbation equations

The axial perturbation equations take a simpler form than their polar counterparts. Because we are considering dust dominated cosmologies, the field equations give us $\dot{\bar{v}} = 0$, and so $\bar{v} = \bar{v}(r)$ and must be set by initial conditions. For $\ell > 2$ the metric perturbation Π can be shown to obey the wave equation

$$-\ddot{\Pi} + \Pi'' + (6H_\perp + H_\parallel)\dot{\Pi} + 6W\Pi' - \left[16\pi\rho + \frac{(\ell-2)(\ell+3)}{a_\perp^2 r^2}\right]\Pi = -16\pi\frac{(\rho\bar{v})'}{a_\perp^2 r^2}, \tag{3.11}$$

which is the LTB version of (GMG69). This is the only dynamical equation that needs solving, for the single variable Π. Once this equation is solved it gives the axial metric perturbations, k_A, via

$$(\ell-1)(\ell+2)k_A = 16\pi\rho a_\perp^2 r^2 \bar{v} u_A - \epsilon_{AB}(a_\perp^4 r^4 \Pi)^{|B}. \tag{3.12}$$

Clearly $\ell = 1$ is a special case. For large angle perturbations of this type we have $(a_\perp^4 r^4 \dot{\Pi}) = 0$ and $(a_\perp^4 r^4 \Pi)' = -16\pi a_\perp^2 r^2 \rho\bar{v}$. The solution for Π is then

$$\Pi = -\frac{2}{a_\perp^4 r^4}\int \frac{v(Mr^3)_{,1}}{\sqrt{1-\kappa r^2}}dr. \tag{3.13}$$

The metric perturbations k_A must then be obtained from inverting eq. (2.32). This will involve an extra degree of freedom in k_A that means it cannot be determined uniquely.

There are no axial perturbations with $\ell = 0$.

3.3 Structure of the equations and solutions

It can be seen from the master equations, (3.1) (3.10), that χ and Π contain gravitational wave degrees of freedom, as their leading derivatives are of the form $-(\ddot{\ }) + (\ )''$ (i.e. a wave equation with a characteristic speed of unity). It can also be seen that ς and $\bar{v}$ look rather like vectors in FLRW cosmology, while φ appears to govern density perturbations like the Newtonian potential. Unfortunately, this roughly analogous behaviour does not hold completely, as we will show below when we consider the FLRW limit. What is clear, however, is that there exist complicated couplings between the variables in this system. We can therefore no longer expect gravitational waves to decouple from density perturbations, as the varying curvature of the background serves to couple these perturbations intimately.

The solutions to the perturbation equations in sections 3.1 and 3.2 will, in general, need to be found numerically. However, if we consider $\ell \geq 2$ and neglect the contribution of the gravitational waves described by χ, we can make progress. With $\eta = \chi = 0$, Equation (3.3) can be integrated to find

$$\varsigma \propto \frac{1}{a_{\parallel}^2}.$$

Clearly, $\varsigma \to 0$ as the Universe expands, and $a_{\parallel} \to \infty$. Assuming χ to be negligible can then be seen to lead to a negligible ς in the late Universe. With $\chi = \varsigma = 0$, Equation (3.2) becomes

$$\ddot{\varphi} + 4H_{\perp}\dot{\varphi} - \frac{2\kappa}{a_{\perp}^2}\varphi = 0. \tag{3.14}$$

This equation can be solved parametrically, together with the analogue of the Friedmann equation, (2.3). There are three solutions, depending on the sign of κ.

For $\kappa < 0$ we find the solution

$$a_{\perp} = \frac{M(1 - \cosh 2\Theta)}{2\kappa} \tag{3.15}$$

$$\varphi = \frac{\cosh\Theta}{\sinh^5\Theta}[c_1 + c_2(\sinh 2\Theta - 6\Theta - 4\tanh\Theta)], \tag{3.16}$$

$$t - t_0 = \frac{M(\sinh 2\Theta - 2\Theta)}{2(-\kappa)^{3/2}}, \tag{3.17}$$

where $c_1 = c_1(r)$, $c_2 = c_2(r)$ and $t_0 = t_0(r)$ are free functions that must be specified as part of the initial conditions. The function $t_0(r)$ is the 'bang time'.

For $\kappa > 0$ we find

$$a_{\perp} = \frac{M(1 - \cos 2\Theta)}{2\kappa} \tag{3.18}$$

$$\varphi = \frac{\cos\Theta}{\sin^5\Theta}[c_1 + c_2(\sin 2\Theta - 6\Theta + 4\tan\Theta)] \tag{3.19}$$

$$t - t_0 = \frac{M(2\Theta - \sin 2\Theta)}{2(\kappa)^{3/2}}. \tag{3.20}$$

Again, c_1, c_2 and t_0 are free functions of r.

Finally, for $\kappa = 0$, a parametric solution is not required, and we find

$$a_{\perp} = \frac{(18M)^{1/3}(t - t_0)^{2/3}}{2} \tag{3.21}$$

$$\varphi = \frac{c_1}{(t - t_0)^{5/3}} + c_2. \tag{3.22}$$

Once more, with c_1, c_2 and t_0 as free functions of r.

In the $\kappa \neq 0$ cases, Θ is a monotonically increasing function of t, and in all three cases c_1 corresponds to a decaying mode, and c_2 to a growing mode. In the cases with $\kappa \leq 0$ the 'growing mode' is itself either a constant (for $\kappa = 0$) or a decreasing function of t (for $\kappa < 0$), and in those cases we mean growing with respect to the other mode, which is decaying faster.

For $\kappa = 0$ the power-law forms of $a_-(t)$ and φ mean that the asymptotic form of both the growing and decaying modes is clear. It can also be seen for $\kappa \neq 0$ that both modes, together with a_-, behave as if $\kappa = 0$ in the limit $t \to t_0$ (as expected, due to their dynamical evolution being dominated by ρ, and not κ, at early times). In the case of $\kappa < 0$ the growing mode can be seen to decay as $\sim 1/|t - t_0|$ when $t \to \infty$, and the scale factor, a_-, behaves like an open Milne universe. For $\kappa > 0$ the scale factor initially grows, reaches a maximum of expansion, **and then collapses to zero in finite time, t.** As this future singularity is approached, both growing and decaying modes of φ **diverge to infinity.**

These solutions may serve as the basis for calculating the matter power spectrum. However, they will only remain so as long as the evolution equation for χ remains approximately satisfied.

4 The FLRW limit

From the perturbed LTB equations above it is not clear what each gauge invariant variable corresponds to in terms of the more familiar Bardeen potentials, and so forth, of standard cosmology. Here we derive the standard FLRW perturbation equations in the GMG formalism, and re-express the GS and GMG variables in terms of FLRW variables.

In the FLRW limit $\kappa \to$ constant, and we have that $a_\perp$ and $a_- \to a(t)$. The master equations in the polar sector (3.1)–(3.3) then become

$$\left[\partial_\tau^2 + 2\mathcal{H}\partial_\tau - \vec{\nabla}^2 + \frac{4(1-\kappa r^2)}{r}\partial_r - \frac{2}{r^2}\right]\chi = 0,$$

and

$$\left[\partial_\tau^2 + 3\mathcal{H}\partial_\tau - 2\kappa\right]\varphi = -\left[-\mathcal{H}\partial_\tau + \frac{(1-\kappa r^2)}{r}\partial_r + \frac{(\ell(\ell-1) - 2 + 4\kappa r^2)}{2r^2}\right]\chi,$$

and

$$\left[\partial_\tau + 2\mathcal{H}\right]\varsigma = \sqrt{1-\kappa r^2}\,\partial_r\chi,$$

while in the axial sector we have

$$\left[\partial_\tau^2 - 6\mathcal{H}\partial_\tau - \vec{\nabla}^2 - \frac{4(1-\kappa r^2)}{r}\left(\partial_r - \frac{3}{2r}\right) - 6\mathcal{H}^2\right]\mathrm{H} = 16\pi\rho\frac{\sqrt{1-\kappa r^2}}{ar^2}\partial_r\mathbb{V}, \tag{4.1}$$

and

$$\partial_\tau v = 0, \tag{4.2}$$

where $d\tau = dt/a$ is conformal time, and $\mathcal{H} \equiv a_{,\tau}/a$ is the conformal Hubble rate which obeys the Friedmann and Raychaudhuri equations

$$\mathcal{H}^2 = \frac{8\pi a^2\rho}{3} - \kappa \quad \text{and} \quad \partial_\tau\mathcal{H} = -\frac{1}{2}\left(\mathcal{H}^2 + \kappa\right). \tag{4.3}$$

Throughout this section $\vec{\nabla}^2$ will always refer to the Laplacian acting on a 3-scalar, so that

$$\vec{\nabla}^2 = (1-\kappa r^2)\partial_r^2 + \frac{(2-3\kappa r^2)}{r}\partial_r - \frac{\ell(\ell+1)}{r^2}.$$

It is evident from the equations above that χ is a gravitational wave, as its characteristics are null. However, χ can also be seen to act as a source for φ even though the homogeneous part of the evolution equation looks like very similar to the Bardeen equation. Similarly, ς looks like it almost obeys the vector decay law, but is also coupled to gravitational waves through χ. The fact that these variables do not decouple in the FLRW limit means that their interpretation in terms of FLRW gauge invariants will not be straightforward.

Let us now consider the perturbed FLRW line-element in the longitudinal, or conformal Newtonian, gauge:

$$\begin{aligned} \mathrm{d}s^2 = &-a^2(1+2\Phi)\mathrm{d}\tau^2 - 2a^2 V_i \mathrm{d}\tau \mathrm{d}x^i \\ &+ a^2[(1-2\Psi)\gamma_{ij} + h_{ij}]\mathrm{d}x^i \mathrm{d}x^j, \end{aligned} \tag{4.4}$$

where $a = a(\tau)$ is the scale factor, and $\gamma_{ij} = \mathrm{diag}[(1-\kappa r^2)^{-1}, r^2\gamma_{ab}]$ is the background spatial metric in spherical coordinates of curvature κ. $\vec{\nabla}_i$ is the covariant derivative with respect to γ_{ij}. The metric (4.4) is split in the standard way into two 3-scalars (Φ, Ψ), a 3-vector (V_i) and a 3-tensor (h_{ij}), where the '3' is not usually emphasised. All of these quantities are gauge invariant variables (see appendix D). The vector V_i is divergence-free, and the tensor h_{ij} is divergence and trace-free. Note that the coordinates used in the metric in the longitudinal gauge, given by eq. (4.1), and the metric in the RW gauge, eqs. (2.26) and (2.30), are not the same.

In appendix D we show that, in the FLRW limit, the LTB gauge invariants (φ, ς, χ, η, Π and $\bar{v}$) can be written in terms of the usual FLRW invariants (Φ, Ψ, V_i and h_{ij}) in the following way:

Polar:

$$\begin{aligned} \varphi = &-2\Psi - 2\mathcal{H}V - 2\frac{(1-\kappa r^2)}{r}h_r + \frac{1}{r^2}h^{(T)} \\ &- \left[-\mathcal{H}\partial_\tau + \frac{(1-\kappa r^2)}{r}\partial_r - \frac{\ell(\ell+1) - 4(1-\kappa r^2)}{2r^2}\right]h^{(TF)}, \end{aligned} \tag{4.5}$$

$$\varsigma = \sqrt{1-\kappa r^2}\left\{V_r - \partial_\tau V + \partial_r h_r - \left(\partial_r - \frac{1}{r}\right)\partial_\tau h^{(TF)}\right\}, \tag{4.6}$$

$$\begin{aligned} \chi = &(1-\kappa r^2)h_{rr} + 2\left[-(1-\kappa r^2)\partial_r + \frac{1}{r}\right]h_r - \frac{1}{r^2}h^{(T)} \\ &+ \left[(1-\kappa r^2)\partial_r^2 - \frac{(3-2\kappa r^2)}{r}\partial_r - \frac{\ell(\ell+1) - 8 + 4\kappa r^2}{2r^2}\right]h^{(TF)}, \end{aligned} \tag{4.7}$$

$$\begin{aligned} \eta - \Phi = &-\Psi - (\partial_\tau + 2\mathcal{H})V + \frac{1}{2}(1-\kappa r^2)h_{rr} + \left[-(1-\kappa r^2)\partial_r + \kappa r\right]h_r \\ &+ \frac{1}{2}\left[-\partial_\tau^2 + (1-\kappa r^2)\partial_r^2 - 2\mathcal{H}\partial_\tau - \frac{(2-\kappa r^2)}{r}\partial_r + \frac{2}{r^2}\right]h^{(TF)}. \end{aligned} \tag{4.8}$$

Axial:

$$\Pi = \frac{\sqrt{1-\kappa r^2}}{a^2 r^2}\left[\left(\partial_r - \frac{2}{r}\right)\bar{V} - \partial_r \bar{h}_r\right] \tag{4.9}$$

$$16\pi\rho a\bar{v} = \left[-\vec{\nabla}^2 + \frac{(2-4\kappa r^2)}{r}\partial_r - 4\kappa\right]\bar{V} \tag{4.10}$$

where, in order to compare with the GMG formalism, we have split the 3-vector V_i and the 3-tensor h_{ij} into their radial and angular parts, and then these into their polar and axial components, as described in appendix D. This makes explicit the mixing of SVT modes in the LTB gauge invariants. We have substituted eq. (D.10) to remove the tensor contribution to $\bar{v}$ in eq. (4.10).

4.1 Polar perturbations

As we are dealing with FLRW perturbations we may separate the scalar, vector and tensor parts of these equations, as we know they evolve independently.

4.1.1 Scalars

From $\eta = 0$ we have $\Phi = \Psi$, as is usual in a dust dominated FLRW cosmology. From the φ-equation we then find

$$\partial_\tau^2\Psi + 3\mathcal{H}\partial_\tau\Psi - 2\kappa\Psi = 0, \tag{4.11}$$

which is the usual Bardeen equation for the Newtonian potential. The ς- and χ-equations contain no scalar modes. We then note that the scalar part of the gauge invariant matter perturbations can be written

$$4\pi a^2\rho\Delta = \vec{\nabla}^2\Psi - 3\mathcal{H}\partial_\tau\Psi - 3(\mathcal{H}^2 - \kappa)\Psi, \tag{4.12}$$

$$4\pi a\rho v = -(\partial_\tau + \mathcal{H})\Psi, \tag{4.13}$$

$$4\pi a^2\rho w = -\sqrt{1-\kappa r^2}(\partial_\tau - \mathcal{H})\partial_r\Psi. \tag{4.14}$$

It can be seen from (4.12) that the scalar part of the energy density perturbation is just the gauge invariant density fluctuation $\delta\rho^{(s,i)} \equiv \delta\rho - \partial_\tau\rho(B - \partial_\tau E)$ [16]. However, we will see below that we cannot simply identify $\Delta = \delta\rho^{(s,i)}/\rho$, as Δ has non-zero vector and tensor parts.

4.1.2 Vectors

From $\eta = 0$, and the evolution equation for ς, we find that

$$\partial_\tau V = -2\mathcal{H}V \quad \text{and} \quad \partial_\tau V_r = -2\mathcal{H}V_r. \tag{4.15}$$

Thus, these two equations give the usual a^{-2} law for vector modes. The vector part of the evolution equation for φ automatically follows from these two, while the χ-equation contains no vectors. The vector parts of the gauge invariant matter perturbations are then given by

$$\Delta = 3\mathcal{H}V \tag{4.16}$$

$$16\pi a\rho v = \left[(1-\kappa r^2)\partial_r - \kappa r\right]V, \\ -\left[(1-\kappa r^2)\partial_r^2 - \kappa r\partial_r - 2(3\mathcal{H}^2 + \kappa)\right]V, \tag{4.17}$$

$$16\pi a^2\rho\, w = \sqrt{1-\kappa r^2}\left\{ -\frac{\ell(\ell+1)}{r^2} + 3\mathcal{H}^2 \quad \kappa\right] V_r + \left[\frac{\ell(\ell+1)}{r^2} - 3(\mathcal{H}^2+\kappa)\right]\partial_r V\right\}. \tag{4.18}$$

It is a curiosity that the vector part of $\Delta - 3\mathcal{H}V$ is non-zero, so that while Δ looks like it is just a gauge invariant density perturbation, it actually contains vectors.

4.1.3 Tensors

The GMG formalism is rather less tidy when trying to describe 3-tensor modes. The equation which looks like it should be describing gravitational waves is that for χ. But while this equation consists only of tensor modes, it is in a very ugly form when evaluated in terms of the FLRW perturbed metric, as the χ equation contains fourth derivatives of $h^{(TF)}$. In fact, as all four GMG variables contain 3-tensors, all four field equations contain tensor modes, and showing that they reduce to the usual FLRW wave equation for tensors is non-trivial. The four equations form a set of coupled PDEs for the variables $h_{rr}, h_r, h^{(T)}, h^{(TF)}$, the simplest of which may be read off from $\eta = 0$ above. Recall, however, that there is only one degree of freedom in the polar part of h_{ij}, with the trace and divergence free conditions removing the other three. If we choose this degree of freedom to be $h^{(T)}$ then it can be shown from the GMG equations for η, φ and ς, when combined with the conditions given by eqs. (D.7), (D.8) and (D.9), reduce to the single master equation

$$[\partial_\tau^2 + 2\mathcal{H}\partial_\tau - \vec{\nabla}^2]\, h^{(T)} = 0, \tag{4.19}$$

which is just the trace of the usual FLRW wave equation. The χ equation then follows automatically.

The tensor parts of the variables associated with the fluid can then be written

$$\Delta = \frac{3}{2}\mathcal{H}\partial_\tau h^{(TF)}, \tag{4.20}$$

$$v = \frac{1}{2}a\partial_\tau h^{(TF)}, \tag{4.21}$$

$$w = \frac{1}{2}\sqrt{1-\kappa r^2}\left(\partial_\tau h_r + \frac{1}{r}\partial_\tau h^{(TF)}\right). \tag{4.22}$$

4.2 Axial perturbations

There are no scalar modes in the axial sector.

For vector modes it can be seen from $\partial_\tau \tilde{v} = 0$, and the radial equation of (3.12), that the usual vector decay law, $\partial_\tau \tilde{V} = -2\mathcal{H}\tilde{V}$, is obeyed. The Π-equation is then automatically satisfied.

Combining the radial equation of (3.12) and eq. (D.10), we find the wave equation

$$[\partial_\tau^2 + 2\mathcal{H}\partial_\tau \quad \vec{\nabla}^2 + 2\kappa r\partial_r + 3\kappa]\, h_r = 0, \tag{4.23}$$

where the extra curvature terms are due to $\vec{\nabla}^2$ acting here on a scalar that is actually part of a 3-tensor. The equation for Π then follows.

4.3 SVT variables

We have found that what appear as gauge invariant fluid perturbations in the GMG formalism – namely Δ, v and w – are not exclusively fluid modes, as they are usually understood in FLRW cosmology, as they can be excited by tensors (FLRW models need a tensor part in the anisotropic stress for fluid perturbations to couple to tensor modes, which we have not included here). It is also the case that the GMG metric perturbations do not correspond in a straightforward way to the SVT decomposition we are familiar with from FLRW cosmology. For example, it is clear that χ represents gravitational waves, and in the FLRW limit it is a pure tensor mode: but what about scalars and vectors? Can we identify combinations of gauge invariant GMG variables which will represent purely scalar or vector modes in the FLRW limit, and so be useful physical variables in LTB cosmology?

In order to find these, let us first note that the combination

$$\lambda = 8\pi a^2 \mathcal{H}^{-1}\rho\left[\Delta \quad 3\frac{\mathcal{H}}{a}v\right] \tag{4.24}$$

does not contain any tensor modes in the FLRW limit (as can be verified from eqs. (4.20) and (4.21)). Also, note that we can construct from ς and χ a quantity that contains only vector modes:

$$\begin{aligned}\xi &= \frac{3r}{2\sqrt{1-\kappa r^2}}\left[\vec{\nabla}^2 + 3\kappa\right]r^{-1}\varsigma - \frac{3}{2r^3}\partial_r\left(r^2\partial_\tau\chi\right)\\ &= \frac{3}{2}\left[\vec{\nabla}^2 - 3\kappa - \frac{2}{r}\partial_r\right]\left(V_r - \partial_r V\right).\end{aligned} \tag{4.25}$$

From λ and ξ we can now construct a variable that is a function of scalar modes only:

$$\begin{aligned}\zeta \equiv\ & a^{-2}\vec{\nabla}^2\lambda - a^{-2}\left[(1-\kappa r^2)\partial_r + \frac{2-3\kappa r^2}{r}\right]\xi\\ & - \frac{2}{a^2\mathcal{H}}\left[\vec{\nabla}^2 - 3\kappa\right]\vec{\nabla}^2\Psi.\end{aligned} \tag{4.26}$$

This is related to the gauge invariant density fluctuation $\delta\rho^{(GI)}$ and the curvature perturbation, $\mathcal{R} = \Psi - \mathcal{H}(\mathcal{H}\Phi - \partial_\tau\Psi)/(\partial_\tau\mathcal{H} - \mathcal{H}^2 - \kappa)$ [17], by

$$\frac{7\ell\zeta}{8\pi\rho} = \vec{\nabla}^2\left[\frac{\delta\rho^{(GI)}}{\rho} + 3\mathcal{R} - 3\Psi\right]. \tag{4.27}$$

For the axial perturbations we already see that $\bar{v}$ is a pure vector mode, but that Π is an awkward mixture of vectors and tensors. Defining the variable

$$\begin{aligned}\Upsilon =\ & a^{-2}\left[\vec{\nabla}^2 - \frac{4(1-\kappa r^2)}{r}\partial_r + \frac{2(3-4\kappa r^2)}{r^2}\right]\Pi\\ & - 16\pi\rho\frac{\sqrt{1-\kappa r^2}}{a^3 r^2}\partial_r\bar{v} \qquad (4.28)\\ =\ & \frac{\sqrt{1-\kappa r^2}}{a^4 r^2}\left[\vec{\nabla}^2 - 2\kappa r\partial_r - \kappa\right]\partial_\eta\bar{h}, \qquad (4.29)\end{aligned}$$

we are able to define a pure tensor mode using the GMG gauge invariant variables.

Using these new variables, we can now generalise to the inhomogeneous case. The resulting functions will have the useful feature that they reduce to pure scalar or vector modes in the FLRW limit. An example set of variables is given by eqs. (2.34)–(2.39), in section 2.3.1. These reduce to the quantities above in the FLRW limit. The variables $\hat{\zeta}$, $\hat{\boldsymbol{\xi}}$, $\hat{v}$, $\hat{\chi}$ and $\hat{\Upsilon}$, are then useful gauge invariant variables in the LTB perturbation equations as they encode generalised scalar, vector and tensor perturbations, respectively, as they are normally referred to in cosmology.

5 Discussion

We have presented here a full system of master equations that represent the general perturbations to LTB space-times, in terms of the gauge invariant variables $\varphi, \varsigma, \chi, \Pi, \bar{v}$ (and η, strictly speaking). This formalism can now be used to investigate, in a fully consistent fashion, the growth of linear structure in LTB models. As such, predictions for phenomena such as baryon acoustic oscillations, the integrated Sachs-Wolfe effect, and the observed matter power spectrum can now be made, and used to compare with astrophysical data. This will allow us to establish what deviations should be expected from the usual FLRW predictions, and whether or not such deviations can be observed in our Universe.

However, while $\varphi, \varsigma, \chi, \Pi, \bar{v}$ and η appear completely naturally, and produce an elegant system of equations in the form of an initial value formulation, they do not reduce to anything intuitive in the FLRW limit. Instead, they are a cumbersome mixture of scalar, vector and tensor perturbations – a situation made worse still by the additional couplings that exist in the evolution equations in the more general, inhomogeneous case.

To address these problems we have defined a new set of variables in the polar sector, $\hat{\zeta}$, $\hat{\boldsymbol{\xi}}$ and $\hat{\chi}$, that can be thought of as generalised scalar, vector and tensor perturbations, respectively. Similarly, we propose new variables in the axial sector, $\hat{v}$ and $\hat{\Upsilon}$, that correspond to generalised vector and tensor modes. In the FLRW limit these new variables become pure scalars, vectors and tensors. We expect these new variables to prove useful in future studies where they can be used to set the initial conditions for the evolution of perturbations. For example, in an LTB model with homogeneous bang time, $t_{\rm b}(r) =$constant, the surfaces of constant t will be almost homogeneous at early times, and will then be well approximated by an FLRW description. The new variables can then be used to match the FLRW initial conditions onto the LTB evolution equations in a straightforward way. This will be considered further in future studies.

Acknowledgments

We are grateful to Pedro G. Ferreira and Roy Maartens for helpful discussions and comments. TC acknowledges the support of Jesus College and the BIPAC. CC acknowledges funding from the National Research Foundation (South Africa) and the University of Cape Town. SF is funded by the National Astrophysics and Space Science Programme (South Africa) and the NRF. CC would like to thank the Department of Astrophysics at the University of Oxford for hospitality while some of the work presented here was undertaken. This visit was partly supported by a joint Royal Society (UK) - NRF grant UID 65329.

A The Gerlach-Sengupta formalism

The general form of perturbations to the metric and stress-energy tensors can be written, in terms of the harmonic functions outlined in section 2, as $g_{\mu\nu} \to g_{\mu\nu} + \Delta g_{\mu\nu}$ and $T_{\mu\nu} \to T_{\mu\nu} + \Delta T_{\mu\nu}$, where [11]

$$\Delta g_{\mu\nu} \equiv \begin{pmatrix} 0 & h_1^{\rm axial}\bar{Y}_a \\ h_1^{\rm axial}\bar{Y}_a & h\,\bar{Y}_{ab} \end{pmatrix} \tag{A.1}$$

$$\Delta T_{\mu\nu} \equiv \begin{pmatrix} 0 & \Delta t_A^{\rm axial}\bar{Y}_a \\ \Delta t_A^{\rm axial}\bar{Y}_a & \Delta t^{(1)}\,\bar{Y}_{ab} \end{pmatrix}. \tag{A.2}$$

for axial perturbations, and

$$\Delta g_{\mu\nu} \equiv \begin{pmatrix} h_{AB}Y & h_A^{\rm polar}Y_a \\ h_A^{\rm polar}Y_a & a^2 r^2(KY\gamma_{ab} + GY_{ab}) \end{pmatrix} \tag{A.3}$$

$$\Delta T_{\mu\nu} \equiv \begin{pmatrix} \Delta t_{AB}Y & \Delta t_A^{\rm polar}Y_a \\ \Delta t_A^{\rm polar}Y_a & \Delta t^{(2)}Y_{ab} + a^2 r^2 \Delta t^{(3)}Y\gamma_{ab} \end{pmatrix}. \tag{A.4}$$

for polar perturbations. The new variables $h_A^{\rm axial}$, h, $\Delta t_A^{\rm axial}$, $\Delta t^{(1)}$, h_{AB}, $h_A^{\rm polar}$, K, G, Δt_{AB}, $\Delta t_A^{\rm polar}$, $\Delta t^{(2)}$ and $\Delta t^{(3)}$ are all functions of the two coordinates x^A.

From these quantities we can then construct the gauge invariant variable [11]

$$k_A \equiv h_A^{\rm axial} - h_{|A} + 2h w_A, \tag{A.5}$$

for axial perturbations, and

$$k_{AB} \equiv h_{AB} - p_{A|B} - p_{B|A} \tag{A.6}$$

$$\kappa \equiv K - 2w^A p_A \tag{A.7}$$

$$t_{AB} \equiv \Delta t_{AB} - t_{ABC}p^C - t_{AC}p^C{}_{|B} - t_{BC}p^C{}_{|A} \tag{A.8}$$

$$t_A \equiv \Delta t_A^{\rm polar} - t_{AC}p^C, \tag{A.9}$$

for scalar perturbations. The quantities $\Delta t_A^{\rm axial}$, $\Delta t^{(1)}$, $\Delta t^{(2)}$ and $\Delta t^{(3)}$ are already gauge invariant for a dust dominated universe. Here a pipe indicates a covariant derivative with respect to the metric on M^2, and we have defined $p_A \equiv h_A^{\rm polar} - a^2 r^2 G_{|A}/2$, along with GS, for concision. All of these expressions are constructed so as to be invariant under infinitesimal coordinate transformations of the form $x^\mu \to x^\mu + \xi^\mu$.

There exists here a useful gauge in which $h = h_A^{\rm polar} = G = 0$. This is the Regge-Wheeler gauge [15], where the remaining perturbation variables are all equal to gauge invariant quantities, as can be seen from the expressions above.

B The Gundlach-Martín-García formalism

The background quantities used by GMG can be written in the LTB case, using our notation, as

$$U = H_- \tag{B.1}$$

$$V = \frac{H_\perp}{W} \tag{B.2}$$

$$m = \frac{M}{2} \tag{B.3}$$

$$\mu = \tilde{H}_\parallel \tag{B.4}$$

$$\nu = 0. \tag{B.5}$$

GMG then write their perturbed fluid four velocity as $u_\mu \to u_\mu + \Delta u_\mu$, where

$$\Delta u_\mu = (0, \tilde{v}\, Y_{,\theta}) \tag{B.6}$$

for axial perturbations, and

$$\Delta u_\mu = \left[\left(\tilde{w} n_A + \frac{1}{2} h_{AB} u^B\right) Y, \tilde{v}\, Y_{,\theta}\right] \tag{B.7}$$

for scalar perturbations. Here $n_A \equiv -\epsilon_{AB} u^B$ is a unit space-like vector, and $\tilde{v}$, $\tilde{v}$ and $\tilde{w}$ are all functions of x^A. Density perturbations are then parametrised by $\rho \to \rho + \tilde{\Delta} Y \rho$, and the following gauge invariant quantities can be constructed:

$$v \equiv \tilde{v} - p^{/t} u_B \tag{B.8}$$

$$w \equiv \tilde{w} - n^A u_{A|B} p^B + \frac{1}{2} n^A u^B (p_{A|B} - p_{B|A}) \tag{B.9}$$

$$\Delta \equiv \tilde{\Delta} - p^A (\ln \rho)_{|A} \tag{B.10}$$

with $\tilde{v}$ already gauge invariant. Again, the Regge-Wheeler gauge can be seen to have a special significance. The gauge invariants above can be related to those in appendix A via

$$L_A = \tilde{v} u_A \tag{B.11}$$

$$t_A = v \rho u_A \tag{B.12}$$

$$t_{AB} = \rho \Big[w (u_A n_B + n_A u_B) + \Delta u_A u_B \tag{B.13}$$

$$- \frac{1}{2} (k_{AC} u_B + u_A k_{BC}) \Big] \tag{B.14}$$

together with $L = t^{(2)} = t^{(3)} = 0$. GMG then continue to decompose k_{AB} into the 'fluid frame' via

$$k_{AB} \equiv \eta (n_A n_B - u_A u_B) + \phi (n_A n_B + u_A u_B) \tag{B.15}$$

$$+ \varsigma (u_A n_B + n_A u_B), \tag{B.16}$$

and to define the new variable

$$\chi \equiv \phi - \varphi + \eta. \tag{B.17}$$

In these variables the perturbation equations take a particularly simple form [8].

C Polar $\ell = 0, 1$ perturbations

For polar perturbations with $\ell = 0, 1$ it is no longer the case that the field equations give $\eta = 0$. The general system of equations given in section 3.1 now reads:

For $\ell \geq 1$:

$$-\ddot{\chi} + \chi'' + 2(H_\parallel - H_\perp)\zeta' - 2\eta'' = -2\left[8\pi\rho - \frac{3M}{a_-^3} - 2H_\perp(H_\parallel - H_\perp)\right](\chi+\varphi) \tag{C.1}$$
$$+\frac{(\ell-1)(\ell+2)}{a_-^2 r^2}\chi + 3H_\parallel\dot{\chi} + 4(H_\parallel - H_\perp)\dot{\varphi} + 2W\chi'$$
$$-2\left[H' - 2(H_\parallel - H_\perp)W\right]\zeta - 2(H_\parallel - H_\perp)\dot{\eta} - 6W\eta'$$
$$-\left[\frac{\ell(\ell+1)+8}{a_\perp^2 r^2} + 8H_\parallel H_\perp + 4H_\perp^2 - 16W^2 - 32\pi\rho\right]\eta,$$

$$-\ddot{\varphi} - 4H_\perp\dot{\varphi} + \left[2W^2 - \frac{\ell(\ell+1)-2}{2a_-^2 r^2}\right](\chi - 2\eta) \tag{C.2}$$
$$-2W(H_\parallel - H_\perp)\zeta + H_-(\dot{\chi} - 2\dot{\eta}) - W(\chi'$$
$$-2\eta') - 2W^2\eta - 2\left(\frac{1}{a_\perp^2 r^2} - W^2\right)\varphi,$$

$$-\dot{\zeta} - 2H_\perp\zeta + \chi' + 2W\eta - 2\eta', \tag{C.3}$$

$$8\pi\rho v - \frac{\zeta'}{2} + H_\parallel(\chi - \varphi) + \frac{\dot{\chi}}{2} + \dot{\varphi} \quad (H_- + H_\perp)\eta, \tag{C.4}$$

$$\dot{v} - \frac{\chi}{2} + \frac{\varphi}{2} - \eta, \tag{C.5}$$

and for $\ell \geq 0$:

$$8\pi\rho w - (\dot{\varphi})' - W\dot{\chi} - H_-\chi' - (H_\parallel - 2H_-)\varphi' - 2H_-\eta' \tag{C.6}$$
$$+\left[\frac{\ell(\ell+1)-2}{2a_-^2 r^2} + H_\perp^2 + 2H_\perp H_\parallel - W^2 - 4\pi\rho\right]\zeta,$$

$$8\pi\rho\Delta = \left[\frac{\ell(\ell+1)}{a_-^2 r^2} + 2H_-^2 + 4H_\parallel H_\perp - 8\pi\rho\right](\chi+\varphi) + 2H_\perp\zeta' \tag{C.7}$$
$$\frac{(\ell-1)(\ell+2)}{2a_-^2 r^2}\chi + 2(H_\parallel + H_\perp)W\zeta - H_-\dot{\chi} - \varphi'' + (H_\parallel + 2H_\perp)\dot{\varphi}$$
$$-W\chi' - 2W\varphi' - 2H_-(H_\perp + 2H_-)\eta,$$

$$\dot{w} - \frac{\varphi'}{2} - H_-w - \frac{H_\parallel}{2}\zeta - W\eta, \tag{C.8}$$

$$\dot{\Delta} + \left(w + \frac{\zeta}{2}\right)' - \frac{\ell(\ell-1)}{a_\perp^2 r^2}v - \left(w - \frac{\zeta}{2}\right)\frac{\rho'}{\rho} - \frac{\dot{\chi}}{2} - \frac{3\dot{\varphi}}{2} - 2W\left(w + \frac{\zeta}{2}\right). \tag{C.9}$$

C.1 $\ell = 1$

For $\ell = 1$ there is an additional gauge freedom which can be used to eliminate one of the perturbation variables. The obvious choice may be to use this to set $\eta = 0$, but GMC showed this to lead to some ambiguity. We therefore follow them in using the less ambiguous choice $\varphi = 0$. The evolution and conservations equations above can then be combined to give

$$W\eta' - H_\perp\dot{\eta} = 4\pi\rho\Delta - 16\pi\rho H_\perp v - \left(\frac{2}{a_-^2 r^2} - 3W^2 + H^2\right)\eta \tag{C.10}$$
$$-\left[W^2 - H_\perp^2 - 4\pi\rho\right]\chi - 2H_-W\zeta,$$

$$W\chi' - H_-\dot{\chi} = 8\pi\rho\Delta - 32\pi\rho H_\perp v - \left[\frac{2}{a_-^2 r^2} + 2H_\perp^2 - 8\pi\rho\right]\chi \qquad \text{(C.11)}$$
$$-2(H_\parallel + H_-)W\varsigma - 2H_-^2\eta,$$
$$W\varsigma' - H_-\dot{\varsigma} = 8\pi\rho(w - 2Wv) + 2H_\parallel W(\eta - \chi) + 4H_- W\eta$$
$$- \left[H_\perp^2 - W^2 + \frac{2}{a_-^2 r^2} - 4\pi\rho\right]\varsigma. \qquad \text{(C.12)}$$

These are the LTB equivalents of (GMGA12), (GMGA13) and (GMGA14) from [8]. These three equations can be solved, along with the three conservation equations (3.8) (3.10), with $\varphi = 0$, for the six remaining perturbation variables, η, χ, ς, v, w and Δ.

C.2 $\ell = 0$

Polar perturbations with $\ell = 0$ are spherical. As such one could conceive of absorbing such perturbations into the background parameters, which themselves describe the most general spherically symmetric dust dominated solution of Einstein's equations. Despite this being the case, it still seems worth considering $\ell = 0$ perturbations in a spherical background, as one can then separate them out more easily from a smooth background.

In this case we again have a non-zero η, but now have sufficient gauge freedom to set $\varphi = 0$ and

$$\varsigma = \frac{2H_- W}{H_\perp^2 - W^2}(\eta - \chi), \qquad \text{(C.13)}$$

as done by GMG. The constraint equations then give

$$W\eta' - H_\perp\dot{\eta} - 4\pi\rho\left(\chi - \frac{2H_\perp^2}{(W^2 - H_\perp^2)}\eta\right) + 16\pi\rho\frac{H_- W}{(W^2 - H_\perp^2)}w \qquad \text{(C.14)}$$
$$-4\pi\rho\frac{(W^2 - H_\perp^2)}{(W^2 - H_\perp^2)}\Delta,$$

and

$$W\chi' - H_\perp\dot{\chi} = \frac{3H_\perp W}{(H_-^2 - W^2)}\left[H_\perp W + 4\pi\rho\frac{H_\perp W}{(W^2 - H_\perp^2)}\right](\chi - \eta) + 16\pi\rho\frac{H_- W}{(W^2 - H_\perp^2)}w \qquad \text{(C.15)}$$
$$+8\pi\rho\frac{(W^2 + H_\perp^2)}{(W^2 - H_-^2)}\Delta + \left(8\pi\rho - \frac{1}{a_-^2 r^2}\right)\left(\chi + \frac{2H_-^2}{(W^2 - H_\perp^2)}\eta\right).$$

These are the LTB versions of (GMGA18) and (GMGA19). The two remaining conservation equations are then

$$\dot{w} - \left[H_\parallel - 4\pi\rho\frac{H_\perp}{(W^2 - H_\perp^2)}\right]w - \frac{W}{2a_-^2 r^2(W^2 - H_-^2)}\eta \qquad \text{(C.16)}$$
$$+(\eta - \chi)\left[\frac{W(W^2 - H_\perp^2)}{2(W^2 + H_\perp^2)} - \frac{H_\perp H_\perp W}{(W^2 + H_\perp^2)} - 4\pi\rho\frac{WH_\perp^2}{(H_\perp^2 - W^2)}\right],$$

and

$$\dot{\Delta} + w' = \frac{4\pi\rho H_\perp}{(W^2 - H_\perp^2)}\Delta - \frac{H_-}{(W^2 - H_\perp^2)}\left(\frac{1}{2a_-^2 r^2} - 4\pi\rho\right)\eta \qquad \text{(C.17)}$$

$$-\left[\frac{\rho'}{\rho}+2W-4\pi\rho\frac{W}{(W^2-H_-^2)}\right]w$$
$$-(\eta-\chi)\left[\frac{H_\perp W}{(W^2+H_-^2)}\frac{\rho'}{\rho}+H_-+H_\parallel-\frac{H_\perp(W^2-H_\perp^2)}{2(W^2+H_-^2)}+4\pi\rho\frac{H_\perp W^2}{(W^4-H_\perp^4)}\right].$$

These equations are the LTB versions of (GMGA15) and (GMGA16). We now have four equations to solve for the four remaining variables η, χ, w and Δ.

D Matching LTB and FLRW gauge invariants

Here we derive the standard FLRW perturbation equations in the GMG formalism. Unfortunately, the RW gauge is not well adapted to our usual description of FLRW perturbations. We must therefore write both the GMG variables and the perturbed FLRW metric in a general gauge.

In general coordinates an arbitrary perturbation of FLRW can be written

$$\begin{aligned}ds^2 &= -a^2(1+2\phi)d\tau^2+2a^2(\vec\nabla_i B-S_i)d\tau dx^i\\ &\quad+a^2\left[(1-2\psi)\gamma_{ij}+2\vec\nabla_i\vec\nabla_j E+2\vec\nabla_{(i}F_{j)}+h_{ij}\right]dx^i dx^j,\end{aligned}\tag{D.1}$$

where $a=a(\tau)$, γ_{ij} is the spatial metric, and $\vec\nabla_i$ is the covariant derivative with respect to γ_{ij}. The vectors here are divergence free, $\vec\nabla_i S^i=0$, and the tensors are divergence and trace-free. Gauge invariant metric perturbations are given by

$$\begin{aligned}\Phi &= \phi+\mathcal{H}(B-\partial_\tau E)+\partial_\tau(B-\partial_\tau E),\\ \Psi &= \psi-\mathcal{H}(B-\partial_\tau E),\\ V_i &= S_i+\partial_\tau F_i,\end{aligned}\tag{D.2}$$

and the perturbations h_{ij} are already gauge-invariant.

To compare with the GMG formalism, we expand this 1+3 split into a 1+1+2 split in spherical coordinates, peeling off the radial parts of each variable. A 3-vector, such as S_i, then splits into a scalar, S_r, and a 2-vector, S_a. These can then be decomposed into spherical harmonics as

$$\begin{aligned}S_i &= \sum_{\ell m} S_r^{(\ell m)}Y^{(\ell m)}-S_r Y,\\ S_a &= \sum_{\ell m} S^{(\ell m)}Y_a^{(\ell m)}+\bar S^{(\ell m)}\epsilon_a{}^b Y_b^{(\ell m)},\\ &\quad -SY_a-\bar S\bar Y_a,\end{aligned}\tag{D.3}$$

where S and $\bar S$ are the polar and axial parts of S, respectively. The divergence-free property of the 3-vector, $\vec\nabla_i S^i=0$, then gives us that

$$(1-\kappa r^2)\partial_r S_r+\frac{(2-3\kappa r^2)}{r}S_r-\frac{\ell(\ell+1)}{r^2}S=0.\tag{D.4}$$

This reduces the degrees of freedom in the 3-vector to two: one polar and one axial.

For a 3-tensor, the split into radial and angular parts is a bit more messy. The tensor

$$h_{ij}=\left(\begin{array}{c|c}h_{rr} & h_{ra}\\ \hline h_{ra} & h_{ab}\end{array}\right)\tag{D.5}$$

splits into a 2-scalar $h_{rr} = h_{rr}^{(\ell m)} Y^{(\ell m)}$ (spherical harmonic sum implied), a 2-vector $h_{ra} = h_v^{(\ell m)} Y_a^{(\ell m)} + \bar{h}_v^{(\ell m)} \bar{Y}_a^{(\ell m)}$ and a remaining part consisting of a 2-scalar (the trace) and polar and axial trace-free 2-tensors:

$$h_{ab} = h^{(T)} \gamma_{ab} Y + h^{(TF)} Y_{ab} + \bar{h} \bar{Y}_{ab}. \tag{D.6}$$

This splits the 3-tensor h_{ij} into its polar (h_{rr}, h_r, $h^{(T)}$ and $h^{(TF)}$) and axial ($\bar{h}_r$ and $\bar{h}$) parts.

The trace-free, $\gamma^{ij} h_{ij} = 0$, and divergence-free, $\bar{\nabla}^i h_{ji} = 0$, conditions give:

$$0 = (1 - \kappa r^2) h_{rr} + \frac{2}{r^2} h^{(T)}, \tag{D.7}$$

$$0 = (1 - \kappa r^2) \partial_r h_{rr} + \frac{(2 - 4\kappa r^2)}{r} h_{rr} - \frac{2}{r^3} h^{(T)} - \frac{\ell(\ell-1)}{r^2} h_{rr}, \tag{D.8}$$

$$0 = (1 - \kappa r^2) \partial_r h_r + \frac{(2 - 3\kappa r^2)}{r} h_r + \frac{1}{r^2} h^{(T)} - \frac{(\ell-1)(\ell+2)}{2r^2} h^{(TF)}, \tag{D.9}$$

$$0 = (1 - \kappa r^2) \partial_r \bar{h}_r + \frac{(2 - 3\kappa r^2)}{r} \bar{h}_r - \frac{(\ell-1)(\ell+2)}{2r^2} \bar{h}. \tag{D.10}$$

Again, the degrees of freedom left after applying these relations is two: one per parity.

We can now equate the perturbed FLRW with the perturbed LTB metric, in an arbitrary gauge, to find that the polar perturbations are related by

$$a^{-2} h_{\tau\tau}^{GMG} = -2\phi, \tag{D.11}$$

$$a^{-2} h_{\tau r}^{GMG} = \frac{2}{1 - \kappa r^2} \psi + 2 \left(\partial_r - \frac{\kappa r}{1 - \kappa r^2} \right) \partial_\tau E + 2 \left(\partial_r - \frac{\kappa r}{1 - \kappa r^2} \right) F_r + h_{r\tau}, \tag{D.12}$$

$$a^{-2} h_{r\tau}^{GMG} = -S_r + \partial_r B_r \tag{D.13}$$

$$a^{-2} h_r^{GMG} = -S + B, \tag{D.14}$$

$$a^{-2} h_r^{GMG} = 2 \left(\partial_r - \frac{1}{r} \right) E + F_r - \left(\partial_r - \frac{2}{r} \right) F - h_{rr}, \tag{D.15}$$

$$r^2 G = 2E - 2F + h^{(TF)}, \tag{D.16}$$

$$K = -2\psi + 2 \frac{1 - \kappa r^2}{r} \partial_r E - 2 \frac{1 - \kappa r^2}{r} F_r + \frac{1}{r^2} h^{(T)} - \frac{\ell(\ell-1)}{2r^2} h^{(TF)}, \tag{D.17}$$

where everything has been decomposed into spherical harmonics, so that $\phi = \phi^{(\ell m)}(x^A)$ etc. For the axial modes we have

$$a^{-2} h_\tau^{GMG} = -\bar{S}, \tag{D.18}$$

$$a^{-2} h_r^{GMG} = \left(\partial_r - \frac{2}{r} \right) \bar{F} + \bar{h}_r, \tag{D.19}$$

$$a^{-2} h^{GMG} = \bar{F} - \frac{1}{2} \bar{h}. \tag{D.20}$$

The gauge invariant GMG variables can now be calculated directly, and are given in section 4.

References

[1] **G. Lemaître**, *The expanding universe*, *Ann. Soc. Sci. Brussels* **A53** (1933) 51 [*Gen. Rel. Grav.* **29** (1997) 641] [SPIRES].

R.C. Tolman, *Effect of inhomogeneity on cosmological models*, *Proc. Nat. Acad. Sci. U.S.A.* **20** (1934) 169;
H. Bondi, *Spherically symmetrical models in general relativity*, *Mon. Not. Roy. Astron. Soc.* **107** (1947) 410 [SPIRES].

[2] R. Maartens and D.R. Matravers, *Isotropic and semi-isotropic observations in cosmology*, *Class. Quant. Grav.* **11** (1994) 2693.

[3] H. Bondi, *Cosmology*, Cambridge University Press, Cambridge U.K. (1952).

[4] N. Mustapha, C. Hellaby and G.F.R. Ellis, *Large scale inhomogeneity versus source evolution: can we distinguish them observationally?*, *Mon. Not. Roy. Astron. Soc.* **292** (1997) 817 [gr-qc/9808079] [SPIRES];
M.-N. Celerier and J. Schneider, *A solution to the horizon problem: a delayed big bang singularity*, *Phys. Lett.* **A 249** (1998) 37 [astro-ph/9809134] [SPIRES];
M. Joyce et al., *Fractal cosmology in an open universe*, *Europhys. Lett.* **50** (2000) 416 [astro-ph/0002504] [SPIRES];
H. Alnes, M. Amarzguioui and O. Gron, *An inhomogeneous alternative to dark energy?*, *Phys. Rev.* **D 73** (2006) 083519 [astro-ph/0512006] [SPIRES];
R.R. Caldwell and A. Stebbins, *A test of the copernican principle*, *Phys. Rev. Lett.* **100** (2008) 191302 [arXiv:0711.3459] [SPIRES];
S. Alexander, T. Biswas, A. Notari and D. Vaid, *Local void vs dark energy: confrontation with WMAP and type Ia supernovae*, arXiv:0712.0370 [SPIRES];
J. Garcia-Bellido and T. Haugboelle, *Confronting Lemaître-Tolman-Bondi models with observational cosmology*, *JCAP* **04** (2008) 003 [arXiv:0802.1523] [SPIRES];
J.P. Zibin, *Scalar perturbations on Lemaître-Tolman-Bondi spacetimes*, *Phys. Rev.* **D 78** (2008) 043504 [arXiv:0804.1787] [SPIRES];
J. Garcia-Bellido and T. Haugboelle, *Looking the void in the eyes — the kSZ effect in LTB models*, *JCAP* **09** (2008) 016 [arXiv:0807.1326] [SPIRES];
K. Bolejko and J.S.B. Wyithe, *Testing the copernican principle via cosmological observations*, *JCAP* **02** (2009) 020 [arXiv:0807.2891] [SPIRES];
T. Clifton, P.G. Ferreira and K. Land, *Living in a void: testing the copernican principle with distant supernovae*, *Phys. Rev. Lett.* **101** (2008) 131302 [arXiv:0807.1443] [SPIRES];
J.P. Zibin, A. Moss and D. Scott, *Can we avoid dark energy?*, *Phys. Rev. Lett.* **101** (2008) 251303 [arXiv:0809.3761] [SPIRES];
J. Garcia-Bellido and T. Haugboelle, *The radial BAO scale and cosmic shear, a new observable for inhomogeneous cosmologies*, arXiv:0810.4939 [SPIRES];
T. Clifton, P.G. Ferreira and J. Zuntz, *What the small angle CMB really tells us about the curvature of the Universe*, arXiv:0902.1313 [SPIRES];
K. Tomita and K.T. Inoue, *Probing violation of the Copernican principle via the integrated Sachs-Wolfe effect*, arXiv:0903.1541 [SPIRES];
K. Tomita, *Bulk flows and cosmic microwave background dipole anisotropy in cosmological void models*, *Astrophys. J.* **529** (2000) 26 [astro-ph/9905278] [SPIRES]; *Distances and lensing in cosmological void models*, *Astrophys. J.* **529** (2000) 38 [astro-ph/9906027] [SPIRES].

[5] J.-P. Uzan, C. Clarkson and G.F.R. Ellis, *Time drift of cosmological redshifts as a test of the Copernican principle*, *Phys. Rev. Lett.* **100** (2008) 191303 [arXiv:0801.0068] [SPIRES];
C. Clarkson, B. Bassett and T.H.-C. Lu, *A general test of the Copernican principle*, *Phys. Rev. Lett.* **101** (2008) 011301 [arXiv:0712.3457] [SPIRES];
J. Jia and H. Zhang, *Can the Copernican principle be tested using the cosmic neutrino background?*, *JCAP* **12** (2008) 002 [arXiv:0809.2597] [SPIRES].

[6] K.S. Thorne and A. Campolattaro, *Non-radial pulsation of general-relativistic stellar models. I. Analytic analysis for $L \geq 2$*, *Astrophys. J.* **149** (1967) 591 (*Erratum ibid.* **152** (1967) 673);
R. Price and K.S. Thorne, *Non-radial pulsation of general-relativistic stellar models. II. Properties of the gravitational waves*, *Astrophys. J.* **155** (1969) 163.

K.S. Thorne, *Nonradial pulsation of general-relativistic stellar models. III. Analytic and numerical results for neutron stars*, *Astrophys. J.* **158** (1969) 1; *Nonradial pulsation of general-relativistic stellar models. IV. The weakfield limit*, *Astrophys. J.* **158** (1969) 997;
A. Campolattaro and K.S. Thorne, *Nonradial pulsation of general-relativistic stellar models. V. Analytic analysis for $L = 1$*, *Astrophys. J.* **159** (1970) 847;
J.R. Ipser and K.S. Thorne, *Nonradial pulsation of general-relativistic stellar models.VI. Corrections*, *Astrophys. J.* **181** (1973) 181;
C.T. Cunningham, R.H. Price and V. Moncrief, *Radiation from collapsing relativistic stars. I — Linearized odd-parity radiation*, *Astrophys. J.* **224** (1978) 643; *Radiation from collapsing relativistic stars. II. Linearized even parity radiation*, *Astrophys. J.* **230** (1979) 870 [SPIRES];
C.T. Cunningham, R.H. Price and V. Moncrief, *Radiation from collapsing relativistic stars. III second order perturbations of collapse with rotation*, *Astrophys. J.* **236** (1980) 674;
J.R. Ipser and R.H. Price, *Nonradial pulsations of stellar models in general relativity*, *Phys. Rev.* **D 43** (1991) 1768.

[7] E. Seidel, *Gravitational radiation from even parity perturbations of stellar collapse: mathematical formalism and numerical methods*, *Phys. Rev.* **D 42** (1990) 1884 [SPIRES].

[8] **C. Gundlach and J.M. Martín-García**, *Gauge-invariant and coordinate-independent perturbations of stellar collapse. I: the interior*, *Phys. Rev* **D 61** (2000) 084024 [gr-qc/9906068] [SPIRES].

[9] T.J. Waters and B.C. Nolan, *Gauge invariant perturbations of self-similar Lemaître-Tolman-Bondi spacetime: even parity modes with $l \geq 2$*, arXiv:0903.3243 [SPIRES];
K. Tomita, *Perturbations in a spherically symmetric inhomogeneous cosmological model with the selfsimilar region*, *Phys. Rev.* **D 56** (1997) 3341 [SPIRES].

[10] J.P. Zibin, *Scalar perturbations on Lemaître-Tolman-Bondi spacetimes*, *Phys. Rev.* **D 78** (2008) 043504 [arXiv:0804.1787] [SPIRES].

[11] U.H. Gerlach and U.K. Sengupta, *Gauge invariant perturbations on most general spherically symmetric space-times*, *Phys. Rev.* **D 19** (1979) 2268 [*Addendum ibid.* **22** (1980) 1300] [SPIRES].

[12] C. Clarkson, *A covariant approach for perturbations of rotationally symmetric spacetimes*, *Phys. Rev.* **D 76** (2007) 104034 [arXiv:0708.1398 [SPIRES];
C. Clarkson and R.K. Barrett, *Covariant perturbations of Schwarzschild black holes*, *Class. Quant. Grav.* **20** (2003) 3855 [gr-qc/0209051] [SPIRES].

[13] G.F.R. Ellis and H. van Elst, *Cosmological models*, *NATO Adv. Study Inst. Ser. C. Math. Phys. Sci.* **541** (1999) 1 [gr-qc/9812046 [SPIRES];
C.G. Tsagas, A. Challinor and R. Maartens, *Relativistic cosmology and large-scale structure*, *Phys. Rept.* **465** (2008) 61 [arXiv:0705.4397 [SPIRES].

[14] J.M. Stewart, *Perturbations of Friedmann-Robertson-Walker cosmological models*, *Class. Quant. Grav.* **7** (1990) 1169 [SPIRES].

[15] T. Regge and J.A. Wheeler, *Stability of a Schwarzschild singularity*, *Phys. Rev.* **108** (1957) 1063 [SPIRES].

[16] V.F. Mukhanov, H.A. Feldman and R.H. Brandenberger, *Theory of cosmological perturbations. Part 1. Classical perturbations. Part 2. Quantum theory of perturbations. Part 3. Extensions*, *Phys. Rept.* **215** (1992) 203 [SPIRES].

[17] K.A. Malik and D. Wands, *Cosmological perturbations*, *Phys. Rept.* **475** (2009) 1 [arXiv:0809.4944] [SPIRES].

Bibliography

[1] H. Bondi, Cosmology, CUP (Cambridge) (1952).

[2] S. Weinberg, Rev. Mod. Phys. **61**, 1 (1989).

[3] N. Straumann, Mod. Phys. Lett. A **21**, 1083 (2006).

[4] J. Frieman, M. S. Turner and D. Huterer, Annu. Rev. Astron. Astrophys. **46**, 385 (2008).

[5] For a review, see E. J. Copeland, M. Sami and S. Tsujikawa, Int. J. Mod. Phys. D **15**, 1753 (2006).

[6] M. Sami, arXiv:hep-th/09010756.

[7] G. Lemaître, Ann. Soc. Sci. Brux. A **53**, 51 (1933).

[8] R. C. Tolman, Proc. Nat. Acad. Sci. **20**, 169 (1934).

[9] H. Bondi, Mon. Not. Roy. Astron. Soc. **107**, 410 (1947).

[10] H. Alnes and M. Amarzguioui, Phys. Rev. D **74**, 103520 (2006).

[11] G. Hinshaw et al., Astrophys. J. Supp. **180**, 225 (2009).

[12] M. R. Nolta et al., Astrophys. J. Supp. **180**, 296 (2009).

[13] H. Shapley, Harvard College Observatory Bulletin **874**, 9 (1930).

[14] J. A. Munoz and A. Loeb, Phys. Mon. Not. Roy. Ast. Soc. **391**, 1341 (2006).

[15] J. R. Gott et al., Astrophys. J. **624**, 463 (2005).

[16] J. P. Zibin, Phys. Rev. D **78**, 043504 (2008).

[17] C. Clarkson, T. Clifton and S. February, J. C. A. P. **6**, 25 (2007).

[18] M. Hicken et al., arXiv:0901.4787.

[19] M. Hicken et al., arXiv:0901.4804.

[20] G. Miknaitis et al., Astrophys. J. **666**, 674 (2007).

[21] P. Astier et al., A&A **447**, 31 (2006).

[22] A. G. Riess et al., Astrophys. J. **659**, 98 (2007).

[23] J. Simon, L. Verde and R. Jimenez, Phys. Rev. D **71**, 123001 (2005).

[24] A. Einstein, Sitzungsber. K. Akad. **6**, 142 (1917).

[25] E. Hubble, Proceedings of the National Academy of Science **15**, 168 (1929).

[26] V. Petrosian, E. Salpeter and P. Szekeres, Astrophys. J. **147**, 1222 (1967).

[27] J. E. Gunn and B. M. Tinsley, Nature **257**, 454 (1975).

[28] A. A. Penzias and R. W. Wilson, Astrophys. J. 124, 419 (1965).

[29] A. R. Liddle and D. H. Lyth, *Cosmological Inflation and Large-Scale Structure*, Cambridge University Press (2000).

[30] A.W. Jones and A.N. Lasenby, Living Rev. Relativity **1**, 11 (1998). [Online Article]: cited on 20 May 2009, http://www.livingreviews.org/Articles/Volume1/1998-11jones/.

[31] J. Ehlers, P. Geren, and R. K. Sachs, J. Math. Phys. **9**, 1344 (1968).

[32] W. R. Stoeger, R. Maartens and G. F. R. Ellis, Astrophys. J. **443**, 1 (1995).

[33] A. H. Guth, Phys. Rev. D **23**, 347 (1981).

[34] F. Zwicky, Helvetica Physica Acta **6**, 110 (1933).

[35] F. Zwicky, Astrophys. J. **86**, 217 (1937).

[36] V. Rubin, Astrophys. J. **238**, 471 (1980).

[37] V. Zacek, arXiv:astro-ph/07070472.

[38] T. J. Sumner, Living Rev. Relativity **5**, 4 (2002). [Online Article]: cited on 17 May 2009, http://www.livingreviews.org/Articles/Volume5/2002-4sumner/.

[39] J. Einasto, arXiv:astro-ph/0901.0632v1.

[40] E. Bertschinger, Annu. Rev. Astron. Astrophys. **36**, 599 (1998).

[41] G. Bélanger, arXiv:astro-ph/0901.0632v1.

[42] S. Perlmutter et al., Astrophys. J. **517**, 565 (1999).

[43] A. G. Riess et al., Astron. J. 116, 1009 (1998), astro-ph/9805201.

[44] T. M. Davis et al., Astrophys. J. **666**, 716 (2007).

[45] M. Kowalski et al., Astrophys. J. **686**, 749 (2008).

[46] R. Durrer and R. Maarteens, Gen Relativ Gravit **40**, 301 (2008).

[47] B. P. Schmidt et al., Astrophys. J. **507**, 46 (1998).

[48] S. Perlmutter et al., Astrophys. J. **483**, 565 (1997).

[49] A. N. Aguirre, Astrophys. J. **512**, L19 (1999).

[50] A. N. Aguirre, Astrophys. J. **525**, 583 (1999).

[51] N. C. Rana, Ap&SS **66**, 173 (1979).

[52] N. C. Rana, Ap&SS **71**, 123 (1980).

[53] P. S. Drell, T. J. Loredo and I. Wasserman, Astrophys. J. **530**, 593 (2000).

[54] R. Jimenez, L. Verde, T. Treu and D. Stern, Astrophys. J. **593**, 622 (2003).

[55] J. Simon, L. Verde and R. Jimenez, Phys. Rev. D **71**, 123001 (2005).

[56] W. L. Freeman et al., Astrophys. J. **553**, 47 (2001).

[57] C. L. Reichardt et al, arXiv:0801.1491.

[58] W. C. Jones et al., Astrophys. J. **647**, 823 (2006).

[59] A. C. S. Readhead et al., Astrophys. J. **609**, 498 (2004).

[60] J. Silk, Astrophys. J. **151**, 459 (1968).

[61] R. A. Sunyaev, and Y. B. Zel'dovich, Ap&SS **7**, 3 (1970).

[62] P. J. E. Peebles and J. T. Yu, Astrophys. J. **162**, 815 (1970).

[63] J. R. Bond and G. Efstathiou, Astrophys. J. **285**, L45 (1984).

[64] J. A. Holtzman, Astrophys. J. **71**, 1 (1989).

[65] D. J. Eisenstein et al., Astrophys. J. **633**, 560 (2005).

[66] C. Alcock and B. Paczynski, Nature, **281**, 358 (1979).

[67] W. J. Percival et al., arXiv:astro-ph/0907.1660.

[68] H. Seo and D. J. Eisenstein, Astrophys. J. **598**, 720 (2003).

[69] C. Blake and K. Glazebrook, Astrophys. J. **594**, 665 (2003).

[70] W. J. Percival et al., Mon. Not. Roy. Ast. Soc. **381**, 1053 (2007).

[71] A. Shafieloo, V. Sahnib and A. A. Starobinsky, arXiv:astro-ph/0903.5141.

[72] M. N. Celerier, arXiv:astro-ph/0609352.

[73] M. N. Celerier, arXiv:astro-ph/0702416.

[74] M. J. Geller and J. P. Huchra, Science **246**, 897 (1989).

[75] G. Efstathiou et al., Mon. Not. Roy. Ast. Soc. **247**, 10 (1990).

[76] W. Saunders et al., Nature **349**, 32 (1991).

[77] T. J. Broadhurst et al., Nature **343**, 726 (1990).

[78] R. Sancisi and T. S. van Albada, Intl. Astron. Union Symp. 117, *Dark Matter in the Universe*, J. Kormendy and G. R. Knapp, editors. Dordrecht, The Netherlands: Reidel, pp. 67 (1987)

[79] S. J. Maddox et al., Mon. Not. Roy. Ast. Soc. **240**, 43 (1990).

[80] J. A. Tyson, Astrophys. J. **96**, 1 (1988).

[81] N. H. Heydon-Dumbleton et al., Mon. Not. Roy. Ast. Soc. **238**, 379 (1989).

[82] J. S. Lilly, Astrophys. J., **411**, 501 (1993).

[83] J. W. Moffat and D. C. Tatarski, arXiv:astro-ph/9404048.

[84] D. Branch, Ann. Rev. Astron. Astrophys. **36**, 17 (1998).

[85] W. L. Freedman, *Critical Dialogues in Cosmology*, Singapore: World Scientific **92** (1997).

[86] A. Sandage and G. A. Tammann, *Critical Dialogues in Cosmology*, Singapore: World Scientific, 130 (1997).

[87] R. D. Blandford and T. Kundic, *The Extragalactic Distance Scale*, London: Cambridge University Press **60** (1997).

[88] I. Zehavi et al., Astrophys. J. **503**, 483 (1998).

[89] B. Paczynski and T. Piran, Astrophys. J. **364**, 341 (1990).

[90] J. W. Moffat and D. C. Tatarski, Phys. Rev. D **45**, 3512 (1992).

[91] K. Tomita, Astrophys. J. **529**, 38 (2000).

[92] K. Tomita, Mon. Not. Roy. Astron. Soc. **326**, 287 (2001).

[93] K. Tomita, Prog. Theor. Phys. **105**, 419 (2001).

[94] K. Tomita, Prog. Theor. Phys. **106**, 929 (2001).

[95] N. Mustapha and C. Hellaby, Gen. Rel. Grav. **33**, 455 (2001).

[96] A. Krasinski and C. Hellaby, Phys. Rev. D **65**, 023501 (2002).

[97] A. Krasinski and C. Hellaby, Phys. Rev. D **69**, 023502 (2004).

[98] A. Krasinski and C. Hellaby, Phys. Rev. D **69**, 043502 (2004).

[99] K. Bolejko, A. Krasinski and C. Hellaby, Mon. Not. Roy. Ast. Soc. **362**, 213 (2005).

[100] C. Hellaby and A. Krasinski, Phys. Rev. D **73**, 023518 (2006).

[101] K. Bolejko and C. Hellaby, Gen. Rel. Grav. **40**, 1771 (2008).

[102] N. Sugiura, K. I. Nakao and T. Harada, Phys. Rev. D **60**, 103508 (1999).

[103] M. N. Celerier, Astron. Astrophys. **353**, 63 (2000).

[104] H. Iguchi, T. Nakamura, and K. Nakao, Prog. of Theo. Phys. **108**, 809 (2002)

[105] Y. Nambu and M. Tanimoto, gr-qc/0507057.

[106] J. W. Moffat, astro-ph/0505326.

[107] R. Mansouri, astro-ph/0512605.

[108] C.-H. Chuang, J.-A. Gu, and W-Y. P. Hwang, astro-ph/0512651.

[109] R. A. Vanderveld, E. E. Flanagan, and I. Wasserman, Phys. Rev. D **74**, 023506 (2006).

[110] A. Krasinski, C. Hellaby, M.N. Celerier and K. Bolejko, arXiv:astro-ph/0903.4070.

[111] R. A. Vanderveld, E. E. Flanagan, and I. Wasserman, arXiv:0904.4319.

[112] D. Garfinkle, arXiv:gr-qc/0605088.

[113] T. Clifton, P. G. Ferreira and K. Land, Phys. Rev. Lett. **101**, 131302 (2008).

[114] J. P. Zibin, A. Moss and D. Scott, arXiv:0809.3761.

[115] C.-M. Yoo, T. Kai and K. Nakao2, arXiv:0807.0932.

[116] N. Mustapha, C. Hellaby and G. F. Ellis, arXiv:gr-qc/9808079.

[117] H. Alnes, M. Amarzguioui and Ø. Grøn, astro-ph/0512006v2 (2006).

[118] S. Alexander et al., arXiv:astro-ph/0712.0370

[119] R. R. Caldwell and A. Stebbins, arXiv:0711.3459.

[120] J. G.-Bellid and Troels Haugbølle, arXiv:0802.1523.

[121] J. G.-Bellido and Troels Haugbølle, arXiv:0807.1326.

[122] K. Bolejko and J. S. B. Wyithe, arXiv:0807.2891.

[123] L. Verde, arXiv:0712.3028.

[124] J. Silk, Astron. Astrophys. **59**, 53 (1977).

[125] D. Stern et al., arXiv:astro-ph/0907.3152.

[126] D. Stern et al., arXiv:astro-ph/0907.3149

[127] M. P. Hobson, G. P. Efstathiou and A. N. Lasenby, *General Relativity: An Introduction for Physicists*, Cambridge University Press, New York (2006).

[128] J. Plebanski and A. Krasinski, *An Introduction to General Relativity and Cosmology*, Cambridge University Press, New York (2006).

[129] A. H. A. Alfedeel and C. Hellaby, arXiv:0906.2343.

[130] C. Clarkson, M. Cortes and B. Bassett, arXiv:astro-ph/0702670.

[131] C. Zunckel and C. Clarkson, arXiv:0807.4304.

[132] C. Clarkson, B. Bassett and T. H.-C. Lu, Phys. Rev. Let. 101, 011301 (2008), arXiv:astro-ph/0712.3457.

[133] R. Hlozek et al., arXiv:0801.3847.

[134] W. L. Freedman, Astrophys. J. **553**, 47 (2001).

[135] H. Akaike, IEEE Transactions on Automatic Control **16**, 716 (1974).

[136] G. Schwarz, Annals of Statistics **6**, 461 (1978).

[137] H. Wei, arxiv:astro-ph/0906.0828.

[138] K. Enqvist and T. Mattsson, arXiv:astro-ph/0609120v4.

[139] K. Enqvist, arXiv:astro-ph/0709.2044v1.